Experimental and Numerical Investigation of the Electromechanical Behavior of High Temperature Superconducting Tapes and Cables Subjected to Various Mechanical Loads

Submitted By

Nathaniel C. Allen
M.S.M.E. – Tufts University (2013)
B.S.M.E. – University of New Hampshire (2011)

In partial fulfillment of the requirements for the degree of

Doctor of Philosophy in Mechanical Engineering

Tufts University
Department of Mechanical Engineering
Medford, Massachusetts 02155

August, 2016

Author ……...
Nathaniel C. Allen
Tufts University
Mechanical Engineering Department

Certified By ……...
Gary Leisk
Senior Lecturer, Tufts University
Mechanical Engineering Department

Certified By ……...
(*Research Advisor)* Luisa Chiesa
Associate Professor, Tufts University
Mechanical Engineering Department

Certified By ……...
Michael Zimmerman
Professor of Practice, Tufts University
Mechanical Engineering Department

Certified By ……...
Makoto Takayasu
Research Scientist, MIT
Plasma Science and Fusion Center

Certified By ……...
Thomas Vandervelde
Associate Professor, Tufts University
Electrical and Computer Engineering

Abstract

Second generation high temperature superconducting (HTS) tapes have great mechanical properties as well as excellent high current and high field capabilities. These characteristics make them a very promising conductor for applications like accelerator and fusion magnets. Several HTS tape cabling methods are under development for these magnet applications. To improve fabrication methods and maximize operational performance of these cables composed of several HTS tapes, it is necessary to characterize both the electromechanical behavior of the full scale cables and of the individual tapes under anticipated thermal, mechanical and electromagnetic loads.

In this work, laboratory experimentation and structural finite element analysis have been used to investigate the electromechanical behavior of single HTS tapes and cables. Experiments were conducted to evaluate critical current performance, the maximum current a superconductor can carry before becoming resistive, under various loads while finite element analysis was used to analyze the strain dependence of that critical current for each load type.

Single tape experiments were conducted on three types of commercially available HTS tapes under pure torsion, axial tension, combined tension-torsion and transverse compression on their wide face and thin edge. The results from the tests indicate single HTS: under pure torsion had no reduction in critical current down to a twist pitch of 120 mm; under axial tension experienced a sharp irreversible critical current degradation at their yield strength; under combined tension-torsion behaved similar to pure tension samples for twist pitch lengths

greater than 150 mm; and under transverse compression were far more sensitive to loads applied on their thin edge compared to their wide face.

The single HTS tapes were also analyzed under the same loading conditions using structural finite element analysis. A novel technique was developed for modeling the layered composite structure of the HTS tapes using structural solid-shell elements. The numerical model was able to closely replicate the experimental stress-strain curves and torque behavior of each type of tape. The simulations also produced detailed axial strain results which were successfully paired with an analytical model to predict the critical current performance of the tapes. The numerically predicted critical current was found to have close agreement with the experimental results for each load type.

In addition to the single tape work, electromechanical experiments on two HTS cabling methods, designed for high field magnet applications, were conducted. The HTS cable-in-conduit conductor (CICC) was tested under bending down to a diameter of 0.25 m and revealed that the minimum safe bending diameter to avoid critical current degradation was 0.5 m. The twisted stacked-tape cable (TSTC) was tested under mechanical transverse compression and overall performed better than expected based on real electromagnetic load degradations seen during high field tests.

Both HTS cabling methods were also analyzed using finite element analysis. A methodology for modeling full scale three-dimensional HTS cables was developed incorporating contact pair relationships for modeling the relative motion between tapes. The full scale cables were simulated under bending and

electromagnetic transverse compression. Their numerical strain results were validated against analytical models and were used to predict the critical current performance of the cable as done for single tape. The HTS CICC model under bending agreed well with the experimental critical current results for a nearly frictionless case having a coefficient of only 0.02, indicating the tapes can slide freely during bending. The TSTC model under transverse compression found that a solid cylindrical copper core provides the best support for the tapes under electromagnetic loads.

The overall agreement seen between the experimental measurements and the finite element analysis validates the electromechanical characteristics of the tapes and cables presented in this work. Together the numerical and experimental results provided new details about the strain dependence of the critical current for each load type.

Acknowledgements

I would like to deeply thank everyone who contributed to the completion of my research. Most importantly I want to thank my research advisor Luisa Chiesa for all of her support along this journey. Luisa has not just been an advisor to me but has also been a mentor and most importantly a friend. She is one of the kindest and most generous people I know. She first introduced me to the field of superconductivity, taught me all of my experimental skills and helped me develop my expertise with finite element modeling and for this I am extremely appreciative. I could not have asked for a better "boss" and will greatly miss my time in the Superconductivity Lab. Luisa, I am profoundly grateful for everything you have done for me and my family.

I would also like to thank the "master" Makoto Takayasu who has been an integral part of all of my research. Makoto is one of the most intelligent scientists I have ever met and I have learned countless things form his advice, wisdom and technical expertise. I can only hope that I picked up some of his patience and dedication.

I would also like to thank Gary Leisk who has been a helpful mentor and teacher to me during my graduate studies and has provided valuable insight into this work. I would also like to thank the other members of my committee, Mike Zimmerman and Tom Vandervelde, for all of their contributions.

A special thanks goes out to all of my fellow graduate students who have helped me complete this work, particularly Federica and Zijia. Fede, I will miss working with you in lab and listening to all of your stories. I would also like to

acknowledge the undergraduates students who also had a hand in this research: Amel, Andrew, Madeline and Oliver.

Last but certainly not least, I would like to thank my family for all of their support and especially my loving wife Maren for her extreme patience during my graduate studies. Maren is the most amazing woman I have ever met. She has always been there for me and has blessed me with our beautiful daughter Finley. Maren, I love you so much and would not be where I am today without you.

Table of Contents

Abstract ..... **ii**
Acknowledgements ..... **v**
Table of Contents ..... **vii**
List of Figures ..... **ix**
List of Tables ..... **xiii**
Nomenclature ..... **xiv**

1.0 Introduction **1**
1.1 Background of Superconductivity 1
1.2 Types of Superconductors 2
1.3 LTS versus HTS 4
1.4 Applications of Superconductivity 6
1.5 Why HTS 8

2.0 High Temperature Superconductors **11**
2.1 Second Generation HTS Tapes 11
2.2 Cabling Techniques 14
2.2.1 Twisted Stacked-Tape Cables 15
2.2.2 HTS Cable-in-Conduit Conductor 16
2.3 Electromechanical Characteristics 17
2.3.1 Prior Research 18
2.4 Scope of Work 19

3.0 Single Tape Experiments **21**
3.1 Pure Torsion 21
3.1.1 Experimental Setup 22
3.1.2 Results 23
3.2 Axial Tension 27
3.2.1 Experimental Setup 27
3.2.2 Results 29
3.3 Combined Tension-Torsion 33
3.3.1 Experimental Setup 34
3.3.2 Results 36
3.4 Transverse Compression 39
3.4.1 Experimental Setup 39
3.4.2 Results 42
3.5 Summary and Future Work 45

4.0 Single Tape Modeling **47**
4.1 Finite Element Analysis 47
4.1.1 Solid-shell elements 48
4.1.2 Mesh density 50
4.1.3 Material Properties 52
4.1.4 Boundary Conditions 54

4.1.5 Critical Current Estimation 55
4.2 Pure Torsion 57
4.2.1 Model Details 58
4.2.2 Results 59
4.3 Axial Tension 63
4.3.1 Model Details 64
4.3.2 Results 65
4.4 Combined Torsion-Tension 69
4.4.1 Model Details 70
4.4.2 Results 71
4.5 Summary and Future Work 76

5.0 HTS Cable Experiments 78
5.1 Bending 78
5.1.1 Experimental Setup 79
5.1.2 Results 80
5.2 Transverse Compression 83
5.2.1 Experimental Setup 84
5.2.2 Results 85
5.3 Summary and Future Work 89

6.0 HTS Cable Modeling 91
6.1 Finite Element Analysis 91
6.1.1 Element Types 93
6.1.2 Finite element mesh 94
6.1.3 Material Properties 96
6.1.4 Contact Relationships 97
6.1.5 Boundary Conditions and Loads 98
6.1.6 Critical Current Estimation 100
6.2 Bending 102
6.2.1 Model Details 103
6.2.2 Results 106
6.3 Electromagnetic Transverse Compression 112
6.3.1 Model Details 113
6.3.2 Results 115
6.4 Summary and Future Work 121

7.0 Conclusion 124
8.0 References 129

List of Figures

1.0 Introduction

Figure 1.1 – Schematic of a critical surface of a superconductor which is defined by three critical parameters: temperature, current density and magnetic field. 2

Figure 1.2 – Plot of the upper critical magnetic field as a function of critical temperature for five common Type II superconducting materials.... 4

Figure 1.3 – Schematic showing three superconducting magnet applications: fusion energy, high energy physics and magnetic resonance imaging. 7

Figure 1.4 – Plot of engineering critical current density as a function of applied magnetic field for common LTS and HTS materials. 9

2.0 High Temperature Superconductors

Figure 2.1 – Schematic of the multilayered composite architecture of a HTS tape. Note: layers are not to scale. 12

Figure 2.2 – Images of the five main HTS cabling methods suitable for high field magnets: (a) Twisted Stacked-Tape Cable (TSTC); (b) Roebel assembled coated conductor (RACC); (c) conductor on round core (CORC) cables; (d) HTS slotted-core CICC; and (e) round strands made by twisted stacks. 15

Figure 2.3 – Images of different twisted stacked-tape cable variations. The twisted tape stack can be place in a solid copper core (a), a solder filled copper tube (b) or a completely soldered braided copper sleeve (c). 16

Figure 2.4 – Images of the HTS slotted-core CICC [20]. (a) Cross section of real manufactured cable and (b) schematic of one slot with a stack of nineteen tapes. 17

3.0 Single Tape Experiments

Figure 3.1 – Schematic of the pure torsion experimental device highlighting twisted HTS sample, flexible negative current lead, input rotation shaft and torque meter. 22

Figure 3.2 – Plot of torque magnitude as a function of the twist pitch for SuperPower (a), SuNAM (b) and AMSC (c) tapes. Measurements taken at 77 K for three load cycles. 25

Figure 3.3 – Plot of critical current as a function of the twist pitch length for SuperPower (a), SuNAM (b) and AMSC (c) tapes under pure torsion. 26

Figure 3.4 – Images of the experimental tensile test probe. (a) Schematic of entire probe, (b) close-up of tensile sample with flexible current leads and (c) double extensometers mounted on sample. 28

Figure 3.5 – Plots of stress-strain curves for SuperPower (a), SuNAM (b) and AMSC (c) tapes at 77 K and room temperature (RT). 30

Figure 3.6 – Plots of critical current as a function of axial tensile stress for SuperPower (a) and SuNAM (b) tapes. Measurements were taken at 77 K and in self-field. 32
Figure 3.7 – Images of the combined tension-torsion test probe. (a) Schematic of entire probe and (b) close-up showing twisted sample and torque meter. 35
Figure 3.8 – Plot of critical current as a function of applied tensile stress for twisted SuperPower (a) and SuNAM (b) tapes. Sample twist pitch indicated in parenthesis. 37
Figure 3.9 – Plot of change in torque as a function of applied tensile stress for twisted SuperPower (a) and SuNAM (b) tapes. Sample twist pitch indicated in parenthesis. 38
Figure 3.10 – Image of the experimental transverse compression device. The load is applied through a central forcing screw. 40
Figure 3.11 – Schematic of transverse compression pressing fixtures. (a) Side view of wide face compression and (b) end view of thin edge compression. 41
Figure 3.12 – Plot of critical current as a function of transverse compressive stress on the wide face of single HTS tapes. 43
Figure 3.13 – Plot of critical current as a function of transverse compressive stress on the thin edge of (a) AMSC and (b) SuperPower tapes. ... 44

4.0 Single Tape Modeling

Figure 4.1 – Schematic illustration of the SOLSH190 solid-shell finite element. The colors indicate different layers defined within the element. 49
Figure 4.2 – Schematic depiction of how a composite HTS tape is modeled using solid-shell elements. The internal structure depicted by dashed lines. 50
Figure 4.3 – Image of a typical finite element mesh having 20 elements through the width, a length-to-width ratio of 2 and one element through the thickness. 51
Figure 4.4 – Schematic of an isotropic bilinear stress-strain curve used to define nonlinear elastoplastic material properties in the structural finite element models. 53
Figure 4.5 – Image of a pilot node multipoint coupling constraint applied on the end of an HTS tape. 55
Figure 4.6 – Plot of torque as a function of twist pitch for SuperPower (a) SuNAM (b) and AMSC (c) tapes. Experimental data plotted alongside finite element results. 60
Figure 4.7 – Color contour plot of the axial strain profile in a twisted HTS tape determined from finite element analysis. 61
Figure 4.8 – Plot of normalized critical current as a function of twist pitch for SuperPower (a), SuNAM (b) and AMSC (c) tapes. Experimental data plotted alongside the estimated critical current calculated from the numerical strain data. 62

Figure 4.9 – Plot of stress-strain curves for SuperPower, SuNAM and AMSC tapes at 77 K. Finite element analysis results (open symbols) plotted alongside averaged experimental data (solid curves). 66
Figure 4.10 – Plots of normalized critical current as a function of applied tensile stress for SuperPower (a) and SuNAM (b) tapes [44]. Averaged experimental data plotted alongside the estimated critical current calculated from the numerical strain data. 68
Figure 4.11 – Plots of the change in torque as a function of applied tensile stress on twisted samples from SuperPower (a), SuNAM (b) and AMSC (c) tapes. 72
Figure 4.12 – Plots of normalized critical current (I_c) as a function of applied tensile stress on twisted samples from SuperPower (a), SuNAM (b) and AMSC (c) tapes..... 75

5.0 HTS Cable Experiments

Figure 5.1 – Image of the HTS slotted-core CICC bent on 0.4 m diameter wooden fixture showing individual current leads for each active tape. 80
Figure 5.2 – Plots of critical current as a function of bending diameter for two HTS CICC cables. (a) Short twist pitch and (b) long twist pitch. Legend: Slot # - Tape #..... 81
Figure 5.3 – Schematic of transverse compression load fixtures for TSTC conductors. (a) Uniform distributed pressing plate and (b) concentrated two-point pressing fixture..... 84
Figure 5.4 – Plot of critical current as a function of average transverse compressive stress for a 24-tape soldered TSTC conductor. 86
Figure 5.5 – Plot of critical current as a function of average transverse compressive stress for a 40-tape TSTC conductor soldered inside a copper tube. 88

6.0 HTS Cable Modeling

Figure 6.1 – Images of the discretized cable geometries of the (a) HTS slotted-core CICC and (b) the TSTC soldered inside a copper tube..... 95
Figure 6.2 – (a) Schematic depiction of a coupled displacement and rotation load used to apply pure bending to HTS cables and (b) internal distributed electromagnetic transverse load applied to a TSTC inside a solder filled tube. 100
Figure 6.3 – Images the generic TSTC models analyzed under bending. (a) A centrally located tape stack and (b) a tape stack offset a radial distance of (*h*). 104
Figure 6.4 – Plots of numerical bending strain as a function of the twist angle for four HTS tapes in a TSTC under a 300 mm bending diameter. (a) Bonded model and (b) frictionless model. 107
Figure 6.5 – Plot of the analytical and numerical bending strain as a function of the twist angle of the TSTC under a bending diameter of 0.3 m. 108

Figure 6.6 – Plot of the numerical bending strain as a function of the twist angle in the HTS slotted-core CICC under a 0.5 m bending diameter..... 110
Figure 6.7 – Plot of the normalized critical current as a function of bending diameter for the HTS CICC as predicted from the finite element strain results with various friction coefficients..... 111
Figure 6.8 – Images of a typical 40-tape TSTC having a stack rotation of 45° with two different support methods; (a) a solid copper core and (b) a solder filled copper tube..... 114
Figure 6.9 – Stress contours in a solid copper core TSTC with a 45° stack rotation angle and a 300 kN/m load. (a) Stress in the thickness direction and (b) stress in the width..... 116
Figure 6.10 – Plots of maximum compressive stress in the TSTC as a function of applied transverse load for three different stack orientation angles (Ac). (a) Plot of stress through the thickness and (b) plot of stress through the width for both a solid copper core support and a solder filled copper tube support. 118

List of Tables

1.0 Introduction
Table 1 – Superconducting materials and their critical parameters 3

2.0 High Temperature Superconductors
Table 2 – Dimensions and specifications of tested HTS tapes 13

3.0 Single Tape Experiments
Table 3 – Mechanical properties of tested HTS tapes 31

4.0 Single Tape Modeling
Table 4 – Material properties for HTS tapes used in the numerical models..... 53

5.0 HTS Cable Modeling
Table 5 – Bilinear material properties of HTS cable support materials 97
Table 6 – Influence of friction on transverse compression..... 120

Nomenclature

A –	ampere
B –	magnetic flux density
CICC –	Cable-in-Conduit Conductor
E –	electric field
ENEA –	research laboratory Frascati, Italy
FEA –	finite element analysis
GPa –	Gigapascal
H_c –	critical magnetic field
HTS –	high temperature superconductor
I –	current
I_c –	critical current
I_{c0} –	baseline critical current
J_c –	critical current density
K –	kelvins
kg –	kilogram
LTS –	low temperature superconductor
m –	meter
MIT –	Massachusetts Institute of Technology
mm –	millimeter
MPa –	Megapascal
N –	Newton
T –	tesla
T_c –	critical temperature
V –	volt
µV –	microvolt

1.0 Introduction

1.1 Background of Superconductivity

Superconductivity is defined as the ability to conduct electrical current without resistance. This phenomenon was discovered by Dutch physicist Kamerlingh Onnes in 1911, three short years after he successfully liquefied helium. While investigating the electrical resistance of metals at low temperatures, Onnes noticed the resistance of mercury suddenly dropped to zero below 4 K [1]. Since its discovery, a large number of pure metals and alloys have been found to be superconductive at low temperatures.

Superconductors refer to a class of compounds that exhibit this zero resistance to electrical current behavior. When these superconductors completely enter a superconducting state they are capable of transporting large amounts of current through small spaces with no heat generation. This high current density no energy loss characteristic of superconductors has made them an essential technological material for the development of high field magnets.

The superconductive state of a material was later found to be governed not only by its temperature but also by its magnetic field and current density. The transition between the superconductive state and normal resistive state of a superconductor is defined by three parameters: critical temperature (T_c), critical magnetic field (H_c), and critical current density (J_c). These parameters together create what is called a critical surface, as shown in Figure 1.1. The critical surface defines the domain of superconductivity for a material. If a material is on or beneath this critical surface it will be in a superconductive state.

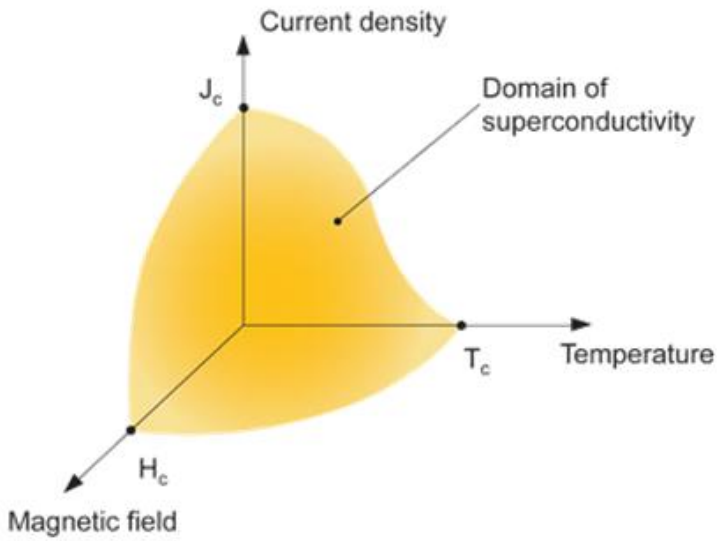

Figure 1.1 – Schematic of a critical surface of a superconductor which is defined by three critical parameters: temperature, current density and magnetic field.

The electrical performance of a superconductor is generally evaluated using its critical current density or simply its critical current (I_c). The critical current refers to the maximum current a superconductor can carry before becoming resistive under a fixed operating temperature and magnetic field, as depicted in Figure 1.1. The critical current of a superconductor is also known to be a function of applied external load and is the focus of this research.

1.2 Types of Superconductors

Type I superconductors are mostly pure metals and are classified by having only one critical magnetic field at which point the material becomes resistive. A few common Type I superconductors are listed in Table 1 along with their critical magnetic field and temperature. As seen in the table these pure elemental superconductors are characterized by low critical temperatures and more importantly by very low critical magnetic fields ($\mu_0 H_{c0}$). Because of this low critical field, these Type I superconductors are unable to carry any appreciable

current in the presences of magnetic fields, making them technologically inadequate for many practical applications.

The applicability of superconductors particularly for high field magnet applications came with the development of Type II superconductors which are typically metal alloys. The five most common Type II superconductors are listed in Table 1 along with their critical parameters. These superconductors are currently being used in or are being researched for high field magnet applications.

Table 1 – Common superconducting materials and their critical parameters [2].

		Material	**T_c (K)**	**$\mu_0 H_{c0}$ (T)**
Type I	***LTS***	Ti	0.40	0.0056
		Al	1.18	0.0105
		Sn	3.72	0.0305
		Hg	4.15	0.0411
		Pb	7.19	0.0803
Type II	***LTS***	NbTi	9.8	10.5
		Nb_3Sn	18.3	24.5
		MgB_2	39	15
	HTS	$YBa_2Cu_3O_7$ (*YBCO*)	93	150
		$Bi_2Sr_2CaCu_2O_8$ (*BSCCO*)	110	110

These Type II superconductors are classified as having two critical field values (lower and upper). Below the lower critical field (H_{c1}) the superconducting material behaves similar to a Type I superconductor and exhibits perfect diamagnetism as described by the Meissner effect [3]. Above the upper critical field (H_{c2}) magnetic flux fully penetrates the superconducting material returning it to the normal resistive state. In between the two critical fields, magnetic flux lines locally penetrate the material without destroying its overall superconductive state.

This partial flux penetration in Type II superconductors allows them to remain

superconductive under higher magnetic fields while carrying substantial amounts of current [4]. This high current, high field characteristic makes Type II superconductors especially well-suited for high field magnets.

1.3 LTS versus HTS

Superconductors are often grouped into two categories based on their critical temperature which is an intrinsic property of the material. High temperature superconductors (HTS) have critical temperatures above 77 K, while low temperature superconductors (LTS) have critical temperatures below 77 K [1]. This transition temperature signifies the boiling point of liquid nitrogen at atmospheric pressure.

The critical temperature and field of five common Type II superconductors are listed in Table 1. Three of these materials are LTS (NbTi, Nb_3Sn and MgB_2) and two are classified as HTS (YBCO and BSCCO) based on their critical temperatures as mentioned above. The critical magnetic field as a function of critical temperature for these five superconductors is plotted in Figure 1.2 and clearly highlights the larger superconducting domain of HTS materials.

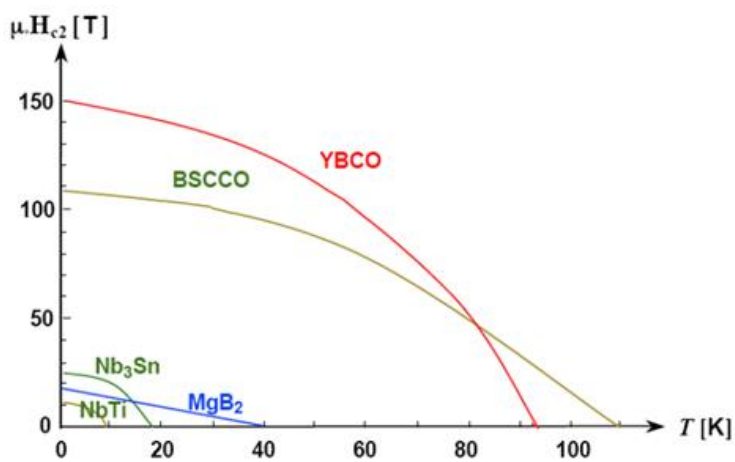

Figure 1.2 – Plot of the upper critical magnetic field as a function of critical temperature for five common Type II superconducting materials.

Niobium titanium (NbTi), niobium tin (Nb_3Sn) and magnesium diboride (MgB_2) are the three main Type II LTS materials. Of these materials, NbTi and Nb_3Sn are the most technologically mature and are the superconductors currently being employed in the high field magnet applications discussed in Section 1.4. Because of their critical temperatures, 9.8 K and 18.3 K respectively for NbTi and Nb_3Sn, they are both commonly operated in 4.2 K environments using liquid helium or super-cooled helium gas. The critical magnetic field of NbTi is 10.5 T and of Nb_3Sn is 24.5 T, as listed in Table 1.

MgB_2 is a relatively new LTS material and has a critical magnetic field of 15 T which is in between that of NbTi and Nb_3Sn. The main characteristic that makes MgB_2 an attractive superconductor for future applications is its higher critical temperature of 39 K. This allows it to be operated under a slightly wider range of temperatures including a 20 K liquid hydrogen environment.

The two most technologically advantageous HTS materials are yttrium-barium-copper-oxide (YBCO) and bismuth-strontium-calcium-copper-oxide (BSCCO). The high critical temperatures of YBCO (93 K) and BSCCO (110 K) materials lend themselves to operating at 77 K in liquid nitrogen environment. Operating at higher temperatures, particularly liquid nitrogen which is cheaper and safer than liquid helium, is one of the main advantages of HTS. The performance of HTS materials is also greatly improved by operating at lower temperatures like 4.2 K which is another advantage for high field magnet applications.

In addition to their higher critical temperatures, the other main characteristics

which set HTS materials apart from LTS materials are their significantly higher critical magnetic fields. As seen in Table 1, YBCO and BSCCO have critical fields of 150 T and 110 T which are almost an order of magnitude larger than the critical fields of the three LTS materials shown. This higher critical value means that HTS conductors can be operated under a much wider range of magnetic fields making them particularly well suited for high field magnet applications.

1.4 Applications of Superconductivity

Since its discovery the unique zero resistance behavior of superconductors has sparked interest into their future applications. After the development of Type II superconductors, superconductivity has been used in many different applications ranging from: small electronics and sensors; to power transmission lines and transformers; to electric motors and generators [6].

Currently the primary industrial use for superconductors is in magnet technology and in particular high field magnets. This is due to the fact that superconductors have high current density and no energy dissipation allowing for the development of compact, high field magnets with low power requirements. The three largest applications of superconducting magnets are fusion energy, high energy physics and medical imaging. Examples of these three applications are shown in Figure 1.3.

High field magnet applications such as accelerator and fusion magnets are one of the largest applications for superconductors. Particle accelerators used in high-energy physics research, like the Large Hadron Collider (LHC) study the collision of particles. The LHC contains over fifteen hundred high field fully

superconducting dipole and quadrupole magnets to bend and confine the particle beams [7]. The size, economics and feasibility of the LHC would not be possible without superconducting magnets.

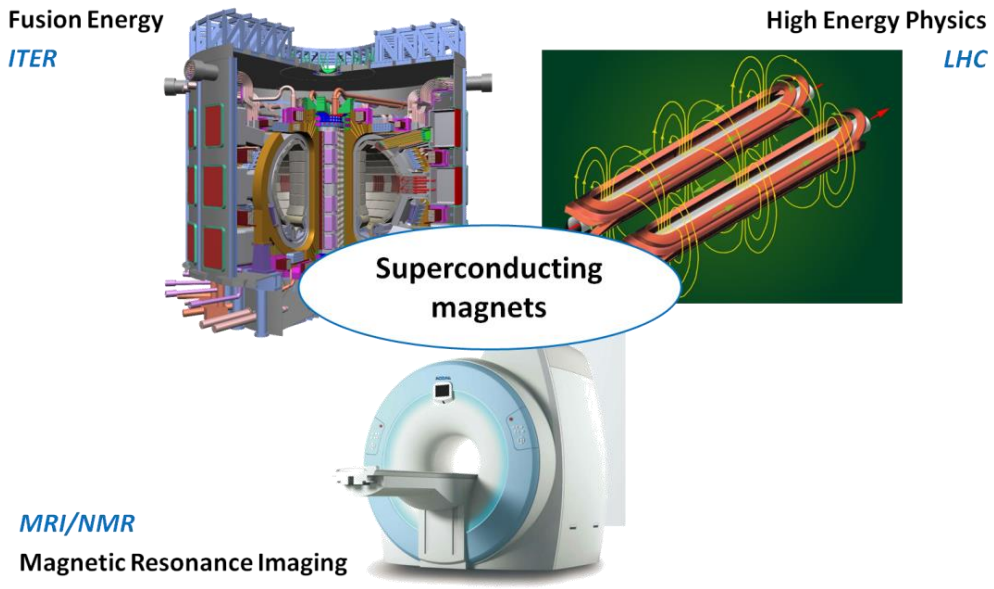

Figure 1.3 – Schematic showing three superconducting magnet applications: fusion energy, high energy physics and magnetic resonance imaging [6]-[9].

Another major high field application of superconductors is fusion energy. ITER is an international project aimed at demonstrating the feasibility of fusion energy for power generation and has been one of the biggest drivers for superconductivity research over the past few decades. In ITER the high temperature plasma in the reactor is confined, shaped and charged using three main superconducting magnet systems: central solenoid, poloidal field coils and toroidal field coils [8].

The one truly commercial application of superconductors is magnetic resonance imaging (MRI) systems and nuclear magnetic resonance (NMR) devices. Superconducting magnets are specifically well suited for MRI/NMR systems because they provide very stable high magnetic fields over a large

volume needed for whole body scanning. Most mass produced MRI systems on the market today use superconducting magnets [9].

1.5 Why HTS

The three high field superconducting magnet applications discussed in Section 1.4 exclusively use Nb_3Sn and NbTi materials. The reason for this is that these two LTS materials are more technologically mature, cheaper and are fully capable of meeting the current field requirements of the applications. That said the future of all three of these applications, particularly fusion and high energy physics, are aimed at achieving higher magnetic fields.

The current state of LTS high field superconducting magnets has a maximum field of around 16 T and 18 T assuming an operating current density of between 500 and 800 A/mm^2 and a temperature of 4.2 K. This magnetic field limitation of LTS materials (NbTi, Nb_3Sn and MgB_2) is depicted in Figure 1.4 which plots the critical current density as a function of magnetic field. The above mentioned range of current and field are shown by the shaded regions. The critical current density is the current divided by the cross sectional area of the entire wire/tape.

The critical current behaviors of HTS materials as a function of magnetic field are also displayed in Figure 1.4. Both HTS materials, BSCCO and YBCO, indicate a gradual decrease in critical current under increasing loads in comparison to the sharp drop in critical current density of the LTS materials due to their much lower critical magnetic fields. From the figure it can be concluded that the only superconducting materials technically feasible to achieve higher magnetic fields above 20 T are HTS.

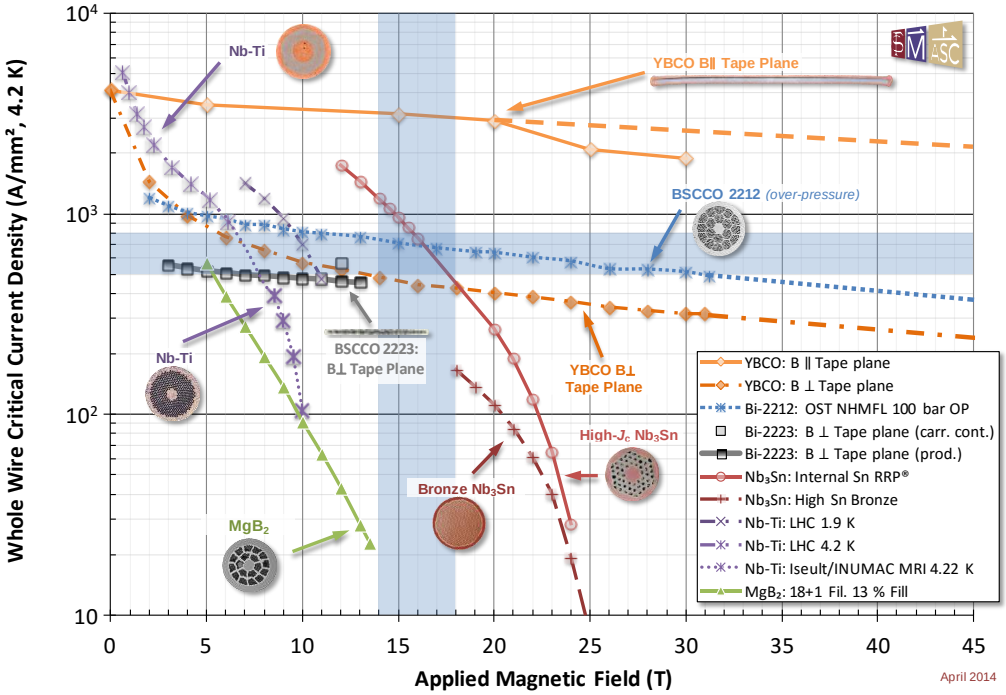

Figure 1.4 – Plot of engineering critical current density as a function of applied magnetic field for common LTS and HTS materials [5].

BSCCO and YBCO are the two primary HTS materials currently being researched for high field magnet applications. One advantage of BSCCO is that it can be made into a round wire form while YBCO can only be produced as thin tapes due to its crystalline structure. The wire geometry gives BSCCO isotropic properties and allows for easier cabling and magnet coil winding.

The BSCCO material however is brittle and has to be reinforced with silver or silver magnesium which makes the conductor expensive. The electrical performance of BSCCO is also very dependent on the heat treatment process and typically requires a high overpressure to obtain the uniformity and high critical current densities desired. Also, BSCCO has poor critical current density at elevated temperatures in the presence of magnetic fields making it only applicable for 4.2 K magnet applications.

YBCO tapes on the other hand, maintain high critical current densities in the presence of both high magnetic field and high temperatures. They do not require a heat treatment and have strong mechanical properties allowing them to be easily handled during cable fabrication and magnet winding. Recent advancements in tape processing have lowered costs and greatly improved the anisotropic performance of the tapes. Other “rare earth” cuprate superconducting tapes besides YBCO are also available with similar characteristics and are referred to as simply REBCO (rare-earth-barium–copper–oxide) tapes.

For these reasons, REBCO tapes (including YBCO) have become the primary focus of fusion and high energy physics research aimed at achieving higher magnetic fields and higher operating temperatures. This work has focused on characterizing the electromechanical behavior of these REBO HTS tapes and cables to help advance their implementation into high field magnet applications.

2.0 High Temperature Superconductors

High temperature superconductors, particularly second generation REBCO (rare-earth-barium–copper–oxide) tapes, have excellent high current capabilities at high magnetic fields and strong mechanical properties. These characteristics make them a very promising conductor for high field magnet applications, such as accelerator and fusion magnets. The main challenge of HTS tapes is their flat layered structure which creates mechanical and field-orientation anisotropy and causes difficulty creating suitable multi-tape high current density cables.

2.1 Second Generation HTS Tapes

Second generation HTS tapes have a thin rectangular geometry and a multilayered composite architecture as illustrated in Figure 2.1. These tapes have a strong structural material (typically Hastelloy®, stainless steel or nickel-tungsten alloys) for a substrate. Thin ceramic oxides (buffer layers), a superconducting REBCO film (generally YBCO, GdBCO or SmBCO) and a silver cap are deposited on the substrate by chemical or physical means. The layered conductor is then coated with a stabilizing layer(s) (usually pure copper, copper alloy or stainless steel) by different techniques including electroplating and lamination.

The tape fabrication process is unique for each manufacturer but in general consists of sequential reel-to-reel deposition steps taking place at elevated temperatures. Some of the different deposition techniques being used for the buffer, REBCO and silver films are: ion-beam-assisted deposition (IBAD), metal organic chemical vapor deposition (MOCVD), reactive co-evaporation by

deposition and reaction (RCE-DR), rolling-assisted biaxially-textured substrates (RABiTS) and magnetron sputtering. The addition of the stabilizing layer/coating is the final step in the process and is typically applied by electroplating or in a few cases by a soldered lamination.

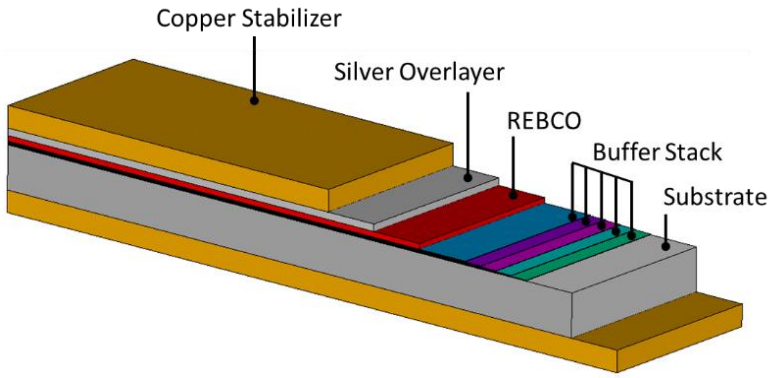

Figure 2.1 – Schematic of the multilayered composite architecture of a HTS tape. Note: layers are not to scale.

Commercial HTS tapes are now available from several industrial manufacturers including: American Superconductor, Bruker HTS, Fujikura, SuNAM, SuperOx and SuperPower [10]-[15]. The tapes from each manufacturer have their own unique composite structure (materials, layers, thicknesses, etc.) and deposition processes which give every type of tape unique mechanical and electromechanical characteristics.

This research focused on HTS tapes from three manufacturers: SuperPower, SuNAM and American Superconductor (AMSC). The dimensions, specifications and characteristics of the three analyzed tapes are presented in Table 2. The width and thickness dimensions listed in the table are mean values from fifty measurements taken on each tape. Similarly, the reported critical currents were the mean values from several critical current measurements conducted in this work. The critical current values were taken at 77 K, in self-field conditions with

no applied load and were evaluated at an electric field criterion of 100 μV/m. The calculated average values presented in the table all fall within the range provided from the manufacturers.

Table 2 – Dimensions and specifications of tested HTS tapes [10]-[12].

	SuperPower	**SuNAM**	**AMSC**
Type	SCS4050-AP	SCN04150	344C
Processing	IBAD-MOCVD	RCE-DR	RABiTS-MOD
Width (mm)	4.027 ± 0.057	4.062 ± 0.008	4.361 ± 0.013
Superconductor	GdBCO/YBCO	GdBCO	YBCO
Thickness (mm)	0.092 ± 0.001	0.144 ± 0.001	0.205 ± 0.005
Substrate *(thickness)*	Hastelloy® C-276 *(50 μm)*	Stainless Steel *(100 μm)*	Ni-5at%W *(75 μm)*
Cu Stabilizer *(total thickness)*	Electroplated *(40 μm)*	Electroplated *(40 μm)*	Laminated *(100 μm)*
Critical Current *77 K, self-field*	112 ± 3 A	229 ± 6 A	111 ± 1 A

As seen from Table 2, all three tapes investigated in this work have rather different layered compositions, overall thickness and deposition techniques. These differences give all three tapes unique mechanical and electrical characteristics as presented in this work. The electrical characteristics and maximum critical current of the three tapes was dependent on the choice of deposition technique and the type of "rare-earth" barium-copper-oxide material being used.

The overall thickness of the tapes is a result of their layered composition particularly their substrate and type of copper stabilization being used. The choice of substrate materials and resulting substrate thickness was one of the biggest differences between the three tapes being investigated. The thickness and method of copper stabilization, electroplated or laminated, was another big area of

difference between the tapes. The substrate and copper stabilizing layers are the two thickest functional layers of the tape and as a result govern the overall mechanical characteristics of the tape.

2.2 Cabling Techniques

High field magnet applications require low ac loss high current density cables composed of several HTS tapes. The major challenge of creating these cables is the flat thin architecture of the HTS tapes which inhibits the use of conventional cabling techniques for round wires.

Several novel methods for cabling multiple HTS tapes together are under development [16]-[20]. Each cabling method has differences in assembly, tape utilization, transposition and mechanical properties among other things. Examples of the five main cabling techniques are presented in Figure 2.2.

The Roebel assembled coated conductor (RACC) [16] punches HTS tapes with a zigzag pattern and then assembles them into the Roebel bar configuration displayed in Figure 2.2(b). The conductor on round core (CORC) cable [17] tightly winds multiple coated conductors in a helical fashion on a small round former, Figure 2.2(c). Twisted stacked-tape cable (TSTC) [18] stacks multiple tapes into a rectangular configuration and then twists them along their axis as shown in Figure 2.2(a). A variation of the stacked-tape cable is round strands made by twisted stacks, Figure 2.2(e), in which the stack of coated conductors is placed between two half-round copper profiles which are twisted [19]. These concepts can also be used in larger multistage Rutherford and cable-in-conduit conductors (CICC) made with multiple of these individual cables. The last major

cabling technique is the HTS slotted-core CICC [20] where stacks of tapes are placed in five helical slots of an aluminum core with a central cooling channel as shown in Figure 2.2(d).

Every HTS cabling method is unique and as a result will have very different electromechanical characteristics. The experimental and numerical investigations presented in this work are focused on the TSTC and the HTS CICC. These cables are currently being made with SuperPower, SuNAM and AMSC tapes. The specifications of these three tapes are provided in Table 2 of Section 2.1.

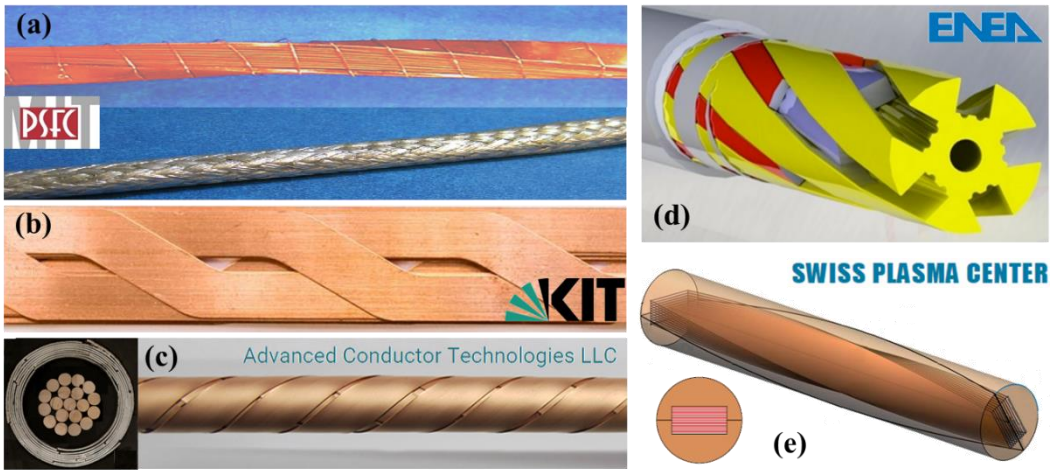

Figure 2.2 – Images of the five main HTS cabling methods suitable for high field magnets [16]-[20]: (a) Twisted Stacked-Tape Cable (TSTC); (b) Roebel assembled coated conductor (RACC); (c) conductor on round core (CORC) cables; (d) HTS slotted-core CICC; and (e) round strands made by twisted stacks.

2.2.1 Twisted Stacked-Tape Cables

Twisted stacked-tape cables in general refer to any cable consisting of a stack of HTS tapes twisted about its axis or helically wrapped around a former. The basic TSTC is a simple, compact and flexible cable with high current density and high tape utilization. SuperPower tapes and to a lesser extent AMSC tapes are being used for TSTC conductors. Variations of the TSTC are being developed to provide additional structural support and electrical stability. One variation is to

place the stack of twisted tapes inside a helically machined groove in a solid cylindrical copper core shown in Figure 2.3(a). Another method is to place the twisted stack inside a solder filled copper tube depicted in Figure 2.3(b). A similar variation is to place the twisted tape stack inside a soldered filled braided copper sleeve illustrated by Figure 2.3(c).

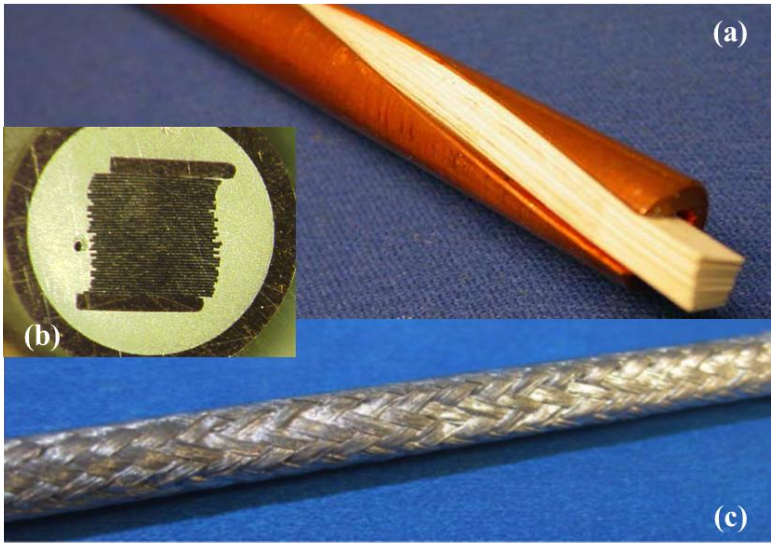

Figure 2.3 – Images of different twisted stacked-tape cable variations [18]. TSTC in a solid copper core (a), a solder filled copper tube (b) and a braided copper sleeve (c).

2.2.2 HTS Cable-in-Conduit Conductor

The HTS CICC is designed particularly for fusion applications and is comprised of a twisted aluminum core with five helical slots around its perimeter. These five slots are designed to accommodate stacks of twenty or more HTS tapes, depending on the type. The aluminum core also has one main central cooling channel for liquid cryogen as well as secondary grooves and space around the tape stack for additional coolant flow. The assembled cable is equipped with a structural aluminum jacket for mechanical stabilization. The entire cable was designed to be industrially feasible using current cabling infrastructure. Further details can be found in [20].

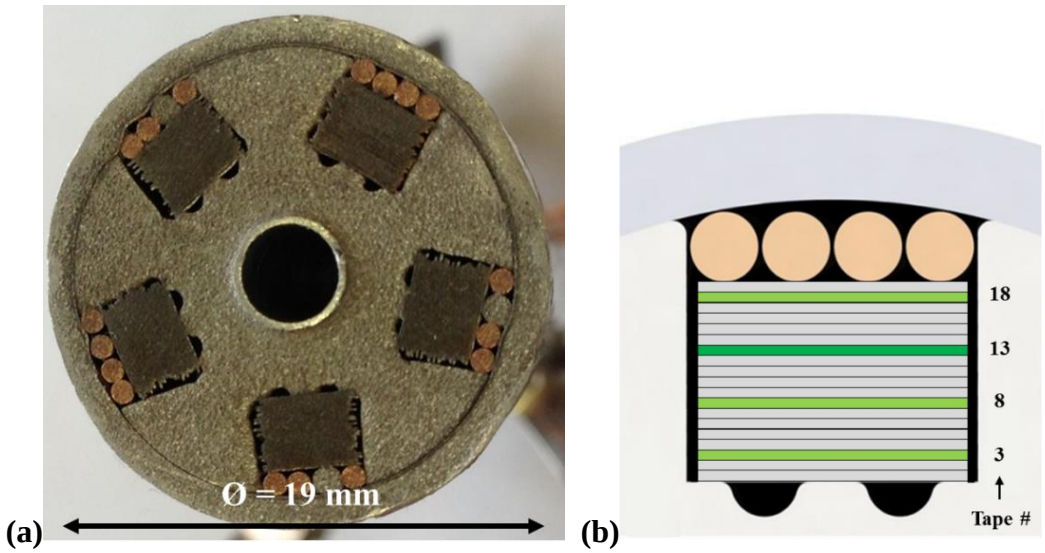

Figure 2.4 – Images of the HTS slotted-core CICC [20]. (a) Cross section of real manufactured cable and (b) schematic of one slot with a stack of nineteen tapes.

2.3 Electromechanical Characteristics

The electromechanical characteristics of a conductor refer to its electrical behavior under mechanical loads. It is well known that the critical current performance of a superconductor, including HTS tapes, is highly dependent on applied stress and strain caused by various loads.

For use in high field magnets, HTS tapes will likely undergo a variety of different loads during cable and magnet fabrication, thermal cool down, magnet energization and operation. These loads include but are not limited to axial tension, torsion, bending and transverse compression as well as combined loads like tension-torsion.

Among other sources, these loads arise from: different rates of thermal contraction in dissimilar materials during cool down (axial); twisting during cable fabrication (torsion); winding of magnet coils (bending); electromagnetic Lorentz forces generated on current carrying conductors in background fields (transverse compression); and hoop forces in energized magnets (tension-torsion).

Therefore, to improve cable processing methods, limit magnet fabrication degradations and maximize their operational performance it is essential to characterize the electromechanical behavior of both individual HTS tapes and full scale cables under the anticipated fabrication and operational loads.

2.3.1 Prior Research

Several experimental studies are available on the electromechanical behavior of single HTS tapes under various loading conditions including axial tension [21]-[27], pure torsion [28]-[32], combined tension-torsion [26]-[27], and transverse compression [33]-[35]. These investigations were conducted at 77 K in self-field on a variety of HTS tapes from various manufacturers including some pre-production tapes. Research at 4.2 K in high magnetic fields is far more limited for single tapes [24],[36]-[37]. Various electromechanical tests have also been conducted on the different HTS cabling methods including CORC, RACC and TSTC. These cables have been evaluated under transverse compression and bending and have also been tested in high magnetic fields under electromagnetic loads [17]-[20],[33],[38]-[41].

Finite element analysis has also been used as an insightful tool to investigate the electromechanical behavior of HTS tapes and cables but to a far lesser extent. Single tapes have been analyzed under axial tension [27],[42], pure torsion [29], combined tension-torsion [27], and transverse compression [27],[43]. Some numerical simulations of HTS cables have also been conducted under bending [43] and transverse compression [40]. The intrinsic strain in single tapes after cool

down from the production process [27] and the intrinsic strain in cables after cool down to operating temperature [43] have also been simulated.

2.4 Scope of Work

This work has focused on characterizing the electromechanical behavior of three commercially available HTS tapes (SuperPower, SuNAM and AMSC) and two cabling methods (TSTC and HTS CICC) under anticipated fabrication and operational loads. The novelty of this work was the combination of laboratory experimentation and numerical finite element modeling. Experiments were used to measure the critical current performance and finite element analysis was used to analyze the strain state of the conductor under various loads.

Single tape experiments were conducted on three types of commercially available HTS tapes under pure torsion [44]-[45], axial tension [44],[46], combined tension-torsion [44],[46]-[47] and transverse compression on their wide face and thin edge [48]. Details and results from the single tape experiments are described in Section 3.0. The single HTS tapes were also analyzed under the same loading conditions using structural finite element analysis. A novel technique was developed for modeling the layered composite structure of the HTS tapes using structural solid-shell elements. Results from the numerical modeling are compared with experimental data for validation in Section 4.0.

In addition to the single tape work, electromechanical experiments on two HTS cabling methods were conducted. The HTS CICC was tested under bending [49] and the TSTC was tested under mechanical transverse compression [48],[50]. Details of the tests and the experimentally determined cable performance are

presented in Section 5.0. Both HTS cabling methods were also analyzed using finite element analysis. A methodology for modeling full scale three-dimensional HTS cables was developed incorporating contact pair relationships for modeling the relative motion between tapes. Specifics of the numerical models and their corresponding electromechanical behaviors are presented in Section 6.0.

A final conclusion of the electromechanical behavior of HTS tapes and cables as determined from experimentation and numerical modeling provided in Section 7.0 along with recommendations for future work.

3.0 Single Tape Experiments

Single tape experiments were conducted on commercially available HTS tapes from three manufacturers: SuperPower, SuNAM and AMSC. Individual tapes from each manufacturer were tested under pure torsion, axial tension, combined tension-torsion load and transverse compression on their wide face and thin edge. Custom experimental equipment for each load type was developed to measure both the critical current as a function of applied load and the mechanical properties of the tapes. All experiments were conducted at 77 K in liquid nitrogen and under self-field conditions (magnetic field generated by the sample). The details and results from the single tape experiments are described in this chapter.

3.1 Pure Torsion

A series of tests to electromechanically characterize single HTS tapes under pure torsion have been conducted [45]. Torsion is a fundamental load in the fabrication of twisted stacked-tape cables. Understanding its effect on single HTS tapes is therefore essential for determining cable fabrication degradations and for developing better cable processing techniques.

A custom probe was developed to simultaneously measure the torque and critical current of single HTS tapes as a function of twist pitch. The probe was used to characterize the performance of HTS tapes from three commercial manufacturers: SuperPower, SuNAM and American Superconductor (AMSC). Specifications of the tapes were provided in Table 2 of Section 2.1. The torque and critical currents of those tapes were characterized over a wide range of torsional strains, down to a twist pitch length of 50 mm.

3.1.1 Experimental Setup

The device used for pure torsion experiments on single tapes is shown in Figure 3.1 [45]. It was designed to simultaneously measure the rotation (twist pitch), torque and critical current of single HTS tapes. The device operates by manually rotating a rod connected to the top of the tape while holding the bottom fixed. The rotation of the top rod corresponds directly to the twist pitch applied to the sample. The rotation of the rod is measured using a potentiometer mounted outside the cryostat. The torque is measured by a 35.5 mN-m low capacity reaction torque sensor (RTS-5 Transducer Techniques) mounted to the bottom of the sample as highlighted in Figure 3.1(b).

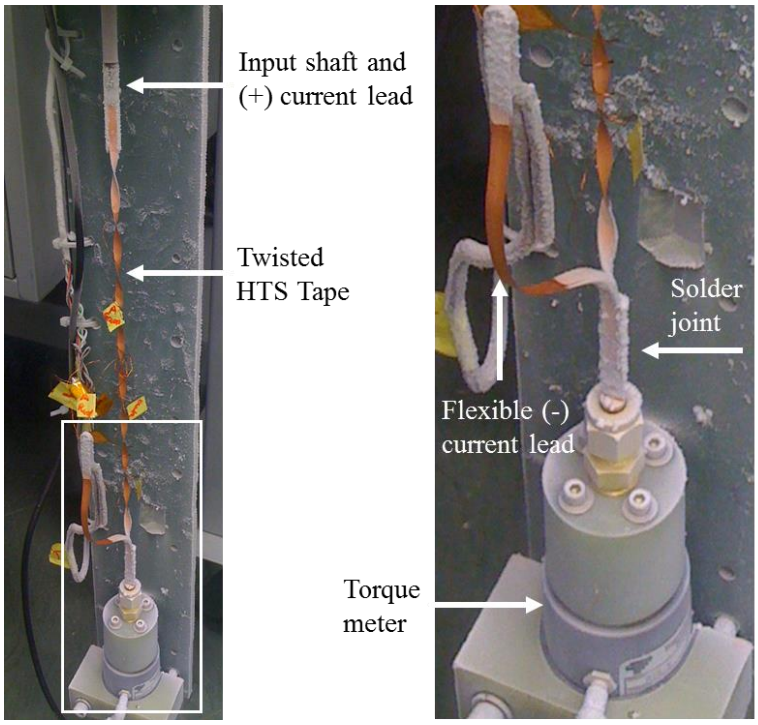

Figure 3.1 – Schematic of the pure torsion experimental device highlighting twisted HTS sample, flexible negative current lead, input rotation shaft and torque meter [45].

The tapes were soldered at the top and bottom to 6.35 mm copper rods. The top copper rod is directly connected to the positive current lead and is used to apply rotation. The bottom copper rod remains stationary and is connected to the

negative current lead via a flexible HTS tape, as shown in Figure 3.1(b). The flexible current lead is necessary to avoid influencing the torque readings since the bottom copper rod is mounted directly to the torque meter.

The device was set up to measure 310 mm long HTS tapes with a twisted sample length of 250 mm. Roughly 30 mm were used for the solder joints on either side. The tapes were also mounted with slack between the copper joints to maintain a pure torsional load as the tap twists. The samples were equipped with two voltage taps (100 mm and 200 mm long) to record the voltage during critical current measurements. The critical current data was calculated with an electric field criterion of 100 μV/m. All measurements were done at 77 K, self-field.

3.1.2 Results

Torque tests down to a twist pitch of 50 mm were performed at room temperature and 77 K for all three HTS tapes: SuperPower, SuNAM and AMSC. Torque was measured using the torque sensor while the twist pitch was calculated from the rotation applied to the potentiometer. The twist pitch refers to the length over which one complete rotation of the tape occurs. The torque magnitudes as a function of the twist pitch for all three tapes at 77 K are shown in Figure 3.2. The plots highlight three incremental twisting cycles. After applying twist, the tapes were completely unwound before starting the next cycle.

The results in Figure 3.2 for all three tapes show an exponentially increasing torque magnitude with decreasing twist pitch length, with a steep increase in torque occurring for twist pitches shorter than 150 mm. The SuNAM tape experienced a slightly earlier torque increase and slightly greater torque

magnitude overall compared with SuperPower. The SuperPower and SuNAM tapes however, were relatively similar as compared to the torque behavior of the AMSC tape which required almost twice the torque to reach the same twist pitch and experienced far more hysteresis (different torque trend) upon unloading. These differences are likely due to the unique substrate materials in each tape, Hastelloy® versus nickel-tungsten, and the method of copper stabilization, electroplating versus laminating.

Figure 3.3 shows the critical current results as a function of twist pitch for all three tapes. The critical current data was taken from the 100 mm long voltage tap located in the center of the sample and was evaluated with an electric field criterion of 100 μV/m. In the figure different cycles are depicted with "up" indicating the increasing rotation (decreasing twist pitch) and "down" indicating decreasing rotation (increasing twist pitch). The lowest twist pitch measured was 50 mm for SuperPower and AMSC and only 80 mm for SuNAM.

As seen in Figure 3.3, the critical current of all three tapes is unchanged down to a twist pitch length of 150 mm. Decreasing the twist pitch further down to 80 mm results in a gradual reversible degradation of critical current. Below a twist pitch of 80 mm, all three HTS tapes experienced steep irreversible degradation of critical current. At a twist pitch of 50 mm the critical current of the Superpower and AMSC tapes was 73% and 70% of their initial values and saw permanent degradation upon unloading. The SuNAM tape repeatedly burned during the critical current measurements at an 80 mm twist pitch on the "2nd up" cycle so no further data could be recorded.

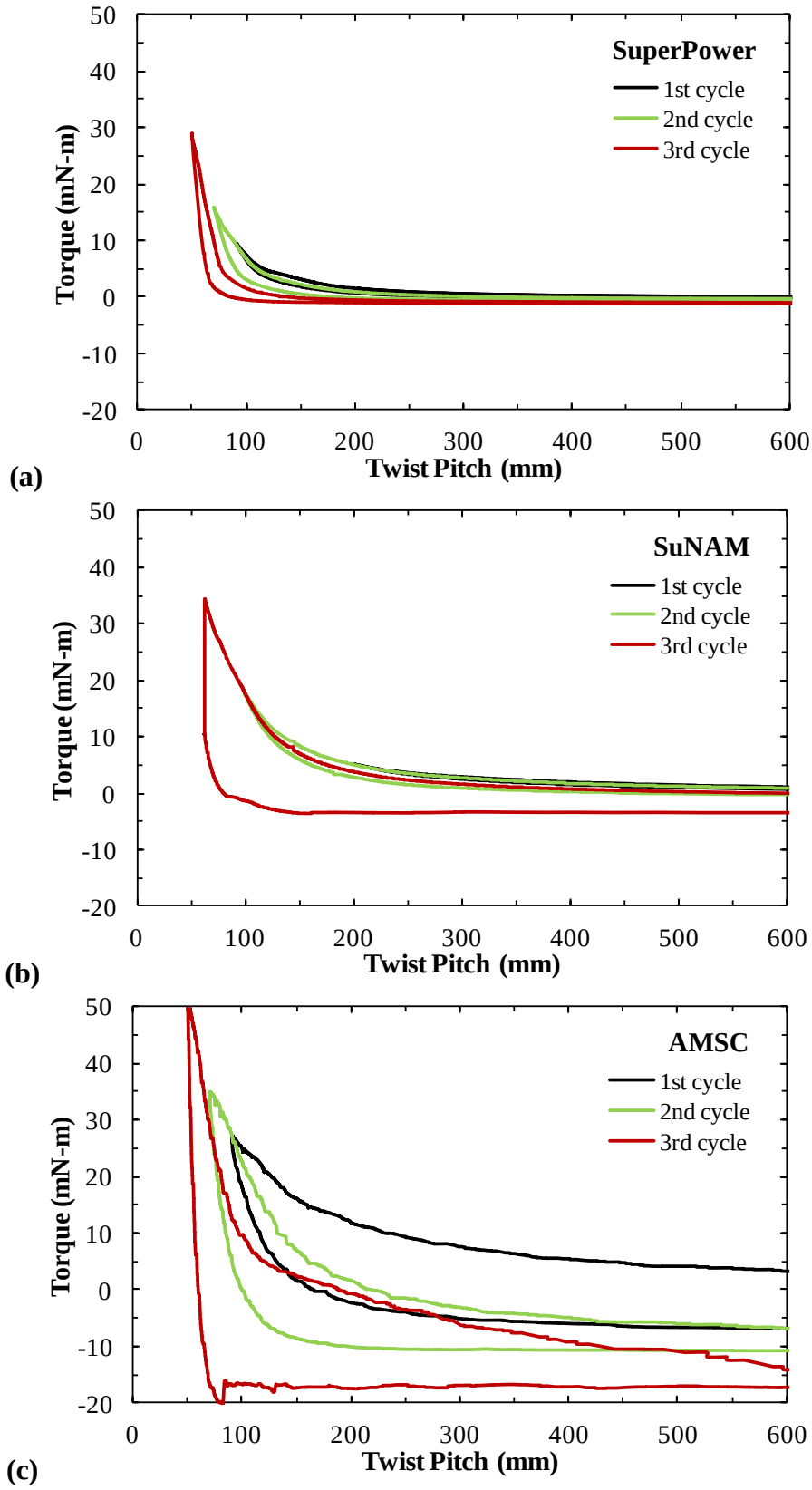

Figure 3.2 – Plot of torque magnitude as a function of the twist pitch for SuperPower (a), SuNAM (b) and AMSC (c) tapes [45]. Measurements taken at 77 K for three load cycles.

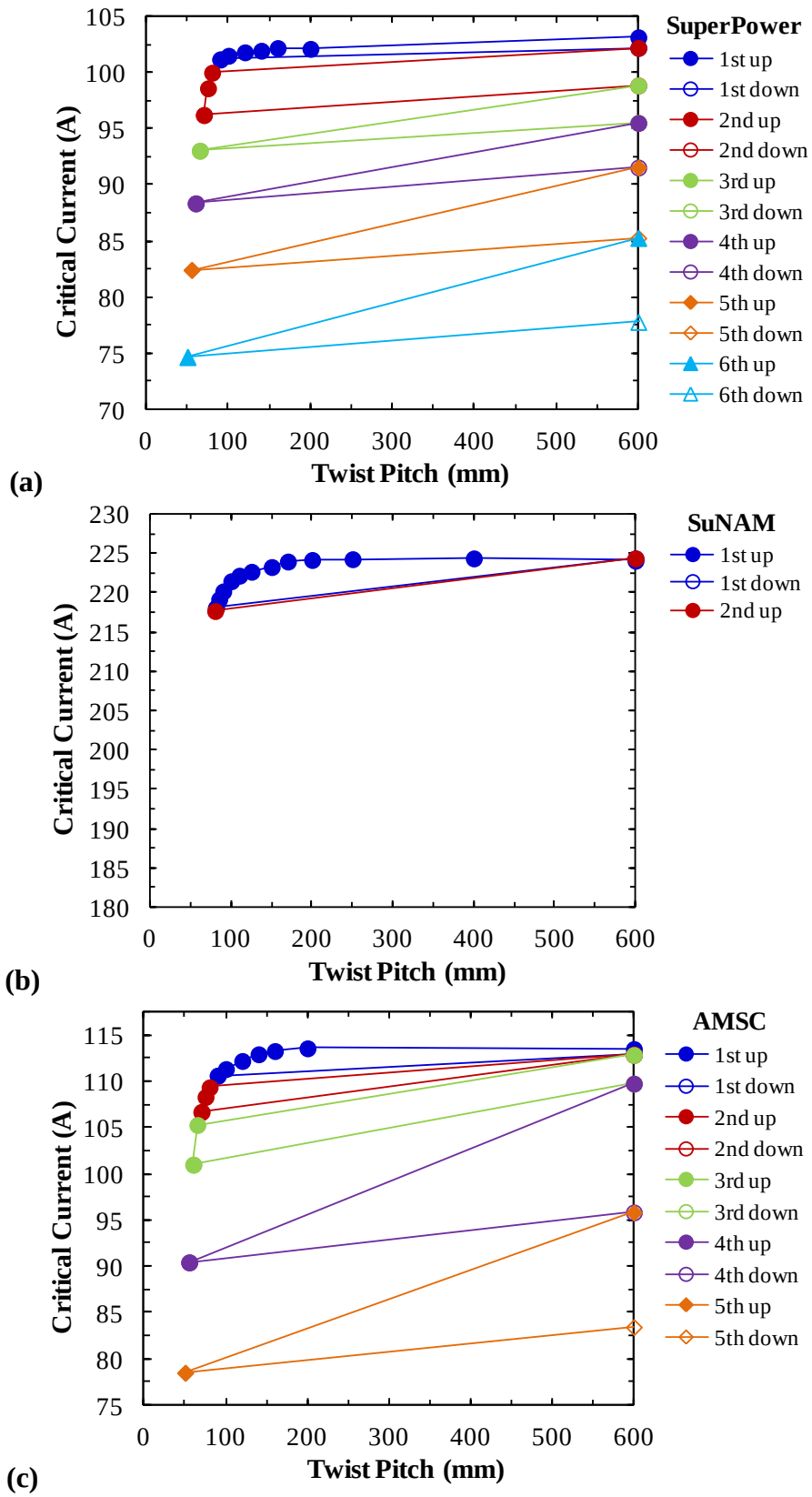

Figure 3.3 – Plot of critical current as a function of the twist pitch length for SuperPower (a), SuNAM (b) and AMSC (c) tapes under pure torsion [45].

3.2 Axial Tension

The mechanical and electrical characteristics of HTS tapes under axial tension have been studied [46]. Axial loads can develop during fabrication, cool down to operating temperatures and magnet operation. It is well known that the critical current of HTS tapes is highly dependent on axial strain particularly from tensile loads. It was therefore imperative to determine the electromechanical behavior of HTS tapes under axial load before integrating them into cables and magnets.

A custom experimental probe was developed to characterize HTS tapes under pure axial tension and combined tension-torsion, as discussed in Section 3.3. The probe was designed to measure both the mechanical stress-strain behavior and the critical current performance of the single tapes under axial tension. Three HTS tapes were tested: SuperPower, SuNAM and AMSC. Their specifications are once again provided in Table 2 of Section 2.1. Stress-strain curves for all three tapes were collected while the critical current behavior of only SuperPower and SuNAM tapes were measured.

3.2.1 Experimental Setup

The test probe used for tension and later combined tension-torsion experiments is shown in Figure 3.4. The probe is designed to simultaneously measure the axial load, elongation, torque and critical current of single HTS tapes in a bath of liquid Nitrogen at 77 K. The probe was used to test 150 mm long tapes having a 100 mm sample length after being mounted. The samples were mounted using stainless steel compression style sample grips.

Axial displacement was applied outside the cryostat through a pull rod by a 1/40 hp permanent magnet DC electric motor (Bison 011-190-0702) and a 10 kN

anti-backlash machine screw actuator (Duff-Norton M5500-124) as shown in Figure 3.4(a). The axial displacement of the sample was measured outside the cryostat by a 15 mm stroke linear variable differential transformer (LVDT, Omega LD621-15). Nyilas-type double extensometers mounted directly on the sample as displayed in Figure 3.4(c) were also used to measure axial displacement [51]. The tensile load was measured outside the cryostat by a precision 1112 N (250 lb) donut style load cell (Futek LTH-350).

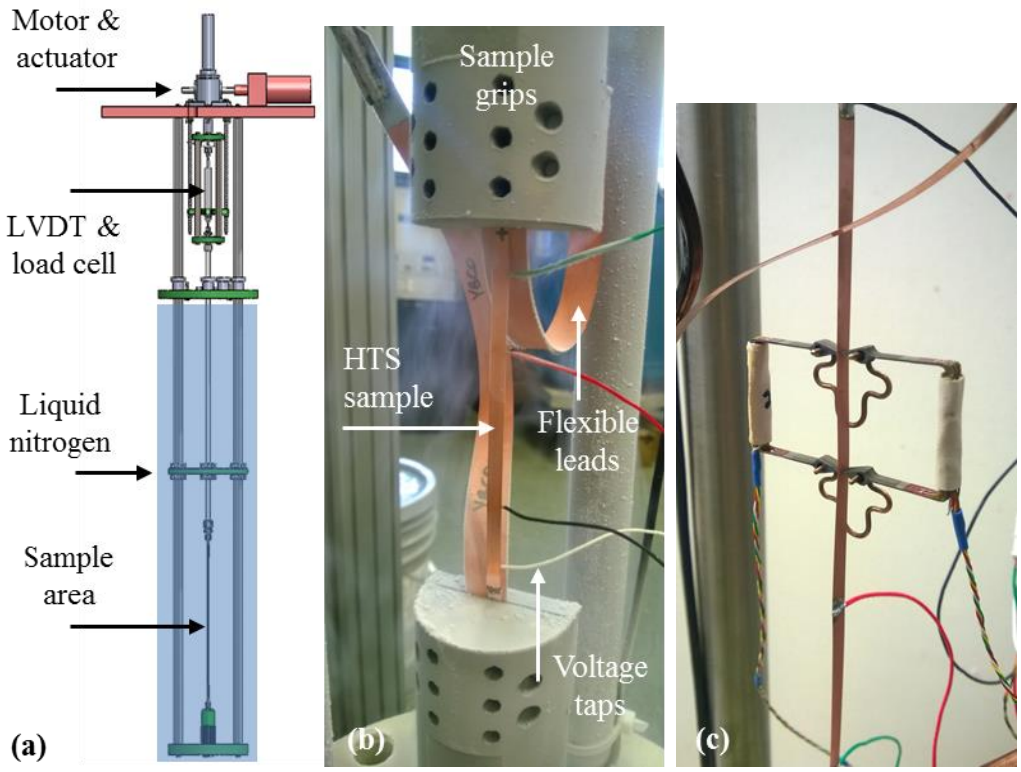

Figure 3.4 – Images of the experimental tensile test probe. (a) Schematic of entire probe, (b) close-up of tensile sample with flexible current leads and (c) double extensometers mounted on sample [46]-[47].

For stress-strain measurements, the samples were axially strained at a rate of roughly 3 mm/min while the load and displacement were simultaneously measured. The tensile load was applied until the tape yielded and started

plastically deforming. The axial strain was then released and the sample was unloaded. No cyclic tests or unloading curves were measured.

For critical current tests, the current was supplied to the samples using two flexible high current 12 mm wide SuperPower tapes as seen in Figure 3.4(b). This method was used so that the current leads would not influence the torque or axial load measurements. Two pairs of voltage taps, 40 and 80 mm long, were used to record the voltage transition during critical current measurements. The primary pair of voltage taps was located in the center of the 100 mm long sample. For the tests, the tensile load was incrementally applied and the critical current was measured at every step. Load was increased until critical current degradation was experienced.

3.2.2 Results

Stress-strain tests were first performed to identify mechanical characteristics of the composite tapes including their yield strength and modulus of elasticity. This information will be used to help validate finite element models of single tapes discussed in Section 4.0. Mechanical stress-strain tests were conducted at room temperature (295 K) and at 77 K in a bath of liquid Nitrogen. The experimental stress-strain curves for all three tapes (SuperPower, SuNAM and AMSC) are shown in Figure 3.5. All three tapes have different dimensions, substrates and stabilizing layers and as a result have very different mechanical characteristics. The experimental data for all tapes was very repeatable and the stress-strain curves presented are averaged from 4 samples of each tape.

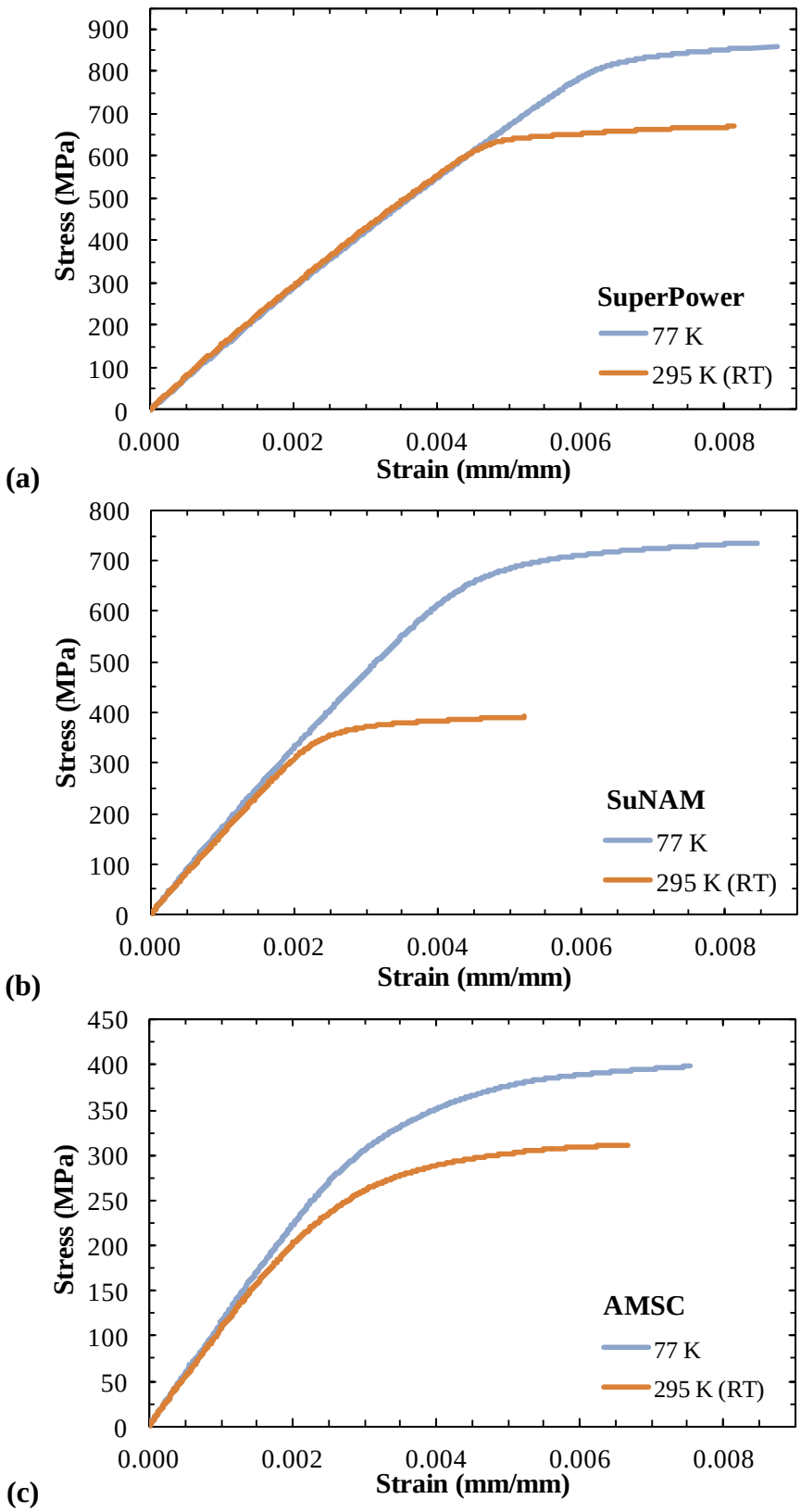

Figure 3.5 – Plots of stress-strain curves for SuperPower (a), SuNAM (b) and AMSC (c) tapes at 77 K and room temperature (RT) [46].

Isotropic bilinear curves were fit to the stress-strain curves of all three tapes and their corresponding modulus of elasticity (E), offset yield strength (Y) and tangent modulus (T) are given in Table 3. The AMSC tape had the lowest modulus of elasticity and offset yield strength of all three tapes. The SuNAM tape had the strongest modulus of elasticity while the SuperPower tape had the highest offset yield strength. The SuperPower tape also had the largest tangent modulus of all tapes. The experimentally determined stress-strain behavior of all three tapes was found to be consistent with other published data [23]-[24], [27].

Table 3 – Mechanical bilinear properties of HTS tapes.

	SuperPower		SuNAM		AMSC	
	77 K	295 K	77 K	295 K	77 K	295 K
E (GPa)	140	145	165	160	115	110
Y (MPa)	825	640	700	372	374	295
T (GPa)	13	8	9	7	6	4

Note: E is modulus of elasticity, Y is offset yield strength and T is tangent modulus.

The difference in the modulus of elasticity of all three tapes at 77 K compared to room temperature was negligible (less than 5%). The offset yield strength, however, was found to be roughly 20% higher at 77 K for SuperPower and AMSC and nearly 50% higher for SuNAM tapes. The tangent modulus also saw an improvement of around 30% at 77 K for all tapes compared to room temperature.

The electromechanical behavior of SuperPower and SuNAM tapes under axial tension was also evaluated by measuring the critical current performance of the tapes under increasing tensile load. The critical currents as a function of applied tensile stress for the two tapes are plotted in Figure 3.6. Both HTS tapes were found to have a gradual and reversible reduction in critical current under

increasing axial tension. This gradual degradation was followed by a steep irreversible degradation of the tapes causing permanent damage upon unloading.

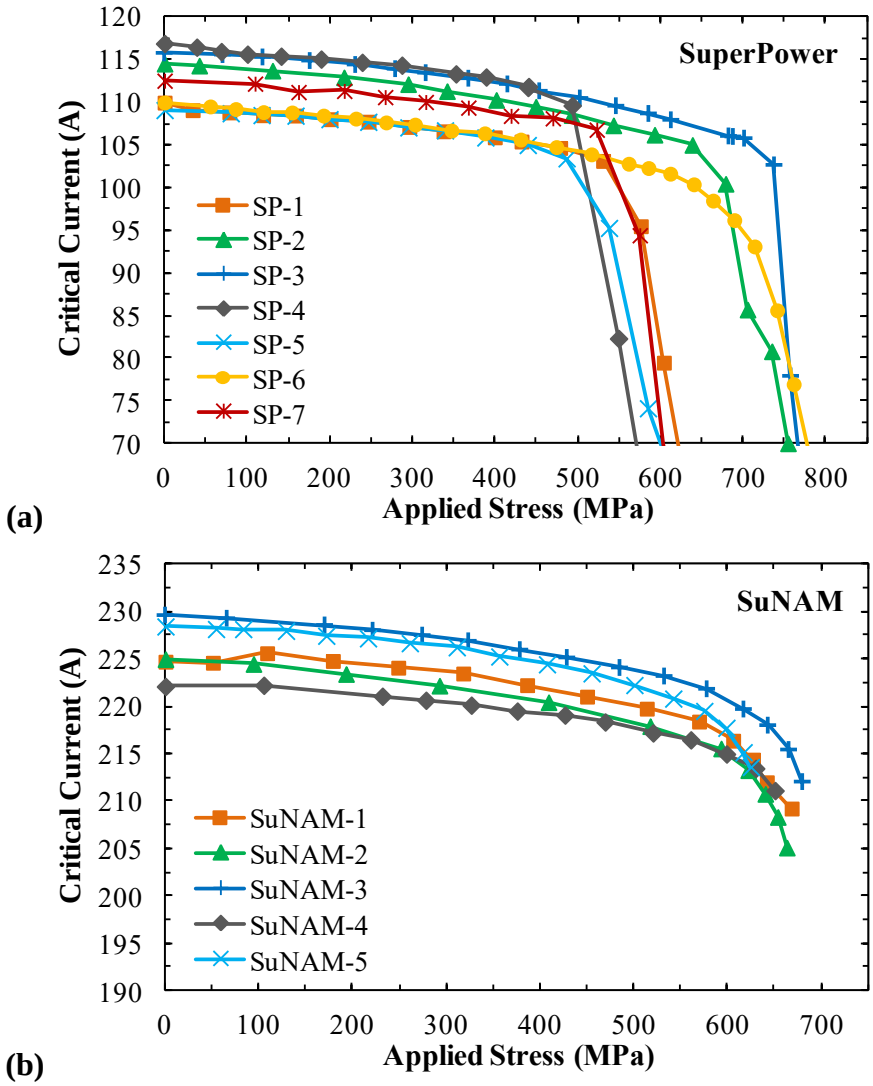

Figure 3.6 – Plots of critical current as a function of axial tensile stress for SuperPower (a) and SuNAM (b) tapes [46]. Measurements were taken at 77 K and in self-field.

The tested SuNAM samples had fairly repeatable critical current behavior. A gradual reduction in critical current was seen up to 650 MPa of applied tensile stress. The sharp critical current degradation occurred approaching a tensile stress of 700 MPa. The SuNAM samples repeatedly burned during critical current measurements just before this stress. By comparison with the stress-strain data in

Figure 3.5 and the mechanical properties in Table 3, a tensile stress of 700 MPa corresponds to the yield strength of the SuNAM tape. This indicates that the steep irreversible critical current degradation in the tape begins near the onset of plastic deformation in the tape.

The SuperPower samples under tension were also expected to see a sharp critical current degradation around their yield strength similar to SuNAM tape and prior literature [23]. As seen in Figure 3.6, all seven of the tested SuperPower samples permanently degraded before reaching the 825 MPa yield strength of the tape. The SuperPower tapes also had large variability between samples with some sharply degrading as early as 500 MPa and others after 700 MPa of tensile stress.

All samples tested from both manufacturers were taken off of the same spool of tape and were prepared and mounted in the same manner. Care was taken during the preparation and mounting to keep everything consistent between samples. Considering this and the fact that the SuNAM tape had more repeatable data, the variability in the SuperPower samples must be real and intrinsic to the tape. A deeper analysis of the tapes looking at their microstructure is required.

3.3 Combined Tension-Torsion

The effect of combined tension-torsion loading on single HTS tapes has been investigated [46]-[47]. Combined tension-torsion is of particular interest for the fabrication and operation of TSTC conductors due to the twisted nature of the design. Among other sources, torsion originates from twisting of the HTS tapes to reduce AC losses and tension stems from different rates of thermal contraction during cool down and electromagnetic hoop forces during a magnet operation.

The combined tension-torsion tests were conducted with the same experimental probe used for axial tension tests as described in Section 3.2. The combined load was applied by first twisting a straight tape to a certain twist pitch and then applying axial tension to the twisted sample producing a combined loading condition. The effect of combined loading on the electromechanical behavior of SuperPower and SuNAM tapes were tested. Their specifications are given in Table 2 of Section 2.1. The experiments measured the torque trend and critical current behavior of twisted tapes as a function of applied load in 77 K, self-field conditions.

3.3.1 Experimental Setup

The device used for axial tension tests, described in Section 3.2.1 and shown in Figure 3.4, was also utilized for the combined tension-torsion tests. For combined loading tests, the probe was adapted to allow the sample to be twisted by rotating the central pull rod. The probe was also adjusted to test longer samples having a twisted sample length of 300 mm. This length was required so that the tension-torsion samples would have at least one full twist pitch along their length. Lastly, the probe was modified to also record torque as the sample was twisted and axially loaded. A close-up image of the modified sample area for tension-torsion tests is shown in Figure 3.7.

For combined tension-torsion tests, the torque was measured by a 71 mN-m low capacity reaction torque sensor (RTS-10 Transducer Techniques) mounted to the base of the probe and affixed to the bottom sample holder. The axial load was recorded by the load cell and the displacement was measured by the LVDT sensor

as done for pure tension tests. The double extensometers were not used to measure displacement since they cannot be mounted to a twisted sample. The LVDT sensor was calibrated with the double extensometers for accuracy.

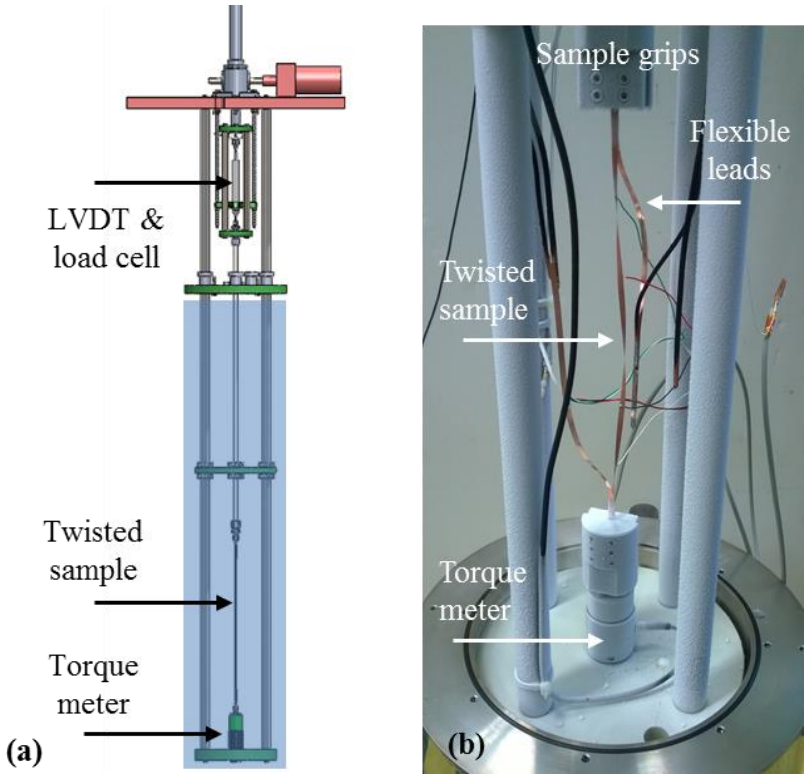

Figure 3.7 – Images of the combined tension-torsion test probe [46]-[47]. (a) Schematic of entire probe and (b) close-up showing twisted sample and torque meter.

For critical current measurements, the current was again supplied to the samples via two flexible HTS tapes, as seen in Figure 3.7, to avoid influencing the torque or axial load measurements. The critical current was recorded using two voltage tap pairs spanning 100 and 200 mm. The voltage-current transition was used to calculate the critical current with a criterion of 100 μV/m. The sample was initially mounted and twisted at room temperature while the subsequent axial loading and critical current measurements were done in 77 K, self-field conditions. The tensile load was applied incrementally and the critical current was evaluated at every step.

3.3.2 Results

The combined tension-torsion results for SuperPower and SuNAM tapes are displayed in Figure 3.8 which plots the critical current as a function of applied tensile stress on the twisted tapes. The tension-torsion tests were conducted first for a 200 mm twist pitch, the current twist pitch of TSTC conductors [18], and then for a 150 mm twist pitch. The experimental data was normalized to the initial critical current of the twisted samples under no axial load. For the twist pitches tested, no critical current reduction is expected just from twisting, based on the pure torsion results of Section 3.1.2. The applied axial stress was determined as the measured load divided by the cross section area.

The combined tension-torsion behavior of both HTS tapes was very similar to that seen in Figure 3.6 under pure axial tension. The tapes had a gradual reduction in critical current under increasing load, followed by a sharp irreversible degradation. The SuNAM samples for a 200 and 150 mm twist pitch were nearly identical and showed degradation starting around 650 MPa and becoming severe by 700 MPa of applied stress. That is the same tensile stress at which the pure tension samples experienced degradation and corresponds to the yield strength of the tape. It should also be noted that under tension-torsion load, a greater critical current degradation was characterized for the SuNAM tapes as compared to the pure tension samples which repeatedly burnt before reaching 700 MPa of load.

The two test SuperPower samples with a 200 mm twist pitch showed noticeable variation in the onset of steep critical current degradation as was found in the axial tension samples. The one tested SuperPower sample with a 150 mm twist pitch fell within the range of the 200 mm twist pitch samples and therefore

can be concluded as experiencing the same critical current behavior. All SuperPower tension-torsion samples experience critical current degradation starting above 650 MPa of stress which match the better performing pure tension samples, possibly indicating a slight improvement in critical current behavior.

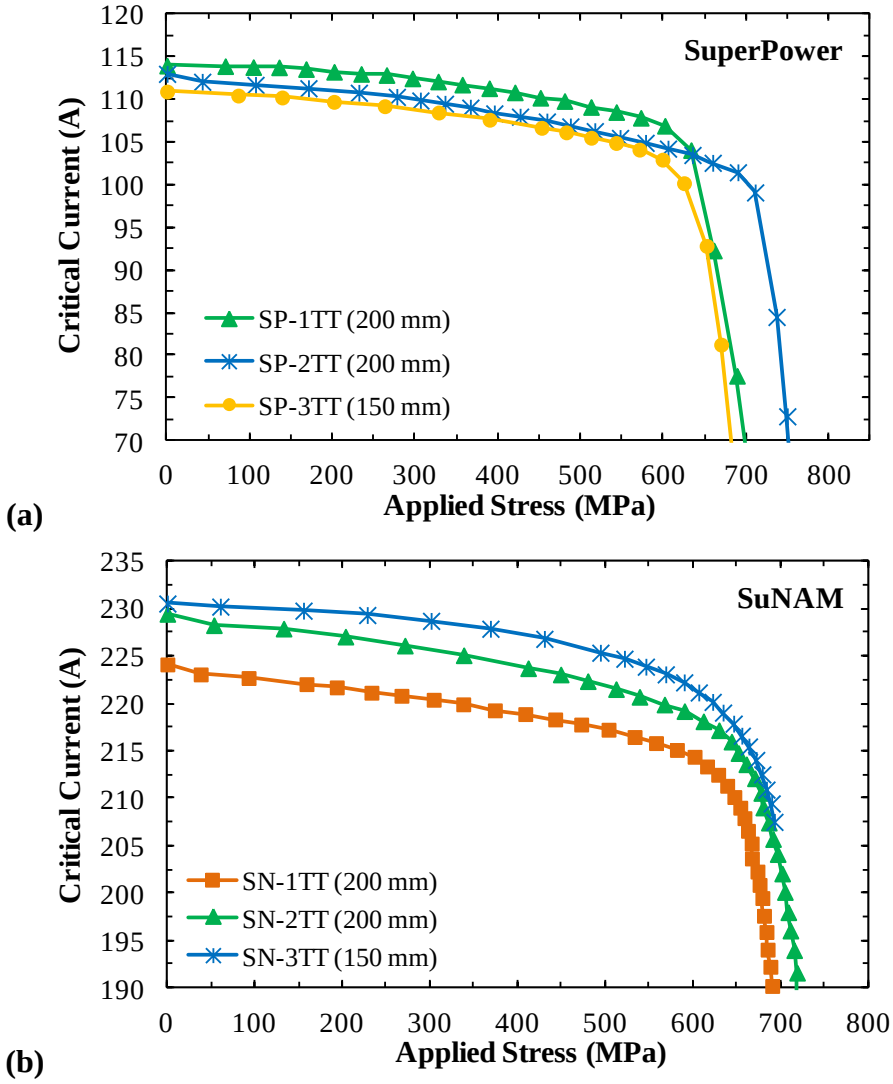

Figure 3.8 – Plot of critical current as a function of applied tensile stress for twisted SuperPower (a) and SuNAM (b) tapes [46]. Sample twist pitch indicated in parenthesis.

Overall, the SuNAM and SuperPower combined tension-torsion results were comparable to the pure axial tension data and may have actually performed slightly better. This indicates that the tensile load is dominant and the effect of the

initial torsion strain was small, for twist-pitch lengths greater than 150 mm, and may have actually improved the critical current behavior slightly.

In addition to the critical current measurements, as the tensile load was applied to the twisted tape the torque was concurrently measured which is something that has previously not been done experimentally. The change in torque as a function of tensile stress on twisted tapes is shown in Figure 3.9.

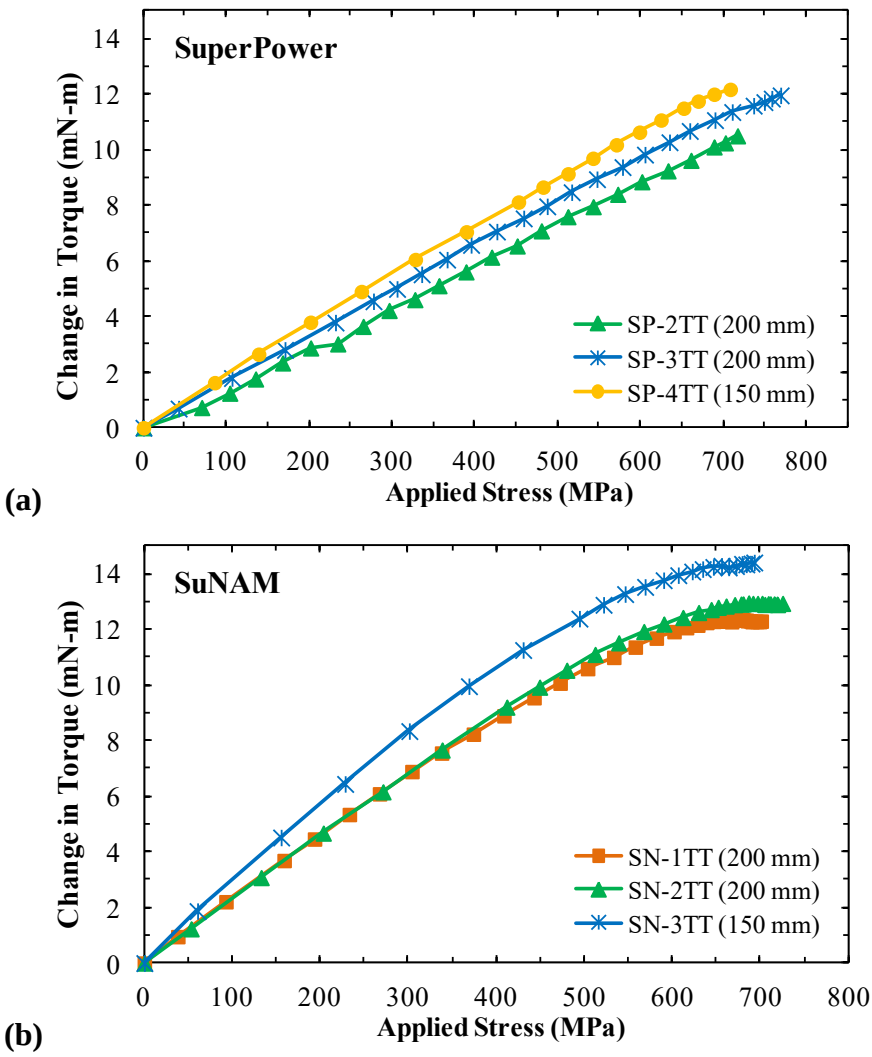

Figure 3.9 – Plot of change in torque as a function of applied tensile stress for twisted SuperPower (a) and SuNAM (b) tapes [46]. Sample twist pitch indicated in parenthesis.

The results from both tapes reveal an intriguing behavior of linearly increasing torque with increasing applied tension. The SuNAM samples also

experienced a noticeable plateau as the tensile stress approached the yield strength of the tape. For the same tensile load the SuNAM tape experienced a greater torque compared to SuperPower which is consistent with the pure torsion results presented in Section 3.1.2. The results from the 150 mm samples of both tapes also indicate that shorter twist pitch samples have greater torsional stiffness (greater increase in torque under tensile load).

3.4 Transverse Compression

The transverse load sensitivity of single HTS tapes on their thin edge and their wide face were investigated [48]. Transverse compression is a typical load experienced by any HTS cable during operation in high magnetic fields due to the natural electromagnetic Lorentz forces which are generated. Since the tapes in a TSTC conductor are twisted along their length it is important to know the effect of transverse load not only on the wide face of the tape but also on its thin edge.

A device was designed to measure the critical currents of tapes and cables at 77 K as a function of transverse load. HTS tapes from two different manufacturers were studied: SuperPower and AMSC. The specifications of the testing tapes were provided in Table 2 of Section 2.1. The transverse load was first applied on the wide face of the tapes so that the functionality of the device could be validated from a direct comparison with prior literature. Transverse compression was then applied on the thin edge of the tapes which has not previously been investigated.

3.4.1 Experimental Setup

The device used for transverse compression experiments on single tapes and cables is shown in Figure 3.10. The transverse load is applied using a

commercially available 10 ton capacity bolt-grip push-puller. As shown in Figure 3.10, the forcing screw is manually rotated such that the central rod is pushed downward transferring a compressive load to the sample area. The central rod has a donut style load cell positioned inside to measure the compressive load applied to the sample during experiments. The load cell is a Futek model #LLW350 rated for 89 kN force and it has a full scale output of 3.0828 mV/V. The downward load from the central rod is transferred to the samples using custom pressing fixtures illustrated schematically in Figure 3.11.

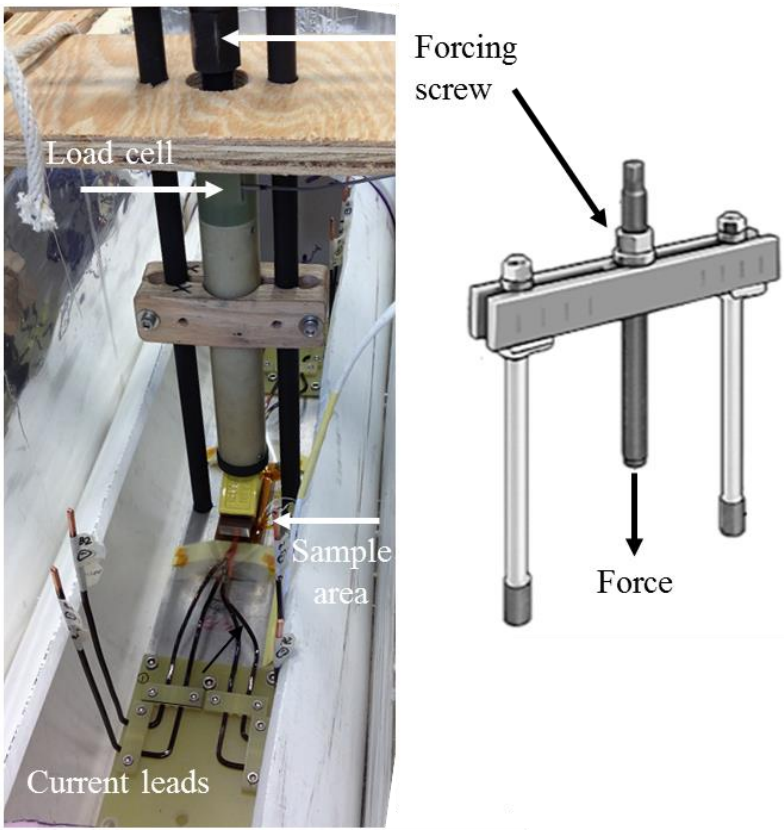

Figure 3.10 – Image of the experimental transverse compression device [48]. The load is applied through a central forcing screw.

Transverse compression on the wide face and thin edge of HTS tapes each required special pressing fixtures which are schematically shown in Figure 3.11. To apply a downward load on the wide face of single tapes (a), two parallel

pressing plates were used. The flat top plate had a 25 mm pressing length and rounded edges to eliminate any stress concentrations on the sample. The plates were wider than the HTS tapes to apply a uniform pressure over the entire tape.

To apply a transverse load on the thin edge of single tapes (b), a custom fixture with a U-shaped bottom channel and a T-shaped top plate was used. The T-shaped plate had a 2.0 mm wide and 2.4 mm deep groove machined in the bottom to position the tapes. Multiple tapes were placed in the groove vertically as shown in Figure 3.11 and two copper strips were added on either side to fill the channel and provide stabilization. The HTS tapes partially extended (less than half their width) outside the groove of the T-shaped top plate and sat on the bottom of the U-shaped channel, solely supporting the applied load. The pressing length of the fixture was 170 mm.

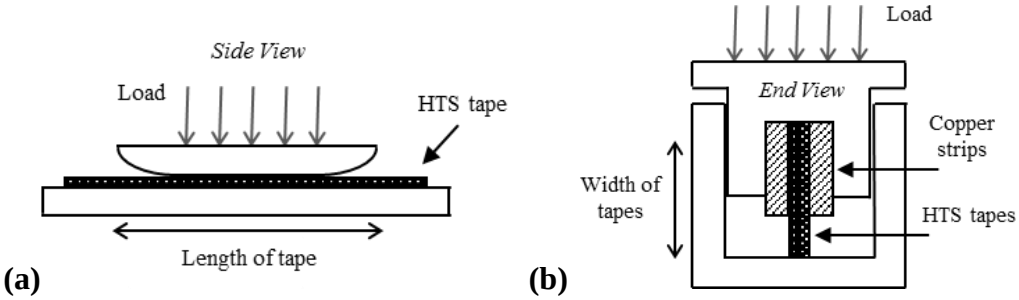

Figure 3.11 – Schematic of transverse compression pressing fixtures. (a) Side view of wide face compression and (b) end view of thin edge compression.

The current was fed to the sample through copper current leads as shown in Figure 3.10. A 220 ampere Agilent 6671A power supply was used for the experiments. All samples were equipped with voltage taps soldered directly on to the REBCO side of the HTS tapes. The voltage taps were used to measure the critical current as a function of the load applied. A voltage tap length of 50 mm and 175 mm were used for the wide face and thin edge samples respectively. The

critical current data was evaluated at an electric field criterion of 100 μV/m. All the measurements were performed at 77 K and self-field conditions.

3.4.2 Results

For both transverse load tests, the critical current data is shown as a function of the average applied pressure in MPa. The average pressure was calculated as the applied force divided by the pressed area. The applied force was directly measured by the load cell and the pressed area was evaluated as the length pressed multiplied by the average thickness or width of the HTS tapes depending on the experiment. The average tape dimensions used in the calculations are provided in Table 2 in Section 2.1.

The first set of experiments tested transverse compression on the wide face of single tapes from SuperPower (SP) and American Superconductor (AMSC). The critical current results as a function of applied load are presented in Figure 3.12. As expected from published literature [33]-[34], the critical current of the SuperPower tape did not show any degradation up to a compressive stress of 450 MPa. Characterization of critical current under larger compressive loads was not feasible with our experimental device.

The AMSC tape in comparison experienced a gradual reversible reduction in critical current up to 400 MPa of stress followed by a sharp irreversible degradation. The ASMC tape had 13% critical current degradation at 470 MPa and a permanent degradation of 9% upon unloading. No prior literature for the AMSC tape under transverse load is available for comparison.

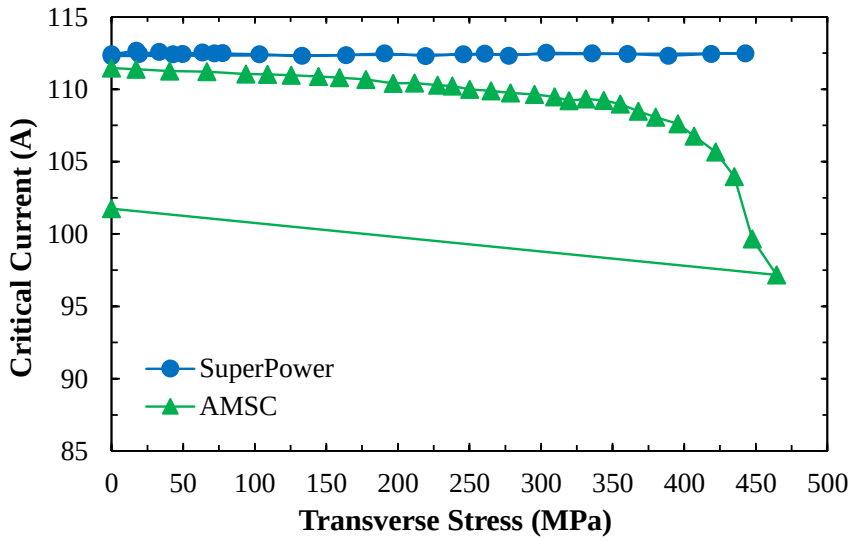

Figure 3.12 – Plot of critical current as a function of transverse compressive stress on the wide face of single HTS tapes [48].

The second set of experiments tested transverse compression on the thin edge of single HTS tapes from the same two manufacturers. Figure 3.13 shows the critical current results as a function of applied load for AMSC tapes (a) and SuperPower tapes (b). Two AMSC tapes were tested in one experimental and four SuperPower tapes in another (results are only shown for two for clarity).

As evident in Figure 3.13, the critical current is far more sensitive to transverse compression applied on the thin edge compared to compression applied to their wide face as shown in Figure 3.12. The critical loads before sharp irreversible degradation under transverse compression on the thin edge was approximately 165 MPa and 130 MPa for AMSC and SuperPower tapes respectively.

Critical current degradation for AMSC tapes started as early as 60 MPa in one sample and 150 MPa for the other. Both samples experienced severe irreversible degradation as high as 60% at a final load of 200 MPa. Critical current degradation for SuperPower tapes began around 90 MPa of compressive stress

and all samples experienced a sudden and severe permanent degradation of critical current after a stress of 135 MPa.

The sudden irreversible degradation of critical current in all samples is likely caused by buckling and in some cases delamination as visually observed after the experiments. The variability in critical current behavior observed among the samples may be caused by a non-uniform load applied to each caused by a slight misalignment of the tapes.

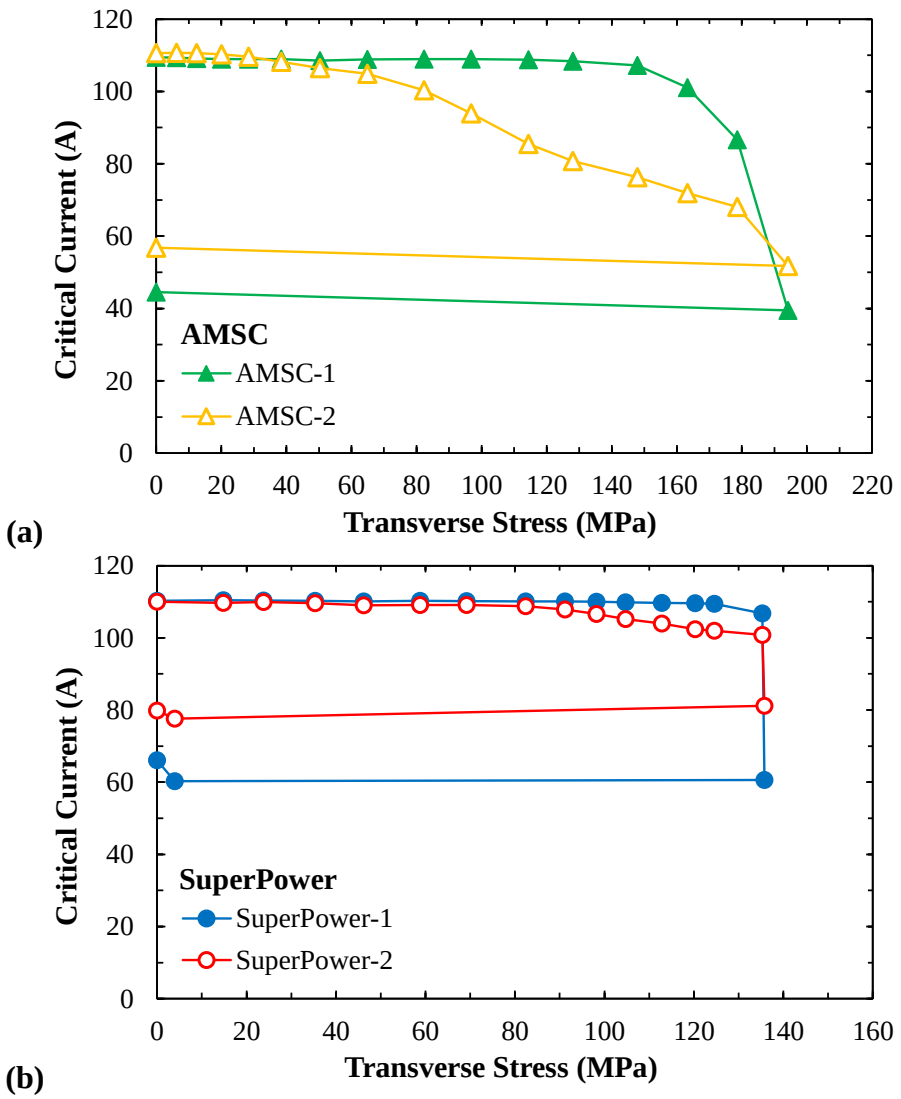

Figure 3.13 – Plot of critical current as a function of transverse compressive stress on the thin edge of (a) AMSC and (b) SuperPower tapes [48].

3.5 Summary and Future Work

The electromechanical characteristics of single HTS tapes from three commercial manufacturers (SuperPower, SuNAM and AMSC) were tested under various loads including pure torsion, axial tension, combined tension-torsion and transverse compression on their wide face and thin edge.

Under pure torsion HTS tapes saw a slight reversible reduction in critical current for twist pitches below 120 mm followed by a sharp irreversible degradation below 80 mm. The mechanical torque characteristics of each tape were different but all experienced an exponential increase in torque for decreasing twist pitch length.

Under axial tension the tested HTS tapes were found to have a slight reversible critical current degradation under increasing tension, followed by a steep irreversible degradation beginning near the onset of plastic deformation as determined from their experimental stress-strain curves. SuNAM tapes experienced fairly repeatable critical current degradation at their yield stress while the SuperPower tapes had large variability between tested samples and experienced critical current degradation below their yield strength.

Under combined tension-torsion load HTS tapes were found to have nearly identical critical current behavior to pure tension samples for the tested twist pitch lengths. This indicates that the tensile load is dominant and the effect of the initial torsion strain is small for twist-pitch lengths greater than 150 mm. The general torque characteristics were found to linearly increase with applied tension on twisted tapes and were found to increase at a greater rate for shorter twist pitch samples.

Under transverse loads single HTS tapes were found to be far more sensitive to compression applied on their thin edge compared to compression applied to their wide face. AMSC and SuperPower tapes both experienced severe critical current degradation around 150 MPa of stress on their thin edge, while had no irreversible degradation above 400 MPa of stress on their wide face.

Overall the difference found between the three tapes under the various loads is likely caused by their differences in layered composition and manufacturing processes. The material type and thickness of their substrate along with the thickness and type of copper stabilization seem to have the most influence on the electromechanical characteristics of the tapes under the tested loads.

Future work for single tape experiments under all four loads includes characterizing more samples from each tape manufacturer to obtain better overall statistics and more accurate electromechanical results for comparison with finite element analysis. In addition, the critical current behavior of the AMSC tape under tension and combined tension-torsion as well SuNAM tape under the transverse compression still need to be characterized. More twist pitch lengths should be tested for the tension-torsion load to validate the numerical results.

The SuperPower tension and combined tension-torsion results also need to be investigated further to try and identify an exact cause for the lower critical current performance that was experienced compared to prior literature. This investigation could include testing more samples including samples from a newer spool of tape. Other investigations could include investigating the microstructure of the REBCO layer for micro-cracks after testing and altering the testing protocol.

4.0 Single Tape Modeling

Structural finite element analysis was conducted on the same three HTS tapes (SuperPower, SuNAM and AMSC) characterized experimentally and under the same type of loads: pure torsion, axial tension and combined tension-torsion [44],[46]-[47]. A novel technique was developed for modeling the layered composite structure of the HTS tapes using structural solid-shell elements. For each type of load the corresponding mechanical characteristics (deformation, torque, strain and stress) were analyzed and evaluated against measured data for model validation. The axial strain in the superconducting layer of the HTS tapes was also analyzed as a function of applied load and paired with an analytical model to estimate the critical current behavior of the tapes. The details of the finite element models and their corresponding results are described in this chapter.

4.1 Finite Element Analysis

The electromechanical behavior and mechanical properties of HTS tapes under various loads were studied using commercial finite element analysis (FEA) software from ANSYS®. Full three-dimensional numerical models of single tapes were developed. The layered composite structure of the HTS tapes was modeled using structural solid-shell elements. Separate numerical models with unique geometry and layered-characteristics were created for SuperPower, SuNAM and AMSC tapes. Specifications of the tapes are provided in Table 2 of Section 2.1.

The numerical models of single HTS tapes were analyzed under three different loading conditions: pure torsion, axial tension and combined tension-

torsion. Each applied load in the finite element model was representative of the loads applied during experiments for comparison.

The HTS tapes were set up to have a completely strain free initial condition and neglected the compressive internal residual strain which develops in the superconducting layer after the tape production process due to differences in thermal contraction of the various constituent materials in tapes [27].

All numerical simulations were run as static non-linear analyses with large deformation and enhanced strain formulations. The simulations were calculated using a Newton-Raphson integration technique and automatic time stepping to increase convergence.

The mechanical characteristics and the estimated electrical performance determined from the finite element simulations were validated against prior experimental data discussed in Section 3.0. The electrical performance was estimated from the structural model using the axial strain of the superconducting layer and an analytical model.

4.1.1 Solid-shell elements

A novel method was developed to model the layered structure of HTS tapes in ANSYS® using solid-shell elements, where the tapes are meshed with one element through their thickness and their layered architecture is defined within the finite elements. This modeling was done in ANSYS® using the SOLSH190 structural solid-shell element. It is an eight-node hexahedron “brick” element possessing continuum solid element topology, for simplified geometric modeling, and internal shell element capabilities, for modeling thin composite structures. A

schematic illustration of the SOLSH190 element is shown in Figure 4.1. The composite behavior and interlayer interactions are handled within the finite element formulations, eliminating the need for contacts between layers.

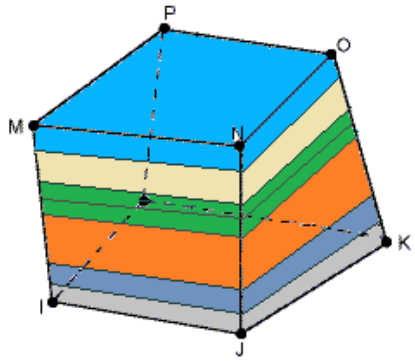

Figure 4.1 – Schematic illustration of the SOLSH190 solid-shell finite element. The colors indicate different layers defined within the element.

When using solid-shell elements, the layered structure of the HTS tape is first modeled simply as one homogeneous geometric volume as depicted in Figure 4.2. The homogeneous tape volume is then discretized with only one finite element through its thickness. Lastly, the number, order, thickness and material properties of each layer are defined within the finite elements using shell section commands. The use of shell section commands to define the layered structure of the tapes allows the finite element models to be easily customized to the exact composite architecture of each type of HTS tape from SuperPower, SuNAM and AMSC.

The characteristics of the solid-shell elements greatly simplify the modeling of the thin layered composite architectures of HTS tapes as compared to using shell or solid elements. The results from solid-shell elements also tend to be more accurate (better fit to analytical data) due to their unique finite element formulations. The computational time required to complete a simulation can also be significantly reduced using solid-shell elements. One limitation of using solid-

shell elements is the inability to model permanent degradation in the form of delamination of the tapes or fracturing of the brittle superconducting layer.

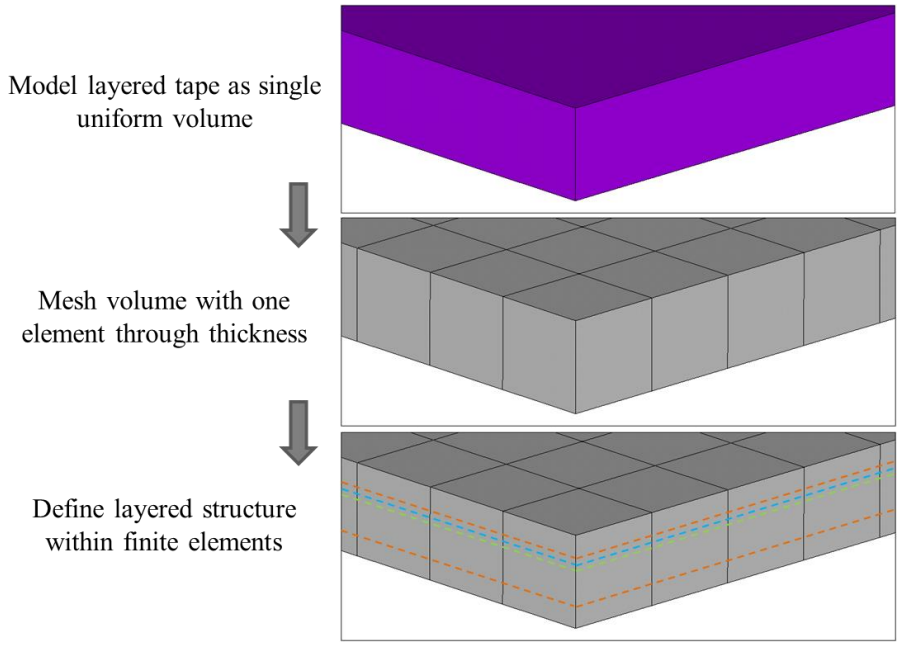

Figure 4.2 – Schematic depiction of how a composite HTS tape is modeled using solid-shell elements. The internal structure depicted by dashed lines.

4.1.2 Mesh density

SOLSH190 solid-shell elements have a hexahedron "brick" shape which is the most tolerant element topology to high aspect ratios which makes them ideal for meshing the slender rectangular tape geometry. Additionally, the similarity of the brick element and tape geometries permits the use of mapped (structured) meshing which allows a more uniform patterned mesh to be used.

Using solid-shell elements requires the tape geometry to be meshed with only one element through the thickness, so that the layered structure can be defined within the element. Although, only one element is used through the thickness of the tape geometry, the accuracy through the thickness of the tape can be improved by increasing the number of integration points defined in each layer of the tape which is equivalent to increasing the mesh density.

Sufficient mesh density through the width and thickness of the tape was determined through a mesh study and varied depending on the load type and accuracy needed. The finite element size was reduced while the computation time and the accuracy of strain results compared to analytical models were monitored. The mesh density was chosen to produce an accurate strain profile through the width of the tape under pure torsion. This was done since pure torsion produces the most variation in strain through the width of the tape. The mesh was optimized for the strain considering it is used to estimate the critical current behavior of the tape. The accuracy of the mechanical deformation and reaction loads were also studied during the mesh analysis.

For single tape models, 20 elements through the width of the tape was determined adequate while more than 40 elements was deemed excessive due to long computation times with insignificant improvements in accuracy. An element length-to-width ratio of 2 selected as ideal so that the relatively long length of the tapes compared to the width could be meshed with less elements without causing shape violations or result inaccuracies. A representative finite element discretization of an HTS tape is shown in Figure 4.3.

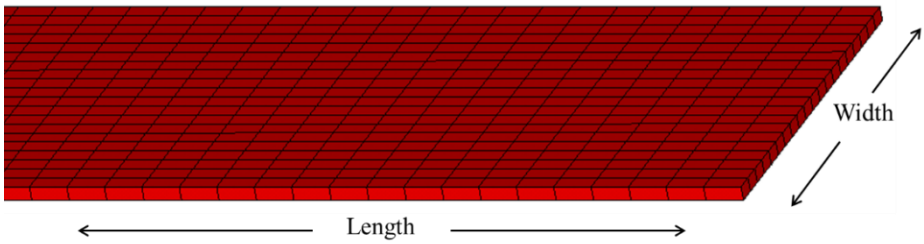

Figure 4.3 – Image of a typical finite element mesh having 20 elements through the width, a length-to-width ratio of 2 and one element through the thickness.

The average mesh density used for the single tape finite element models was: one element through the thickness (solid-shell requirement), 32 elements through

the width and 200 elements along the length for a total of 6,400 elements and over 13,000 nodes. The mesh was chosen to produce reliable and accurate strain results under all three loads (tension, torsion and combined tension-torsion) while having an efficient computation time.

4.1.3 Material Properties

The resulting behavior of any numerical model is highly dependent on the choice of material properties. Therefore, defining accurate material properties for each layer of the HTS tape is critical to successfully modeling the composite behavior of the tapes under load.

The three main structural components of an HTS tape are the substrate (Hastelloy®, stainless steel or nickel-tungsten), superconducting REBCO layer and surrounding copper stabilizer. These materials within an HTS tape are expected to experience both elastic and plastic deformations under fabrication and operational loads. To accurately simulate the elastic-plastic behavior of the HTS tapes, nonlinear material properties for each layer must be defined. A classical bilinear isotropic hardening model was used which defines two slopes (elastic and plastic) to represent the full stress-strain curve of the material being modeled. A schematic illustration of a bilinear material curve is depicted in Figure 4.4 and is defined by a modulus of elasticity, offset yield stress and tangent modulus.

The 77 K properties of each constituent material of an HTS tape used in the ANSYS® modeling of the three tapes are provided in Table 4. The modulus of elasticity (E), offset yield strength (Y) and tangent modulus (T) values were taken directly from stress-strain data at 77 K when available. The properties listed in the

table were chosen based on data from the tape manufacturer when available and from published literature when not.

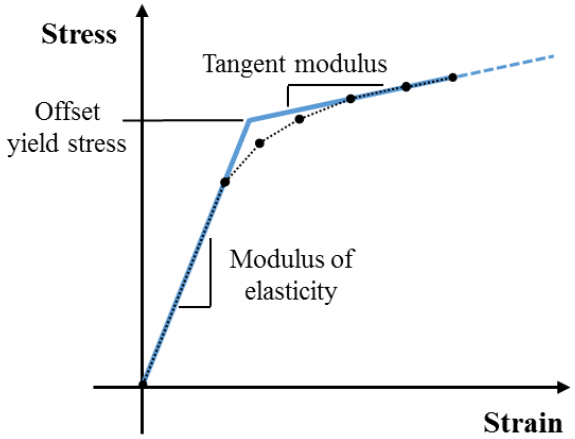

Figure 4.4 – Schematic of an isotropic bilinear stress-strain curve used to define nonlinear elastoplastic material properties in the structural finite element models.

Considering their small influence on the mechanical characteristics of the tapes, the same REBCO/buffer, and silver properties were defined for all tapes for consistency. One of the main differences between the tapes is the substrate material; Hastelloy® for SuperPower, stainless steel for SuNAM and nickel-tungsten alloy for AMSC. The second main difference is the thickness and method used for copper stabilization; electroplating for SuperPower and SuNAM and laminating for AMSC.

Table 4 – Material properties for HTS tapes used in the finite element models.

Material		E (GPa)	Y (MPa)	T (GPa)	References
Substrate	Hastelloy® C-276	180	1225	7.5	[23],[27],[52]
	Stainless Steel	190	850	10.0	[52]-[53]
	Ni-5AT.%W	120	255	3.75	[54]-[55]
Copper	Electroplated	85	350	4.0	[23],[27]
	Rolled	120	455	4.5	[56]-[59]
Silver Overlayer		90	225	22.0	[58]-[60]
REBCO/Buffer		150	---		[60]-[62]

Care was taken to use the most accurate material properties for the substrate and stabilizing materials because they comprise the majority of the tape volume and as a result govern the overall mechanical behavior (strength) of the tape. The buffer and REBCO layers have brittle ceramic characteristics and therefore, were modeled with linear elastic properties, assuming no fracture. Elasticity was chosen for the superconducting layer because brittle materials tend to fracture instead of plastically yielding.

In order to validate the material properties used to model the composite HTS tapes, their composite stress-strain behavior was analyzed numerically and compared to the experimental stress-strain curves measured in Section 3.2 and shown in Figure 3.5.

4.1.4 Boundary Conditions

Torsion was applied in the numerical model in the same manner as done experimentally: one end of the tape was held fixed while the other was rotated twisting the tape. The rotational degrees of freedom were applied in the finite element model using multipoint coupling constraint contact pairs defined on each end of the HTS tape geometry. The constraints were defined to have all the nodes on the end area of the tape constrained to the degrees of freedom of one “pilot” node in the center of the tape cross section as depicted in Figure 4.5. Therefore, any displacement or rotations applied to the pilot nodes will also be applied to the ends of the tape.

Tension was applied to the tape as an outward facing uniform surface pressure on both ends of the tape. The pressure was applied incrementally as was done in

the experiments. For a combined tension-torsion load, the tape was first twisted down to a desired twist-pitch by applying rotation to the pilot node constraints. The twisted tape was then loaded under increasing axial tension as was done in the experimental combined load tests.

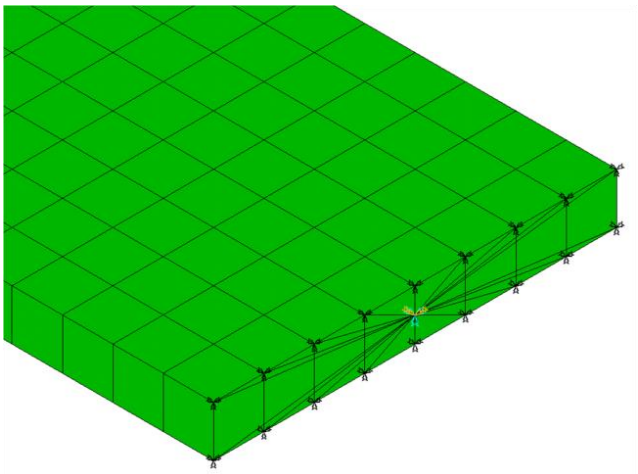

Figure 4.5 – Image of a pilot node multipoint coupling constraint applied on the ends of the HTS tapes in the finite element models.

4.1.5 Critical Current Estimation

The critical current of HTS tapes is known to be highly dependent on the axial strain in the conductor. The axial strain dependence of the critical current for SuperPower tapes has been well characterized experimentally [63]. This experimental critical current as a function of axial strain behavior was used to estimate the electrical performance of HTS tapes in the structural finite element models. The normalized critical current was calculated from the numerical axial strain data using the following steps [64].

Step 1: *Define an analytical relationship for the critical current as a function of axial strain.* The axial strain in an HTS tape under torsion and tension loads is constant through its thickness and along its length but typically varies through its width, especially under torsion. Since the axial strain may not be constant through

its width, the critical current (I_c) of an HTS tape under load was described by an integration of critical current densities (j_c) over the tape width ($2w$),

$$I_c = t\int_{-w}^{w} j_c(\varepsilon_x)\, dx \tag{1}$$

where t is the thickness of the tape and ε_x is the axial strain. The critical current density as a function of axial strain was obtained from measured experimental critical current results in Step 2. The axial strain through the width of the tape was determined from the finite element models in Step 3.

Step 2: *Characterize experimental critical current data as a function of axial strain with an analytical equation.* Published experimental critical current data as a function of applied axial tensile/compressive strain for SuperPower HTS tapes was used [63]. The experimental normalized critical current behavior (I_c/I_o) was approximated by the following sixth order polynomial equation,

$$\begin{aligned} I_c/I_o(\varepsilon_x) = {} & (0.057713 * 10^{12}){\varepsilon_x}^6 - (0.03979215 * 10^{10}){\varepsilon_x}^5 \\ & - (0.2090279 * 10^8){\varepsilon_x}^4 + (0.02385557 * 10^6){\varepsilon_x}^3 \\ & - (0.1668065 * 10^4){\varepsilon_x}^2 - (0.003662115 * 10^2)\varepsilon_x + 1 \end{aligned} \tag{2}$$

where ε_x again represents the axial strain in the HTS tape. This normalized critical current was then be used to define the critical current density using the following relationship where t is the thickness and $2w$ is the width of the tape,

$$j_c(\varepsilon_x) = \frac{I_c/I_o(\varepsilon_x)}{t * 2w}. \tag{3}$$

Step 3: *Use finite element analysis to determine the axial strain through the width of the tape.* Structural finite element analysis of single HTS tapes was conducted to identify the axial strain in the tapes under various loads, including

torsion and tension. More specifically the numerical models was used to identify the axial strain in the superconducting REBCO layer of the HTS tapes. To estimate the critical current from the numerical model, the axial strain through the width of the tape was recorded at weighted Gaussian points.

Step 4: *Conduct a numerical Gaussian integration of equation (1) to estimate the normalized critical current*. The normalized critical current in the HTS tape under load was determined by the integration of equation (1) which was carried out by the Gaussian integration method of order forty using Microsoft Excel®. The integration was done using the numerical axial strain results determined in Step 3 and the analytical expression for the experimental critical current behavior found in Step 2. Additional details of the analytical model in [64].

Considering the structural model of the HTS tapes has a linear behavior for the superconducting layer with no fracturing, the critical current was evaluated in the analytical model for strains up to ±1.5% which is outside the range of experimental data. Estimating the critical current in this manner is a best case scenario and assumes no micro-cracking or fracturing of the superconducting layer [65]. The predicting critical current behavior in this fashion will therefore likely over predict the electrical performance of the tapes.

4.2 Pure Torsion

The mechanical and electrical characteristics of single HTS tapes have been analyzed under pure torsion using finite element analysis [44],[47]. Torsion is a critical load placed on tapes during the fabrication of TSTC conductors and therefore is an important load for determining cable fabrication degradations.

The numerical analysis investigated the behavior of HTS tapes from the same three manufacturers as tested experimentally: SuperPower, SuNAM and AMSC. The specifications, layered architecture and dimensions of the three tapes are provided in Section 2.1. The simulations analyzed the tapes down to a minimum twist pitch of 50 mm and were used to identify the deformed shape of the twisted tapes, the axial strain distribution through the width of the tape and the composite torque characteristics.

4.2.1 Model Details

Pure torsion models were set up and run for all three HTS tapes. The models had a tape length of only 50 mm as compared to the 250 mm twisted length of the experimental samples. The shorter length of the tape was simulated to reduce the size and computational time of the numerical model. The shorter length was accurately modeled using “symmetry style” end conditions which prescribe the ends of the tape to remain planar while permitting them to move freely in the axial direction.

The pure torsion load was applied as axial rotations on the ends of the tapes using pilot node constraints as described earlier and shown in Figure 4.5. One end was constrained not to rotate while the other end was rotated in steps down to a final twist pitch of 50 mm. One end of the cable was also constrained axially while the other remained free, allowing the tape to shorten as it is twisted ensuring a pure torsion condition was achieved.

For every rotational load step the resulting moment (torque) on the end of the sample was recorded. The axial strain through the width of the sample was also

recorded at every step. The strain data was taken at 40 Gaussian points and was used to estimate the critical current performance of the tape as a function of sample twist pitch. The strain results were taken from the center of the tape to avoid any end effects. Results were compared and validated against the experimental results presented in Section 3.1.2.

4.2.2 Results

The mechanical torque results determined from the finite element analysis were first evaluated against the experimental data to validate the mechanical behavior of the composite tape model and the chosen material properties. The numerical torque magnitude as a function of twist pitch length for all three tapes is displayed in Figure 4.6. In the plots, the twist pitch refers to the length over which one complete rotation of the tape occurs. The smaller the twist pitch length, the higher the degree of twist in the tape.

The experimental torsion data from Section 3.1.2 was plotted as symbols alongside the FEA results in Figure 4.6. From the plots it is clear that the numerically calculated torque behavior matches the experimental torque trend which exhibits an exponential increase in torque magnitude for decreasing twist pitch lengths. The numerical results for the SuperPower and SuNAM tapes saw a slight deviation from the experimental curves below a twist pitch of 150 mm and 100 mm respectively for the two tapes. In contrast, the numerical AMSC results were seen to have the best agreement with the experimental data at twist pitch lengths less than 100 mm. Overall, the finite element results for the composite HTS tapes were found to accurately match the experimental torque behavior.

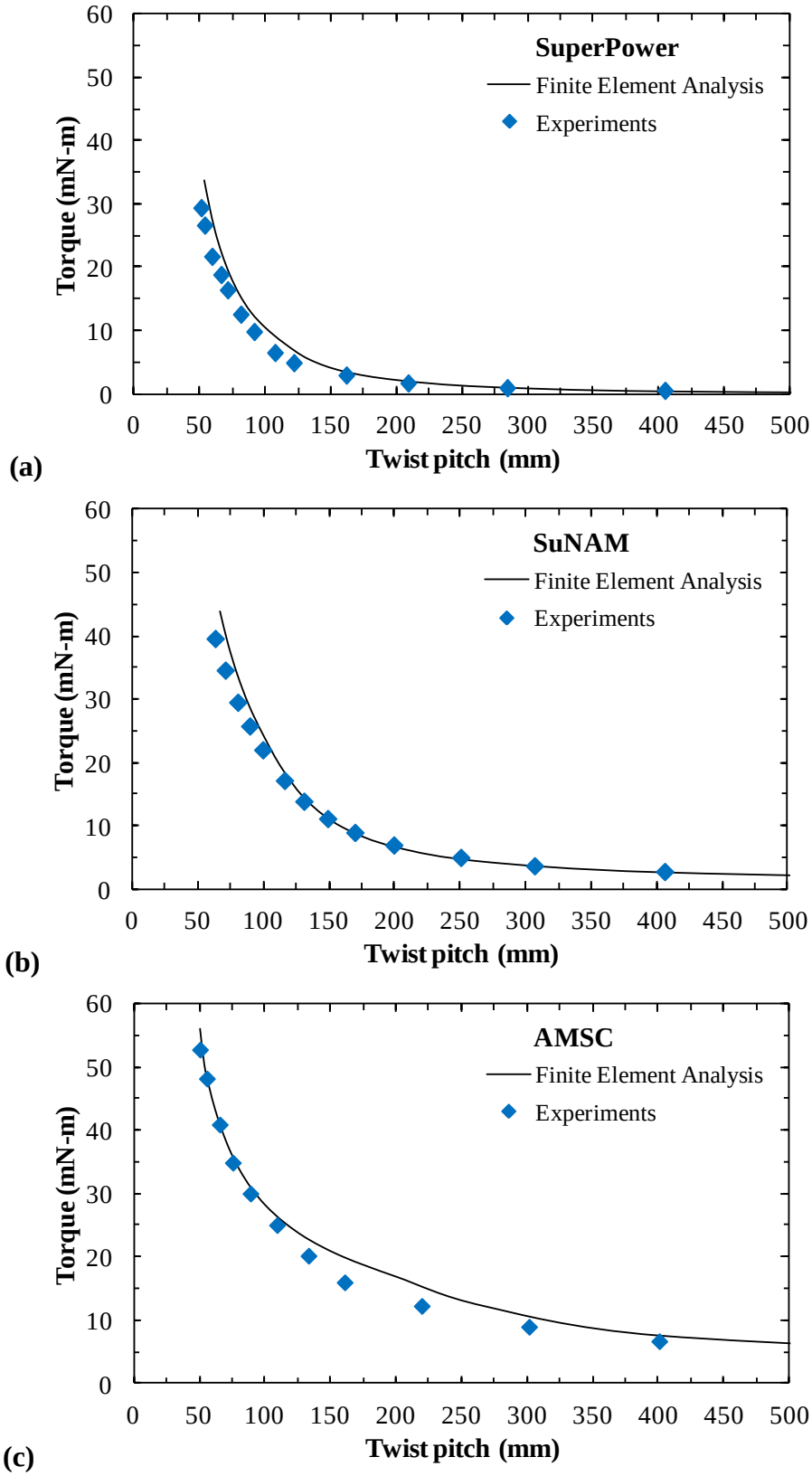

Figure 4.6 – Plot of torque as a function of twist pitch for SuperPower (a) SuNAM (b) and AMSC (c) tapes [44]. Experimental data plotted alongside finite element results.

The FEA model was also used to analyze the axial strain through the width of the tape. Figure 4.7 is a color contour plot of the axial strain in a typical twisted HTS tape showing negative compressive strain (blue) in the middle of the tape and positive tensile strain (red) on the outer edges. As illustrated in the figure, the strain was determined to be constant along the length of the tape which is consistent with a pure torsional load, validating the "symmetry style" end conditions used in the model.

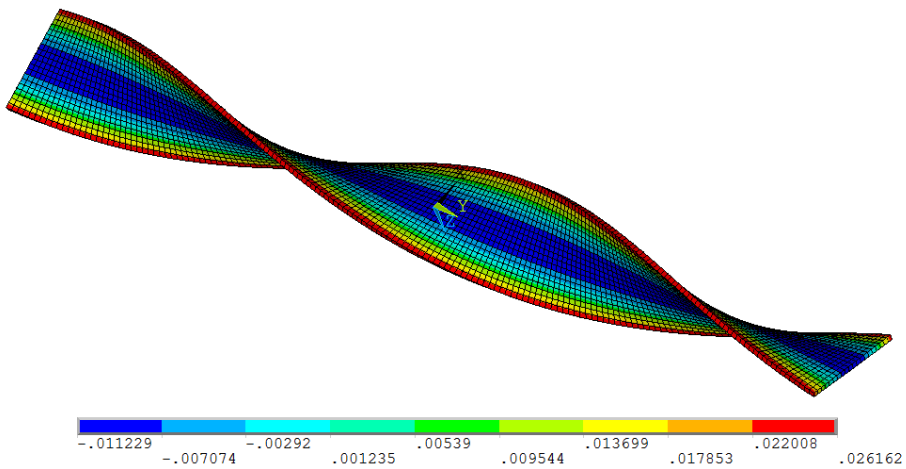

Figure 4.7 – Color contour plot of the axial strain profile in a twisted HTS tape determined from finite element analysis.

The strain results were taken from the center of the tape in the numerical model and matched the parabolic profile expected from a simple analytical calculation of a thin rectangular tape under torsion [64]. The strain data through the width of the tape was used to estimate the normalized critical current using the method described in Section 4.1.5.

The estimated critical current behavior as a function of twist pitch length calculated from the numerical strain results is presented in Figure 4.8. The experimental torsion data from Section 3.1.2 was plotted as symbols alongside the finite element analysis results.

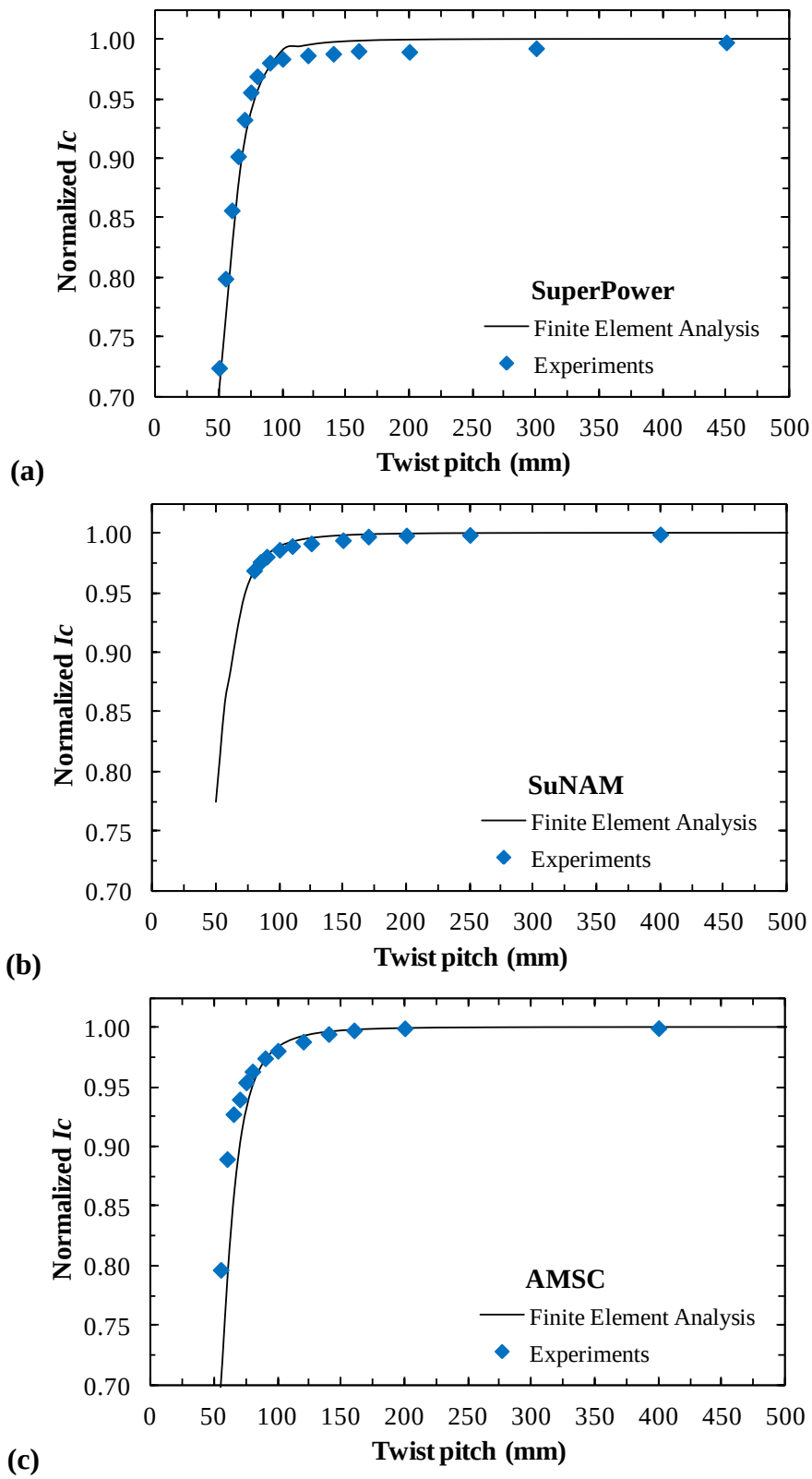

Figure 4.8 – Plot of normalized critical current as a function of twist pitch for SuperPower (a), SuNAM (b) and AMSC (c) tapes [44]. Experimental data plotted alongside the estimated critical current calculated from the numerical strain data.

The numerical critical current results follow the same degradation trend found experimentally. No critical current reduction was experienced down to a twist pitch of 120 mm. For shorter twist pitches a gradual decrease in critical current was seen followed by a sharp irreversible degradation below an 80 mm twist pitch. The SuNAM numerical results have the best agreement with the experimental data. The AMSC results from the finite element model predict a slightly earlier (longer twist pitch) degradation than was found experimentally. The numerical SuperPower results agree well with the experimental onset of degradation but have slightly lower critical current for longer twist pitch lengths.

Over the entire range of twist pitch lengths analyzed, the estimated critical current behavior of all three tapes is in good overall agreement with the experimental data, which validates the finite element model's ability to calculate the critical current of a tape based on numerical strain data. From the finite element model it can also be seen that under very short twist pitches (less than 80 mm) the tensile strain on the outer edges exceeds the yield strength of the tape. This plastic deformation in the tapes is likely the cause of the steep irreversible degradation in critical current that is experienced under torsion.

4.3 Axial Tension

The mechanical stress-strain behavior and critical current performance of single HTS tapes under axial tension were analyzed [44],[46]. Axial tensile strain is a leading cause of critical current degradation in HTS tapes and is generally unavoidable like in the case of different materials having different rates of thermal contraction leading to the development of axial stress upon cool down to the cryogenic operating temperature.

SuperPower, SuNAM and AMSC tapes were all investigated under axial tension using finite element analysis. The specifications, layered structure and dimensions of the three tapes are provided in Section 2.1. Numerical simulations were performed to identify the mechanical behavior of the composite HTS tapes including their stress-strain curve, yield strength and modulus of elasticity. The finite element model was also used to identify the strain state of the tapes under applied axial load so that the critical current performance could be predicted. No critical current results are shown for AMSC tape since experimental data was not available for comparison.

4.3.1 Model Details

The axial tension models were built with a tape length of 50 mm which is half of the 100 mm sample length tested experimentally. The shorter length of the model was similarly used to reduce the size and computational time of the simulations. The same “symmetry style” end conditions were used on the model to constrain the ends to remain planar while giving them the ability to move axially which is critical for tensile load simulations. Separate models were developed for the unique layered structures of each of the three tapes. Bilinear materials were defined in the model using the properties listed in Table 4.

The tensile load was applied as was done in the experiments; the bottom of the tape was held fixed while the load was applied to the top of the tape. The top of the tape was allowed to move freely so that the sample could elongate as tension was applied. A uniform tensile load was applied to the end area of the top tape using an outward facing surface pressure load. The tensile load was incrementally increased as done experimentally.

For every tensile load increment the displacement of the free end of the sample was recorded and used to build the stress-strain curve. The strain was calculated as the change in length divided by the original length and the stress was determined as applied load divided by the cross sectional area. The stress-strain curve was evaluated this way to match how it was calculated experimentally.

The axial strain through the width of the sample was also recorded at every step. The strain data was used to estimate the critical current performance of the tape as a function of applied tensile stress. The axial strain results were taken directly from the model in the middle of the tape eliminating end effects of the model. Both mechanical and estimated electrical results from the numerical model were compared with the experimental data provided in Section 3.2.2.

4.3.2 Results

The mechanical stress-strain behavior of the composite HTS tapes as determined from the finite element models were first evaluated against the experimental curves taken in Section 3.2.2. This was done to validate the numerical models ability to accurately simulate the true mechanical characteristics of the HTS tapes. The stress-strain curves for all three HTS tapes at 77 K are presented in Figure 4.9. In the plots the experimental curves are displayed as lines while the FEA results are plotted with open symbols.

As noted earlier, it is again evident that the stress-strain curves of all three tapes are notably different. The cause of these differences was investigated with the numerical model by varying the thickness and material properties of the layers in the tapes. As anticipated, it was found that the substrate and copper material

properties had the most influence on the behavior of the tape followed by their corresponding thicknesses.

In Figure 4.9, the finite element results have a slightly sharper plastic transition due to the bilinear material properties in the model but, overall are in good agreement with the experimental stress-strain curves for each tape. This is a clear indication that with the correct material properties defined for all layers of the HTS tape, the solid-shell model can accurately simulate the true mechanical behavior of the HTS tapes. The material properties used to produce the displayed FEA results are provided in Table 4.

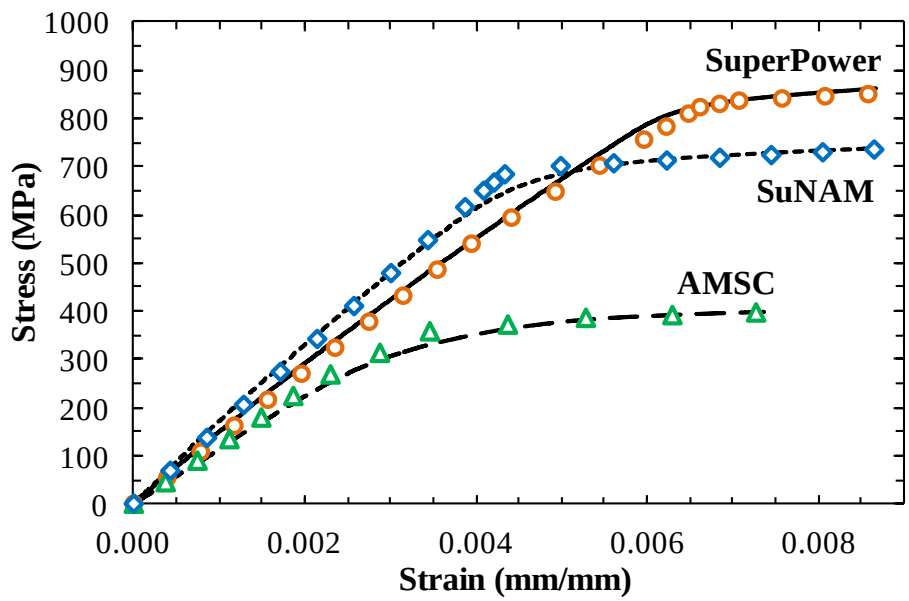

Figure 4.9 – Plot of stress-strain curves for SuperPower, SuNAM and AMSC tapes at 77 K [44]. Finite element analysis results (open symbols) plotted alongside averaged experimental data (solid curves).

In addition to the mechanical behavior of the tapes, the electrical critical current performance under axial tension was also analyzed numerically for SuperPower and SuNAM tapes; no experimental data was available for AMSC tapes. The FEA model was used to evaluate the axial strain through the width of

the tape which was then used to estimate the normalized critical current in the tape using the method described in Section 4.1.5.

The normalized critical current results as a function of applied axial tension for SuperPower and SuNAM tapes are shown in Figure 4.10. The critical current degradations predicted from the numerical strain data are plotted as solid lines. The finite element analysis results for both tapes exhibit a gradual reduction of critical current under increasing applied tensile stress followed by a sharp irreversible degradation. The onset of the sharp degradation aligns with the offset yield stress of the HTS tapes (the start of plastic deformation) shown by the stress-strain curves in Figure 4.9.

The averaged experimental data are displayed in Figure 4.10 as symbols for comparison. The horizontal error bars correspond to the best and worst performing samples that were presented in Section 3.2.2. The SuNAM experimental data was found to have fairly good agreement with the numerical results and experienced a sharp critical current degradation at a slightly lower tensile stress (~5%) than estimated by the finite element model.

In contrast, the experimental SuperPower critical current data was seen to degrade at a much lower tensile stress than predicted by the numerical results. However, as mentioned in Section 3.2.2, the SuperPower experimental data had a higher amount of variability between samples and overall had worse performance than anticipated from prior literature. Considering the experimental data is not fully understood, the manufacturer's data for SuperPower tape [23] is also displayed in Figure 4.10(a) for a more accurate comparison with the finite

element results. The manufacturer's critical current behavior was found to be much closer to the finite element results, as compared with the experimental data. The sharp degradation of critical current in the manufacturer's data occurred under a slightly lower tensile stress (~7.5%) than predicted numerically, similar to the SuNAM tape.

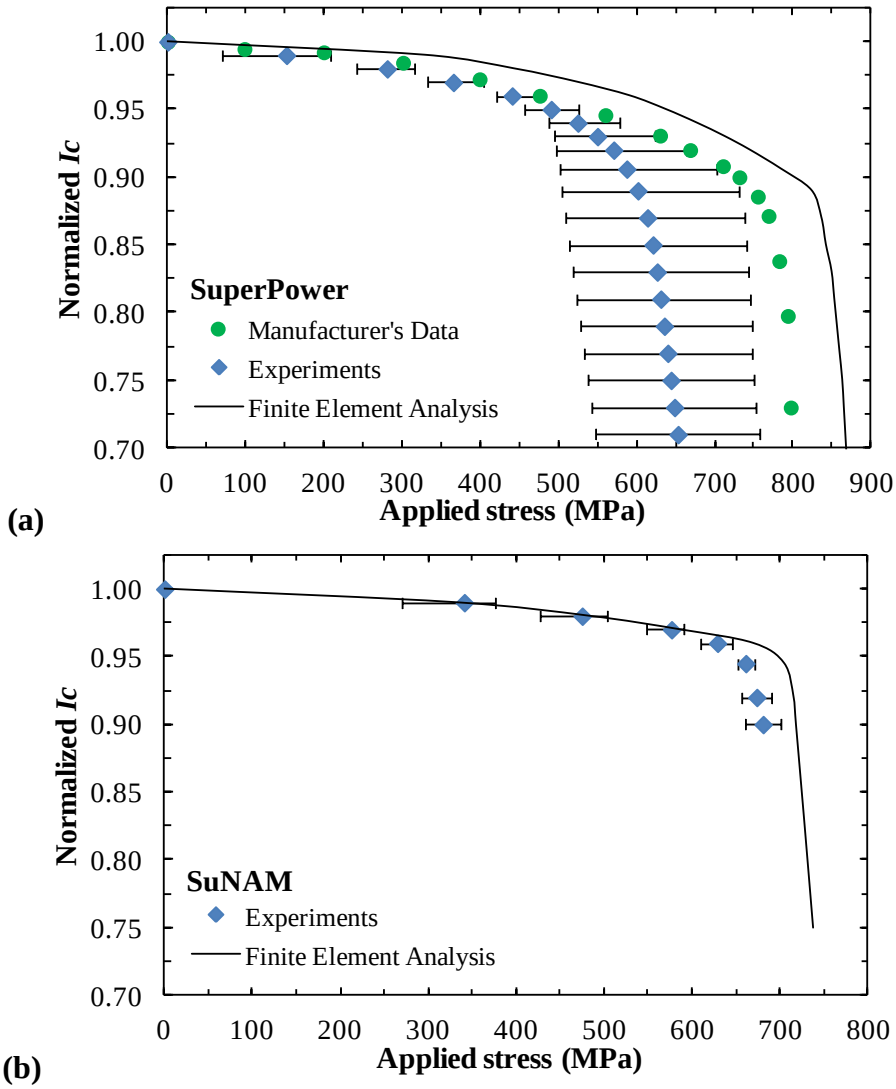

Figure 4.10 – Plots of normalized critical current as a function of applied tensile stress for SuperPower (a) and SuNAM (b) tapes [44]. Averaged experimental data plotted alongside the estimated critical current calculated from the numerical strain data.

An earlier experimental degradation of critical current under tensile stress was partially anticipated because the estimated critical current from the numerical

strain data is a best case scenario. The model assumes that the critical current will continue to degrade all the way up to a tensile strain of roughly 1.5% while it has been reported in literature that micro-cracks can develop in the superconducting layer of HTS tapes as early as 0.7% [65]. The model also uses bilinear material properties which may influence the onset of degradation. Considering this, it is not unreasonable that the numerical model slightly over predicts the critical current performance of the HTS tapes by roughly 5 to 10%.

4.4 Combined Torsion-Tension

The electromechanical behavior of HTS tapes under a combined tension-torsion load were investigated using structural finite element analysis [44],[46]-[47]. Tension-torsion refers to the combined loading condition of axial tension applied to twisted tapes. This type of combined load is of particular interest for TSTC conductors due to the twisted nature of the design and the unavoidable axial loads experienced in magnet applications.

The critical current sensitivity of two HTS tapes (SuperPower and SuNAM) were analyzed under combined tension-torsion loading with finite element analysis. The specifications, layered structure and dimensions of the tapes are provided in Section 2.1. The numerical simulations were used to identify the torque characteristics and axial strain as a function of applied tensile stress for tapes with different twist pitch lengths down to 90 mm. The numerical strain results were combined with an analytical model to predict the critical current performance of the tapes under load. The mechanical torque and estimated critical current results were compared with the experimental data presented in Section 3.3.2 for validation.

4.4.1 Model Details

Based on the relative success of the pure torsion and axial tension FEA models, the combined tension-torsion models also simulated a 50 mm long tape with “symmetry style” end conditions instead of the 300 mm long experimental tension-torsion samples. As done before, separate models were created for each analyzed tape: SuperPower, SuNAM and AMSC. The tapes were defined with the same material properties used in prior models which are listed in Table 4.

The rotation was applied to the sample using pilot node multipoint coupling constraints, as done for pure torsion models, and the tensile load was applied to the ends of the tape using an outward facing surface pressure load, as done in the axial tension models.

The combined tension-torsion load was applied in the numerical model in the same manner as done experimentally. The initially straight tape was first twisted to a specific twist pitch, by applying rotation to the top of the tape while fixing its bottom. A tensile load was then applied to the top of the twisted tape in an incremental fashion while the bottom remained fixed. Combined tension-torsion simulations were run for five twist pitch lengths: 200, 150, 115, 100 and 90 mm.

For every tensile load step, the change in torque and the axial strain through the width of the tape were recorded. The strain data was used to estimate the critical current performance of the tape as done in the prior models. The axial strain data was taken from the middle of the tape while the torque was measured as the reaction moment on the bottom. The numerical results were evaluated against the available experimental data shown in Section 3.3.2 for validation.

4.4.2 Results

The following results are from twisted HTS tapes under applied axial tension or combined tension-torsion loading. The influence of the twist pitch (amount of torsion) on the tensile behavior of the tapes was investigated. Five different twist pitch lengths were numerically analyzed (200, 150, 115, 100 and 90 mm) and compared with the two twist pitch lengths (200 and 150 mm) tested experimentally. The chosen lengths were based on the pure torsion results presented in Section 3.1.2, which found that torsion had no influence above a 200 mm twist pitch and had severe irreversible degradation below an 80 mm twist pitch. In addition to this, current TSTC conductors are made with a 200 mm twist pitch making it a desired twist pitch to analyze [18].

The combined tension-torsion torque characteristics from all three tapes as determined using finite element analysis are shown in Figure 4.11. In the figure, the change in torque magnitude from all five twist pitch lengths are plotted as a function of applied axial tension. All three HTS tapes exhibit an initial trend of linearly increasing torque with increasing applied tension. The SuperPower tape torque remains nearly linear, while the SuNAM tape plateaus under high axial stress and the AMSC tape peaks and then actually begins to decrease under additional load (no experimental data is available to validate this AMSC torque behavior). A comparison of all five twist pitch lengths from all three tapes reveals that tapes with a shorter twist pitch, higher degree of torsion, have a steeper increase in torque under the same applied axial load.

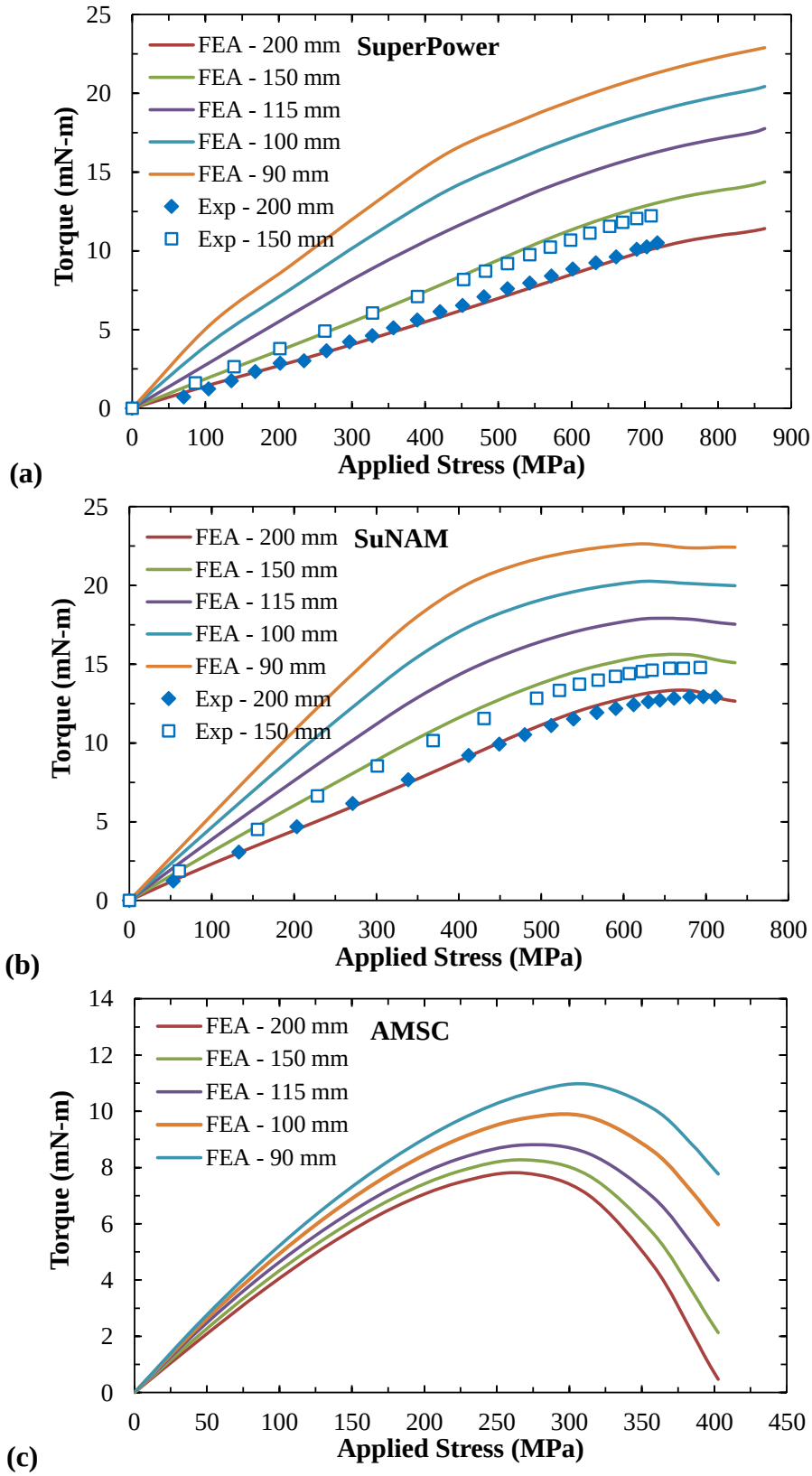

Figure 4.11 – Plots of the change in torque as a function of applied tensile stress on twisted samples from SuperPower (a), SuNAM (b) and AMSC (c) tapes [44].

The experimental combined tension-torsion results for SuperPower and SuNAM tapes with a 200 mm twist pitch (squares symbols) and a 150 mm twist pitch (diamond symbols) are plotted alongside the numerical results in Figure 4.11. The experimental torque data from both tapes shows a good overall agreement with the finite element results validating the model. Only a slight difference in torque behavior for the 150 mm twist pitch tapes under high axial tension (greater than 400 MPa) was evident.

In addition to the torque characteristics, the critical current behaviors of twisted HTS tapes under axial tension (combined tension-torsion loading) were analyzed. The critical current was again estimated from the finite element model using the axial strain results taken as a function of applied load, as described in Section 4.1.5. The normalized critical current results as a function of applied axial tension on twisted HTS tapes are shown in Figure 4.12. The numerical results for five different twist pitch lengths (200, 150, 115, 100 and 90 mm) were evaluated for all three HTS tapes: SuperPower, SuNAM and AMSC.

For all three tapes, the combined tension-torsion behavior for the various twist pitch lengths indicate that tapes with shorter twist pitch lengths (higher amounts of torsional load) experience an earlier and more gradual degradation of critical current as compared to the sharp degradation seen under axial tension. This earlier and more gradual critical current reduction is especially true for tapes with a 115 mm twist pitch or smaller, while the tapes with a 200 mm twist pitch were found to behave nearly identical to pure tension tapes. This result is consistent

with the pure torsion findings from Section 3.1.2 which determined an increasing effect of torsion on the critical current for twist pitch lengths below 120 mm.

Overall, for twist pitch lengths greater than 150 mm, the torsional strain in the twisted tapes has minimal influence on the critical current behavior under axial tension while for twist pitch lengths less than 115 mm the torsional strain contributes to an earlier and more gradual critical current degradation in the twisted tapes under tension.

To validate the capabilities of the finite element model, the average experimental combined tension-torsion data for SuperPower and SuNAM tapes with a 200 mm twist pitch (squares symbols) and a 150 mm twist pitch (diamond symbols) were plotted alongside the numerical critical current results in Figure 4.12. No experimental data for AMSC tapes was available for comparison. The error bars on the 200 mm twist pitch data again represent the best and worst performing samples. Only one sample was tested at a 150 mm twist pitch length.

The experimental critical current degradation of SuNAM tapes with a 200 and 150 mm twist pitch were almost identical and both saw good overall agreement with the estimated finite element results for the same twist pitch lengths. The experimental results saw a slightly earlier critical current degradation than predicted numerically, which is consistent with the axial tension results from Section 3.2.2 and is anticipated based on the method used to estimate the critical current of the tapes using axial strain data.

The experimental combined tension-torsion critical current results for SuperPower tapes were seen to degrade at a much lower tensile stress than

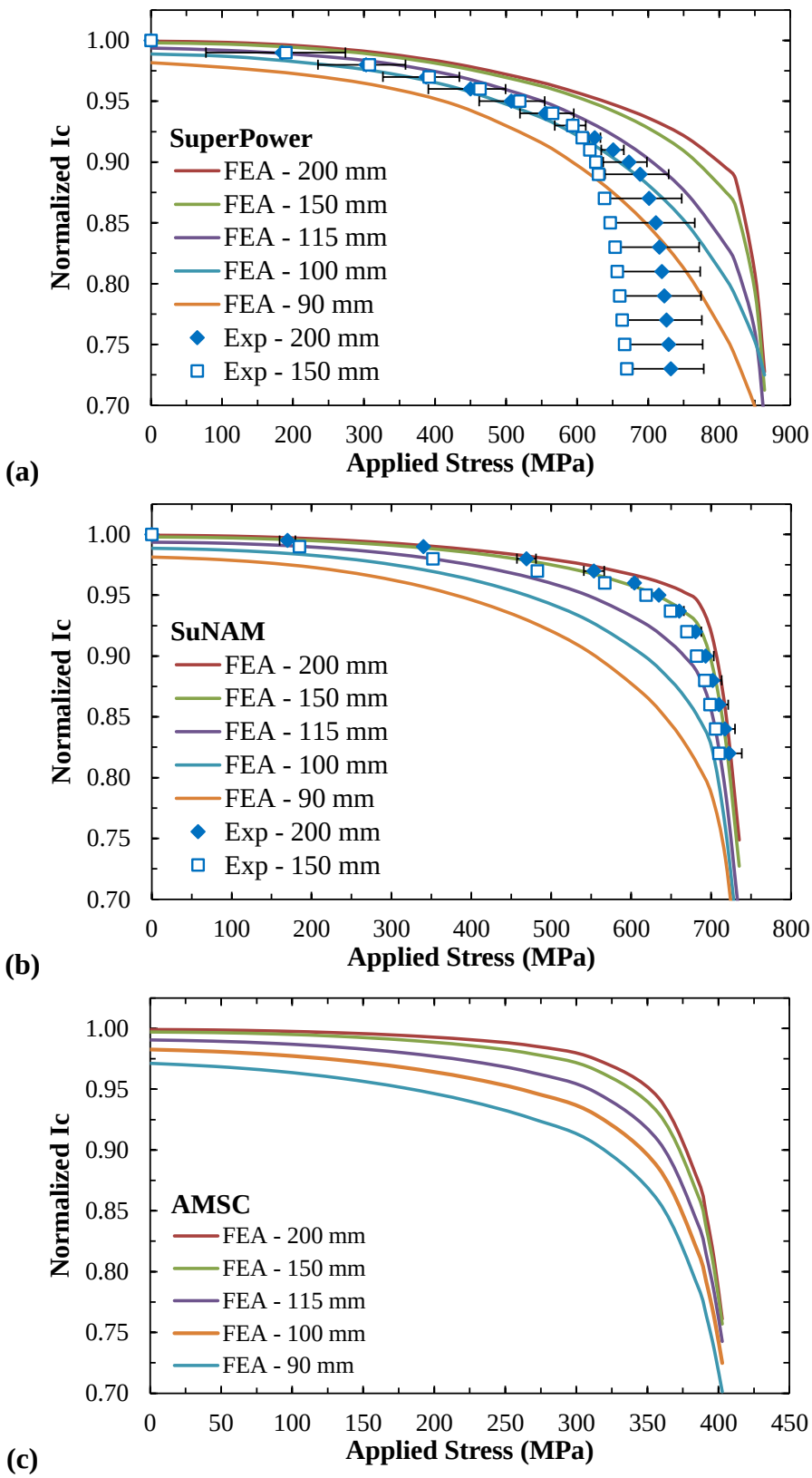

Figure 4.12 – Plots of normalized critical current (I_c) as a function of applied tensile stress on twisted samples from SuperPower (a), SuNAM (b) and AMSC (c) tapes [44].

predicted by the numerical results. This was expected based on the early degradation of axial tension samples found in Section 3.2.2. The difference with the finite element results does not necessarily reflect the inaccuracy of the model but rather the uncertainty of the experimental data.

The good agreement of the experimental torque trend for SuperPower and SuNAM tapes and the experimental critical current behavior of SuNAM tapes with the finite element results validate the numerical models ability to analyze the electromechanical characteristics of HTS tapes under combined tension-torsion.

4.5 Summary and Future Work

Structural finite element analysis was conducted to investigate the electromechanical characteristics of three commercial HTS tapes from SuperPower, SuNAM and AMSC. For comparison and validation, the tapes were analyzed under the same loading conditions applied experimentally including pure torsion, axial tension and combined tension-torsion.

A novel technique was developed for modeling the layered composite structure of the HTS tapes using structural solid-shell elements in ANSYS®. The finite element models were used to simulate the true mechanical characteristics of the tapes. Under axial tension the model accurately reproduced the stress-strain curve of each tape while under pure torsion and tension-torsion the model was able to capture the torque behavior as a function of increasing load.

The numerical model was also used to record the axial strain in the superconducting layer of the HTS tapes under all three load types. The axial strain data through the width of the tape was successfully coupled with an analytical

model to estimate the critical current performance of the HTS tape. The numerically predicted critical current behavior for pure torsion, axial tension and combined tension-torsion loads were found to be in close agreement with the experimental data, with the exception of SuperPower tension and tension-torsion experimental data.

The overall good agreement seen between the experimental measurements and the finite element analysis validated the numerical model's capability to capture the electromechanical characteristics of HTS tapes. Together the numerical and experimental data can provide unique insight into the strain dependence of the critical current for these HTS tapes.

Future single tape finite element modeling work should be focused on improving the fit of the estimated critical current behavior to the experimental results. Currently the numerical models are optimized to replicate the mechanical characteristics of the tapes and not the electrical behavior. This work consider the influence of micro-cracks in the superconducting film by reducing the range of numerical strain (currently ±1.5%) used to estimate the critical current of the tapes. Another method for improving the estimated critical current trend would be to investigate different material property definitions including multilinear curves and bilinear curves defined with an initial yield value instead of the offset yield currently being used.

5.0 HTS Cable Experiments

In addition to the electromechanical characterization of single tapes, two HTS tape cabling methods, designed for high field magnet applications, were investigated experimentally. The HTS slotted-core CICC from ENEA was tested under bending and the twisted stacked-tape cable from MIT was analyzed under transverse compression. Custom experimental test equipment for both load types were used to evaluate the critical current as a function of applied mechanical load. Critical current measurements were conducted on individual tapes within each cable. For both experiments the critical current was measured under 77 K, self-field conditions. The details and results from the HTS cable experiments are described in this chapter.

5.1 Bending

Electromechanical experiments on the bendability of the HTS slotted-core CICC from ENEA have been carried out [49]. These tests were done to characterize the smallest bending radius achievable without electrical performance degradation. Knowing the bending behavior of the cable is fundamental to its future implementation in high field magnet coils for fusion applications. The influence of the twist pitch on the bending performance of the cable was also investigated.

The bending tests were conducted using a custom bending tool which used a series of circular wooden disks with decreasing diameters. The HTS CICC samples were bent around the wooden disks and then fixed in place for the critical current measurements. Two 1.0 m long HTS CICC cables were tested; one with a

long twist pitch (LTP) of 1.4 m and the other with a short twist pitch (STP) of 0.5 m. Both cables contained four active SuNAM tapes per slot for a total of twenty tapes in the cable. The specifications and properties of the tested SuNAM tapes are listed in Table 2 of Section 2.1. A controlled bending moment was applied to the HTS CICC samples at room temperature. Each HTS tape was then electrically characterized by measuring its critical current performance at each subsequent bending diameter down to 0.25 m.

5.1.1 Experimental Setup

A controlled bending moment has been applied to the samples at room temperature by means of a custom bending tool. The device bends the sample around circular wooden disks with decreasing diameters. The cable is bent around the disks using a lever arm mechanism with an attached wheel. Supports are placed along the cable to keep it fixed to the disk during testing, ensuring uniform bending along the sample. The bending diameter was reduced in steps from 1.6 m down to 0.25 m. A photo of the cable bent to a 0.4 m diameter is shown in Figure 5.1. The device is capable of bending roughly 0.85 m of the 1.0 m long cable due to the interference with the current leads.

Two 1.0 m long HTS CICC cables were tested under bending. One cable had a long twist pitch (LTP) of 1.4 m while the other cable had a short twist pitch (STP) of only 0.5 m. For both cables, each slot was filled with nineteen tapes; four SuNAM tapes and fifteen stainless steel dummy tapes. From the bottom of the stack up, the active tapes were located in the 3rd, 8th, 13th and 18th positions as shown in Figure 2.4(b). Each cable contained a total of twenty SuNAM tapes.

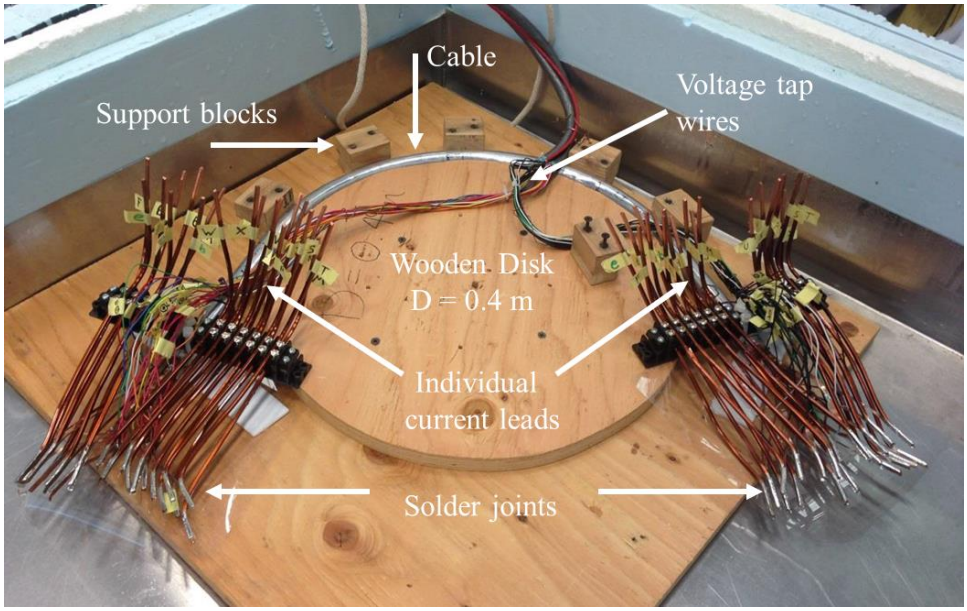

Figure 5.1 – Image of the HTS slotted-core CICC bent on 0.4 m diameter wooden fixture showing individual current leads for each active tape [49].

Since the short twist pitch sample has a twist pitch length shorter than the cable, the strain distribution in every slot should be equivalent. On the other hand, the twist pitch of the long twist pitch sample is greater than the cable length and consequently the strain in each slot is not equivalent.

For both cables, the critical current of each HTS tape was measured individually. The current was supplied by a 220 A power supply and was fed through copper current leads soldered directly to each tape as shown in Figure 5.1. Voltage taps were soldered as close to the ends of the jacketed cable as possible covering a length of approximately 1.05 m. For each applied bending diameter, the critical current was measured at 77 K, in self-field conditions. All critical current results were evaluated at an electric field criterion of 100 μV/m.

5.1.2 Results

The critical current results for both HTS CICC cables as a function of applied bending diameter are shown in Figure 5.2. In the plots, the critical current of all

eleven measurable tapes are shown; a few tapes from both cables were initially degraded and could not be characterized under bending. Overall, both cables experienced a negligible reduction in critical current down to a bending diameter of 0.5 m followed by a steep degradation. A much larger variability in the critical current performance between tapes was also experienced below 0.5 m bending diameter as the cable started to degrade. The average, minimum and maximum critical current performance of the eleven tested tapes from both cables are described below.

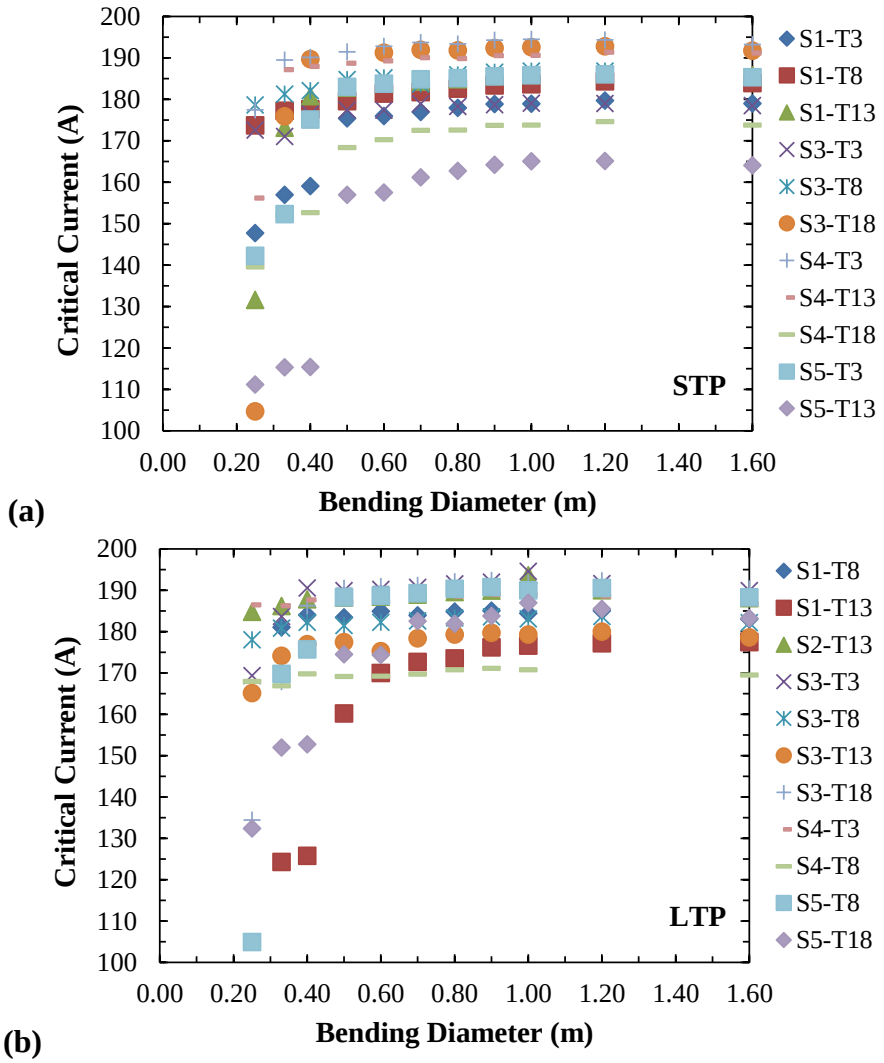

Figure 5.2 – Plots of critical current as a function of bending diameter for two HTS CICC cables [49]. (a) Short twist pitch and (b) long twist pitch. Legend: Slot # - Tape #.

The short twist pitch cable at 0.5 m bending diameter experienced an average critical current reduction of 2%. The best and worst tapes experienced a critical current reduction of 1% and 4% respectively. The average critical current reduction at a bending diameter of 0.33 m was 10% with a max degradation of 30% and a minimum of 3%. At the minimum measured bending diameter of 0.25 m, the average critical current degradation of the short twist pitch cable was 19% with the worst performing tape degrading by 45% and the best performing tape only degrading by 4%.

The long twist pitch cable underwent similar behavior and also had an average critical current reduction of 2% at 0.5 m bending diameter. Its best tape had no critical current reduction and its worst performing tape degraded by 11%. At a 0.33 m bending diameter, an average critical current reduction of 8% was seen with a max degradation of 31% and a minimum of 1%. The average critical current degradation of the long twist pitch cable at the minimum measured bending diameter of 0.25 m was 15% with one tape degrading by as much as 44% and another tape only experiencing a 1% reduction.

It was originally expected that the outer tapes would experience higher tensile and compressive bending strain and therefore might experience more critical current degradation compared to the inner most tapes. As seen in Figure 5.2, this is not the case and the bending strain at which a first degradation occurs, does not depend on the position of the tapes within the stacks. Additionally, several tapes in both samples degraded less than anticipated, even at the smallest bending diameter of 0.25 m. The likely explanation of this behavior is that the tapes in

each stack can slide relative to each reducing the strain of each tape. In addition to this, the slots in the core are slightly oversized compared to the tape stack which may give the stacks enough freedom to move and tilt, locally reducing the bending strain and improving the critical current behavior.

5.2 Transverse Compression

Mechanical transverse load tests were conducted on two types of TSTC conductors [48]. These tests were done to investigate each cables deformation behavior and critical current sensitivity under transverse compression. Transverse compression is a typical load generated from the natural electromagnetic Lorentz forces experienced in a high current cable operating in high magnetic fields. Since high current high field cable tests are challenging and costly, a representative electromagnetic load was applied mechanically. The effects of localized and uniform transverse compression were also studied, given the twisted geometry of a TSTC conductor.

The device used for transverse compression on single HTS tapes, as described in Section 3.4.1, was also used for cables by modifying the pressing plates and load fixtures. A 24-tape soldered TSTC conductor and a 40-tape TSTC conductor inside a copper tube filled with solder were tested. Both cables were made with the SuperPower HTS tapes as listed in Table 2 of Section 2.1. A uniform transverse compressive load was first applied to the 24-tape cable followed by a two-point concentrated load. Two regions of the 40-tape copper tube cable were also tested under uniform transverse compression.

5.2.1 Experimental Setup

The device used for transverse compression of TSTC conductors was the same as the one used for transverse compression of single tapes and is shown in Figure 3.10. The transverse load is applied by manually rotating the forcing screw of a bolt-grip push-puller, which forces a central rod downward applying compressive load to the sample. The applied downward load is measured with a load cell and is transferred to the cable using specialized load fixtures.

Transverse loads were applied to a bare 24-tape soldered TSTC conductor and to a copper sheathed 40-tape TSTC conductor filled with solder. Custom pressing plates for a uniform distributed load and a two-point concentrated load were used and are schematically shown in Figure 5.3. To apply a uniformly distributed transverse load (a), two parallel pressing plates were used. The top plate had shallow rounded edges to alleviate any stress concentrations and a pressed length of 125 mm. To apply a two-point concentrated load on the 24- tape bare TSTC (b), a horseshoe shaped load fixture was used. The load fixture evenly concentrated the downward load at two points spaced 70 mm apart. Each pressing point had an approximate pressing length of 5 mm during testing. A flat plate was used underneath the cables in both load types for consistency.

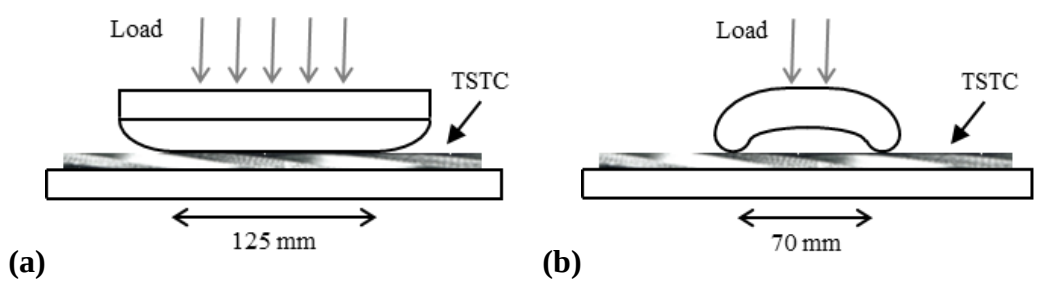

Figure 5.3 – Schematic of transverse compression load fixtures for TSTC conductors. (a) Uniform distributed pressing plate and (b) concentrated two-point pressing fixture [48].

For the 24-tape cable with four active HTS tapes, the critical current of each tape was measured individually. The current was supplied by a 220 A power supply and was fed to each tape using separate copper current leads. Voltage taps were soldered to each tested tape at the ends of the cable, spanning roughly 470 mm.

For the 40-tape sheathed cable under uniform load, the critical current behavior of the entire cable was characterized. The current was provided by three 1.2 kA power supplies connected in series. The current was fed through copper terminal blocks to removable BSCCO-YBCO joints, described in [64], which connected to the ends of the cable supplying current uniformly to all forty tapes. Voltage taps with a 200 mm separation were attached to the exterior of the copper tube centered about the location of applied load.

The voltage taps were used to record the critical current transition of the tapes/cable under incrementally applied transverse load. All critical current results were evaluated at an electric field criterion of 100 μV/m. The mechanical load and electrical measurements were both performed at 77 K and self-field conditions.

5.2.2 Results

A 24-tape soldered TSTC conductor and a 40-tape TSTC conductor soldered inside a copper tube were tested under mechanically applied transverse compressive loads, representative of natural electromagnetic loads experienced by TSTC conductors in high magnetic fields.

The sensitivity of critical current of the 24-tape cable under both a uniform transverse load and a more localized two-point load were investigated. The 24-

tape twisted stacked-tape cable had twenty dummy tapes and only four active HTS tapes of which only one was not damaged during prior experiments [66]. The cable was 432 mm long and had a cable twist pitch of 200 mm. The 24-tape stack was sandwiched between two copper strips and fully soldered together.

The critical current results as a function of average applied compressive stress for the 24-tape cable are displayed in Figure 5.4. The average applied transverse stress was calculated as applied load divided by the average pressed area which was determined as the diameter of the cable multiplied by the pressed length. Consequently, the average transverse stress plotted is a conservative value with local loads likely being higher due to the twisted geometry of the cable.

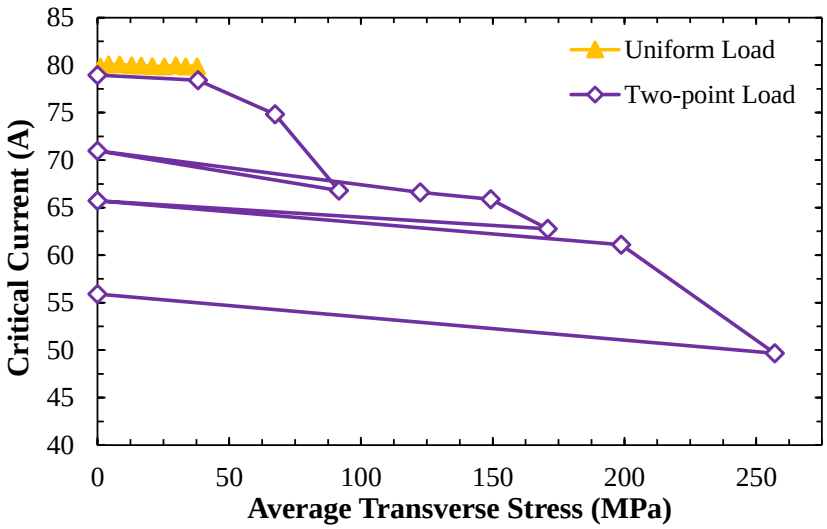

Figure 5.4 – Plot of critical current as a function of average transverse compressive stress for a 24-tape soldered TSTC conductor [48].

In Figure 5.4, no critical current degradation was evident up to 40 MPa of uniformly applied transverse stress over a 125 mm long section of cable. This was the maximum load applied due to the safe operating range of our experimental device. Inspection of the cable after testing found that over the uniformly pressed section, the cable flattened in such a way that the tapes were being loaded mostly

along their wide face. From the single tape results in Section 3.4.2, the critical current of HTS tapes was more resilient to transverse load on their wide face.

Under a concentrated two-point transverse load (with a span of 70 mm), the critical current degradation of the 24-tape cable was far more evident and began under an average applied transverse stress around 70 MPa. By an applied stress of 90 MPa, the critical current had degraded irreversibly by 15% from its initial value. It should be noted that this stress also corresponds to a much smaller transverse force than under uniform loading since the pressed area is far more concentrated. Inspection of the cable after testing observed that the twisted tapes of the cable experienced localized “over-twisting” and shearing which likely attributed to the more pronounced degradation of critical current that was experienced.

The critical current behavior of the 40-tape sheathed twisted stacked-tape cable under uniform transverse load was studied. Two different sections of the cable were uniformly loaded; the center section and the end section near the positive current terminal. The cable consisted of a stack of 40 SuperPower tapes twisted with a twist pitch of 200 mm. The tape stack was placed inside a 9.5 mm diameter copper tube which was filled with solder. The sheathed cable had an overall length of 640 mm. The center section of 40-tape cable was previously tested in high magnetic fields [67] and experienced permanent degradation. These tests were aimed at better understanding this degradation which was likely caused by insufficient mechanical support of the cable under large electromagnetic loads. The end section was in a low magnetic field zone and was not degraded during the high field tests.

The critical current results of the 40-tape cable as a function of average applied compressive stress are displayed in Figure 5.5. The external diameter of the copper tube was used in the calculation of the pressed area, which results in relatively conservative (low) applied stress. The initial critical current values under no load indicate the center section of the cable was permanently degraded by 15% compared to the end section which showed the expected critical current at 77 K and self-field conditions.

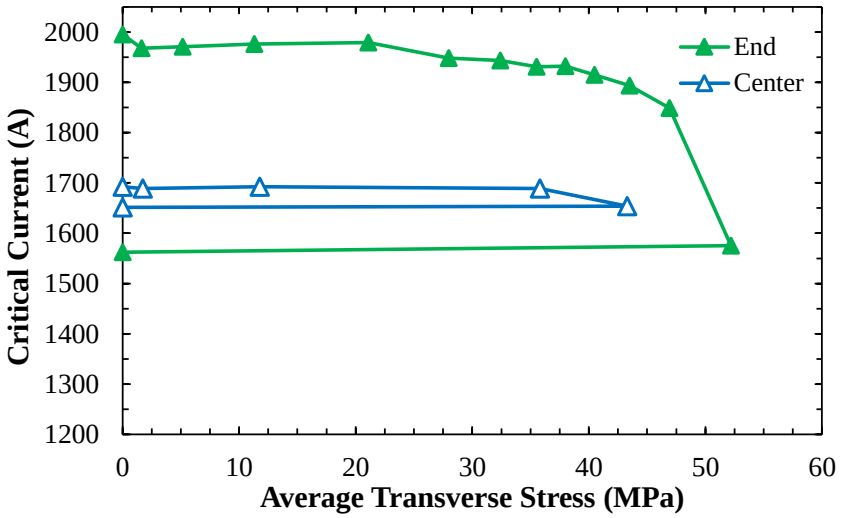

Figure 5.5 – Plot of critical current as a function of average transverse compressive stress for a 40-tape TSTC conductor soldered inside a copper tube [48].

The end section under uniform transverse compression saw a gradual and reversible reduction in critical current beginning at 28 MPa of applied transverse stress. At 45 MPa of stress the critical current was reduced by only 6% of the no load value. Following this, a sharp degradation of the critical current was experienced which led to an irreversible degradation of 21% at 52 MPa of applied transverse load.

The center section of the cable was already degraded roughly 15% before uniform transverse compression was applied. Because of this, the cable saw no

additional degradation under transverse load until a stress of nearly 45 MPa was reached. The undamaged end section saw an earlier more gradual reduction of critical current but similarly experienced irreversible degradation above 45 MPa of applied stress.

5.3 Summary and Future Work

The electromechanical performance of two HTS tape cabling methods, designed for high field magnet applications, were evaluated experimentally. The HTS slotted-core CICC was tested under bending and the twisted stacked-tape cable was analyzed under transverse compression.

The electromechanical bending behavior of two HTS slotted-core CICC cables were evaluated down to a bending diameter of 0.25 m. Minimal critical current reduction was experienced down to 0.5 m bending diameter which was followed by a sharp irreversible degradation. At a 0.5 m diameter, the average critical current degradation of both cables was 2% and the worst performing tape in the short twist pitch sample was only degraded by 4%. At the minimum bending diameter tested (0.25 m) the average critical current degradation of the two cables was 19% and 15% for the short and long twist pitch cables respectively. At this bending diameter, both cables had tapes degraded by nearly half of their initial straight values.

Overall, it can be concluded that to avoid critical current degradation of the cable, the bending diameter used for magnet coils needs to be 0.5 m or larger, to ensure bending strains remain below an acceptable level. Future work for bending tests should include testing longer samples to identify if they perform in the same

manner as the short cable tests conducted in this work. Additional bending tests could also include bending of different TSTC configurations likely to be used in high field magnet applications.

External mechanical transverse compressive loads equivalent to the natural electromagnetic loads experienced during high field operation were applied to TSTC conductors. The unique twisted geometry of a TSTC was taken into account by investigating the effects of localized and uniform transverse compression. A more pronounced critical current degradation was found under a two-point concentrated load compared to a uniform load, likely caused by a local "over-twisting" phenomena in the cable. The 40-tape sheathed TSTC experienced a gradual critical current reduction up to an applied transverse stress of 45 MPa followed by a steep irreversible degradation upon further loading.

Overall, the TSTC performance was better than anticipated, less critical current degradation under higher loads, based on real degradations experienced in high field TSTC tests. The mechanically applied transverse loads were therefore unable to fully explain the actual degradation caused by internal electromagnetic Lorentz loads but highlighted some possible degradation mechanisms. That said, future work for transverse compression on TSTC conductors should be aimed at testing more cables under actual transverse electromagnetic Lorentz loads generated in high field operation.

6.0 HTS Cable Modeling

Full scale three-dimensional finite element simulations of the twisted stacked-tape cable from MIT and the HTS slotted-core CICC from ENEA were conducted under the same loads characterized experimentally, bending and electromagnetic transverse compression. A unique methodology for modeling full scale HTS cables was developed which incorporated parameterized geometry, for easy modification and optimization of the cable design, and modifiable contact pair relationships, to define the relative motion between neighboring geometries. The HTS tapes within the cables were modeled with the same solid-shell technique used for single tape simulations.

Under bending [44],[49], the finite element modeling will be used to identify the axial strain in each HTS tape to estimate the critical current behavior of the entire cable. Under electromagnetic transverse compression [50], the numerical models will be used to identify the maximum compressive stress in the tape stack to gauge the performance of the cable under transverse load. Details of the finite element cable models and their corresponding results are described in this chapter.

6.1 Finite Element Analysis

Commercial finite element analysis software from ANSYS® was again used to conduct numerical simulations of HTS cables. Full scale three-dimensional models of the twisted stacked-tape cable and the HTS slotted-core CICC cable were developed utilizing the same solid-shell technique for modeling the layer architecture of the HTS tapes as was done in single tape models. The TSTC models were built with material parameters based on SuperPower tapes while the

HTS CICC models were built with SuNAM tapes. The specifications of the cables and the HTS tapes can be found in Section 2.0.

The final twisted cable geometry of the TSTC and the HTS CICC conductors were built within ANSYS® and were modeled with an initially strain free condition. This method of modeling ignores the initial stress and strain state caused by the cable fabrication processes (twisting, soldering, jacketing, etc.). This method was justified, since the relative strain state within the cables after fabrication is small when compared to the applied transverse compressive and bending loads being analyzed.

The numerical cable models were analyzed under two critical loads for HTS cables, bending and transverse compression. The applied bending load in the finite element model was representative of the loads tested experimentally. The transverse compressive load was representative of a true electromagnetic Lorentz load experienced in a TSTC cable which is different from the mechanical loads applied externally during experiments.

The numerical cable simulations were also run as static non-linear analyses with large deformation and enhanced strain formulations. The simulations were calculated using numerical integration techniques and automatic time stepping to increase convergence speed.

The stress and strain state of the HTS tapes within the cables were analyzed as a function of applied load. The effect of friction on the relative strain level in the HTS tapes was also analyzed. For bending loads the electrical performance of the tapes and cables was estimated from the structural model using the axial strain.

The numerical results from the finite element simulations were evaluated against the experimental data presented in Section 5.0.

6.1.1 Element Types

The layered structure of HTS tapes in the cable simulations was again modeled using SOLSH190 structural solid-shell elements as described in Section 4.1.1. The tapes were meshed with one element through their thickness and their layered structure (number, thickness, material properties, etc.) was defined within the finite elements. This method was utilized based on its ability to capture the true electromechanical behavior of HTS tapes under applied load, as validated using experimental data in Section 4.0.

The layered architecture the HTS tapes were also at times simply modeled as a single uniform tape with material properties equivalent to those of the composite tape determined experimentally in Section 3.2.2 and summarized in Table 3. This simplification was used to reduce the size, complexity and especially the computational time of the full scale cable models. In this case, SOLSH190 elements were still used to model the tape, but only one layer (uniform volume) was defined for the tape.

Along with the HTS tapes, both cable designs have some form of additional support structure; the HTS CICC has a slotted-core, spacers and external jacket while the TSTC conductors have either a copper core or a solder filled tube. These additional physical geometries that comprise the HTS cables were discretized in ANSYS® using SOLID185 homogeneous structural solid elements. These are eight-node hexahedron “brick” continuum elements with linear elastic

and full nonlinear capabilities including plasticity, stress stiffening, and large deflection/strain. Linear eight-node brick elements with sufficient mesh density were chosen instead of higher order twenty-node hexahedron elements.

Hexahedron “brick” elements are the most tolerant element geometry to high aspect ratios (the ratio of element length to width and thickness) making them ideal for modeling long slender structures like the HTS cables. Brick elements can also be used with mapped or structured meshing which allows a uniform controllable patterned mesh to be used along the length of the cable.

6.1.2 Finite element mesh

The HTS tapes (SOLSH190) and additional cable structures (SOLID185) were both meshed with brick type finite elements. Brick elements were used so that the long slender nature of the cables could be meshed with elongated elements having a length-to-width aspect ratio of two. This technique reduced the total number of elements along the cable length which greatly lessened the heavy computational time required to solve the simulation without impacting the accuracy of the model.

The layered structure of the HTS tapes was again modeled with solid-shell elements which required the tape geometry to be meshed with only one element through its thickness. The remaining mesh density of the tapes was reduced from the mesh used in single tape models to help lessen the computational burden of full scale cable models. The exact number of elements used through the width of the tape varied with cable model but was around ten elements as compared to twenty or greater used for single tape simulations. The number of elements along

the length of the tapes depended on the length of the cable and the mesh density through the width considering an aspect ratio of two was selected.

The mesh density in the remaining cable structures was highly dependent on the cable type, cable length and load being analyzed in the model. Overall, the cable support structures were typically discretized with a courser mesh than used for the HTS tape stack. The discretized geometries of two cables are displayed in Figure 6.1; the HTS CICC and the TSTC soldered in a copper tube. For the most part the mesh density used was fairly consistent between cable models.

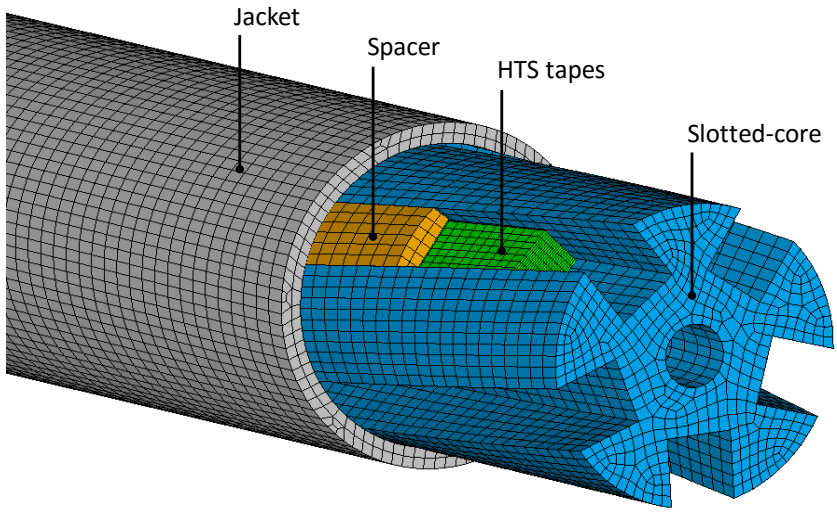

(a)

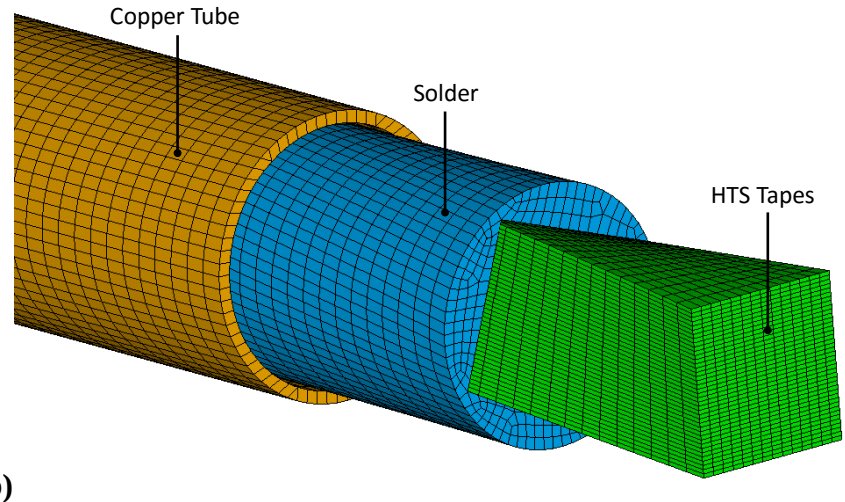

(b)

Figure 6.1 – Images of the discretized cable geometries of the (a) HTS slotted-core CICC [44] and (b) the TSTC soldered inside a copper tube [50].

6.1.3 Material Properties

Similar to single tape models, bilinear isotropic material properties were again used to capture the nonlinear elastic-plastic deformations that are likely to occur in the cables under large load. The bilinear material curves were again characterized in ANSYS® with a modulus of elasticity (E), offset yield stress (Y) and tangent modulus (T). All material properties used in the cable models were defined for a 77 K liquid nitrogen environment.

The HTS tapes in the cables models which incorporated their layered structure used the same material properties that were used in single tape models and are listed in Table 4 of Section 4.1.3. These material properties were validated to accurately model the true electromechanical properties of the HTS tapes. For the HTS tapes in the simplified homogeneous tape models, the experimentally determined bilinear material properties of the entire composite tape listed in Table 3 of Section 3.2.2 were used. For both models the overall mechanical characteristics of the HTS tapes should be equivalent.

The HTS CICC cable model has a twisted and slotted extruded aluminum core along with copper spacers and a cylindrical jacket made from aluminum sheet. One configuration of the TSTC conductor was modeled with a machined cylindrical copper rod while another configuration was modeled with the tape stack being placed inside a solder filled tube which can be defined as copper or stainless steel.

Isotropic bilinear material properties for the additional cable support materials (aluminum, copper, stainless steel and solder) at 77 K are provided in Table 5. The material properties were gathered from published literature and

manufacturer's data when available. The range or spread of values for each material comes from the composition, fabrication and heat treatment of the material. For instance, extruded aluminum is different than bulk aluminum, annealed copper is much weaker than work hardened copper and solder varies greatly with its tin-lead composition.

Table 5 – Bilinear material properties of HTS cable support materials at 77 K.

Cable	Material	E (GPa)	Y (MPa)	T (GPa)	References
HTS CICC	Aluminum	80	235	15.0	[56], [68]-[69]
TSTC	Copper	120	400	4.5	[56]-[57],[68]
	Stainless Steel	180	950	10.0	[52]-[53]
	Solder *(Sn60/Pb40)*	30	100	1.0	[70]-[72]

6.1.4 Contact Relationships

One of the most influential aspects governing the behavior of HTS cables is their mechanical contact interactions. Many different contacts exist within a cable and their behavior depends primarily on the type of load being analyzed. Bending loads are most interested in frictional sliding contact along the length of the cable while in comparison transverse compression loads are more concerned with penetration and the transmittal of load through the contact.

One of the most important contact interactions within a cable occurs between neighboring HTS tapes. The relative motion of these adjacent tapes has a major influence on the mechanical and electrical performance of the cable. Another major contact interaction within a cable is that of the tape stack and remaining cable structure. Along with this, the use of solder or epoxy in the cable will also significantly impact the contact behavior which will impact in the overall behavior and performance of the cable.

Accurately modeling these interactions is essential to developing realistic cable simulations. These cable and tape interactions were modeled using surface-to-surface contact pairs which are defined as having a target and a contact surface which share a set of specified characteristics or settings. Different settings can be chosen for each contact pair to vary the behavior of the interaction. The target and contact surfaces are generated on top of the existing solid geometries and are solely used to model the interaction of the solid volumes. The contact surfaces take on the same characteristics and element topology as the underlying geometry.

In ANSYS®, the contact pairs were defined using TARGE170 target elements and CONTA174 surface-to-surface contact elements. These are the typical contact elements used to simulate an interaction between three-dimensional geometries. For the cable models multiple two main contact sets, each having their own characteristics and settings, were defined. One contact set included all contact pairs defined between every neighboring tape in the stack. The other contact set included the contact pairs defined between the outside of the tape stack and the core/support structure. Additional contacts were also needed in some models.

The contact sets were used to investigate the influence of friction on the relative motion of the tapes and to identify how that influences the critical current behavior of the cable. The contacts were analyzed for a bonded (no-slip) condition, a frictionless (perfect-slip) condition and for a range of friction coefficients from 0.02 to 1.0.

6.1.5 Boundary Conditions and Loads

Bending and transverse compression was applied to the cable models in the most effective manner numerically and therefore are note representative of how

the loads were applied experimentally in Section 5.0. Pure bending was generated by means of a coupled rotation and displacement applied on the ends of the cable. The pure bending motion of the cable consists of moving the ends closer together as they are rotated in opposite directions relative to one another as illustrated in Figure 6.2(a). The exact displacement and rotation required to produce a certain bending diameter for any given length cable can be calculated analytically.

The displacement and rotation degrees of freedom in the bending model were applied to the ends of the cable using pilot node multipoint coupling constraints. The multipoint constraints coupled the motion all the nodes on the end of the cable, including the nodes on the tapes and support structure, to the rigid body motion of a pilot node located on the end of the cable in its exact center. Equal and opposite degrees of freedom were applied to the ends of the cable in steps, incrementally bending the cable to smaller diameters.

Transverse compression was applied to the cable model as a distributed load acting only on the HTS tapes as shown in in Figure 6.2(b). The internal transverse load was applied to each HTS tape as uniformly distributed nodal forces. This type of internally applied transverse load is representative of the true electromagnetic Lorentz load which can develop on TSTC carrying current in background magnetic fields.

In the transverse compression model, the distributed load was always applied in a vertical downward direction, perpendicular to the bottom plate, and the tape stack geometry was rotated to analyze the angle dependence of the load. In the model, the cable geometry was supported on the bottom by a rigid plate which

was fixed. The exterior of the tube was also constrained not to rotate. The internal HTS tapes were confined using contact sets.

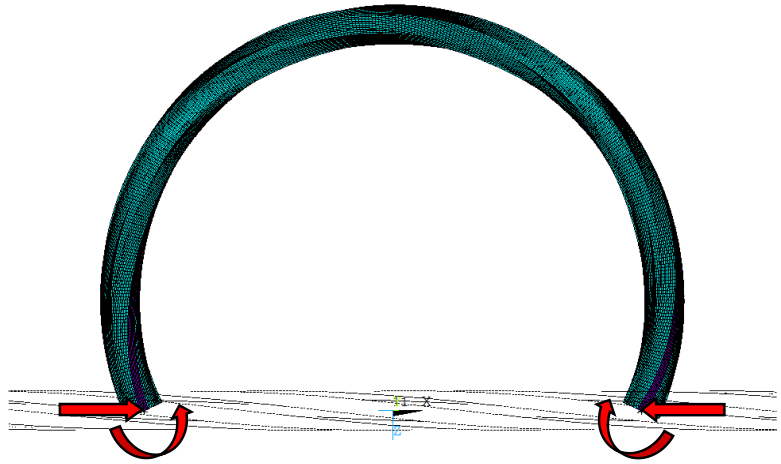

(a)

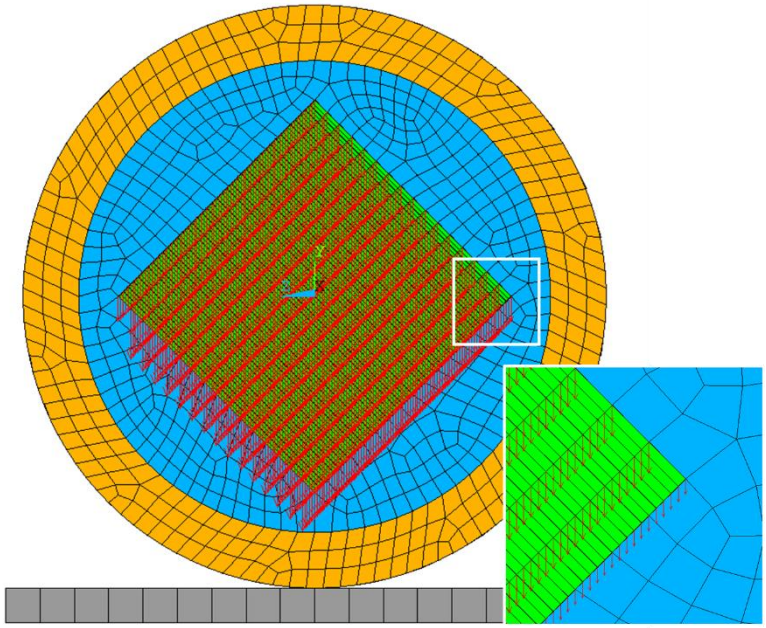

(b)

Figure 6.2 – (a) Schematic depiction of a coupled displacement and rotation load used to apply pure bending to HTS cables [44] and (b) internal distributed electromagnetic transverse load applied to a TSTC inside a solder filled tube [50].

6.1.6 Critical Current Estimation

For the finite element cable models under bending, the axial strain state of every HTS tapes was analyzed and used to estimate the critical current performance of the cable in a similar fashion to what was done for single tapes in

Section 4.1.5. The critical current could not be predicted from the transverse compression models due to a lack of experimental data. The normalized critical current behavior of the HTS cables under bending was estimated from the numerical models using the following steps [73].

Step 1: *Define an analytical relationship for the average critical current through the width of the tape.* The axial strain in a twisted HTS tape under bending (which is the case for the tapes in the TSTC and the HTS CICC under bending) varies both through the width and along the length of the tape. For simplicity the axial strain variance through the width of the tape was first evaluated by averaging the critical current over the width of the tape similar to what was done for single tape models. The average critical current ($I_{c\theta}$) over the tape width ($2w$) was determined using the following integration,

$$I_{c\theta} = \frac{1}{2w}\int_{-w}^{w} I_c(\varepsilon_{x\theta})\, dx\,. \tag{4}$$

The critical current as a function of the axial strain ($\varepsilon_{x\theta}$) was evaluated using equation (2) from Section 4.1.5 which approximates published experimental critical current results [63] with a sixth order polynomial.

Step 2: *Calculate average critical current through the width of each tape using finite element analysis results.* Structural finite element analysis of stacked-tape cables under bending can be used to identify the axial strain in each individual tape within the cable. To estimate the critical current in these tapes from the numerical cable model, the axial strain through the width of the tape was recorded at 72 locations along its length over one full twist pitch corresponding to twist angle (θ) increments of 5°. The numerical strain results were then used to

solve the equation (4) with a numerical Gaussian integration as done in Section 4.1.5 for single tapes.

Step 3: *Evaluate the critical current along the length of the tape using an analytical relationship.* The axial strain in a twisted bent tape does not only vary through its width but also along its length. The averaged critical current through the tape width determined in Step 2 was calculated at numerous twist angles. The variation of the average critical current along the length of the tape was evaluated by taking an integral of the total voltage over the one full twist pitch length (L_p) using an electric field criterion of 100 μV/m and n = 25. The overall tape critical current (I_{cTape}) was determined using the following equation,

$$I_{cTape} = \sqrt[n]{\frac{L_p}{\int_0^{L_p} I_{c\theta}{}^{-n}\, dl}} = \sqrt[n]{\frac{72}{\sum I_{c\theta}{}^{-n}}}\,. \tag{5}$$

The integration of the averaged critical current along the length was approximated simply as a summation of the averaged critical current at all 72 locations along the tape length. Additional details are provided in [73].

6.2 Bending

The twisted stacked-tape cable and the HTS slotted-core CICC were both analyzed under pure bending using full scale three-dimensional numerical models [44]-[49]. As previously mentioned, understanding the smallest bending radius achievable without performance degradation in the cable is essential to its future implementation in high field magnet coils.

The electromechanical performance as a function of applied bending diameter for both cable types was analyzed using finite element analysis. SuperPower and

SuNAM tapes were used in the TSTC and HTS CICC models respectively. Initial simulations were performed to validate the numerical models ability to accurately capture the electromechanical bending behavior of a full scale cable. The influence of friction on the relative motion of neighboring tapes was also investigated. Most importantly the full scale cable models were used to estimate the critical current performance of ever tape within the cable using axial strain data as was done for single tapes. The predicted critical current behavior of the HTS CICC under bending was compared with the experimental results presented in Section 5.1.2 for model validation.

6.2.1 Model Details

Full scale pure bending models were developed for a generic twisted stacked-tape cable and the HTS slotted-core CICC. For both cables, one full twist-pitch was modeled so that all of the internal tapes will pass through both the tensile (outer edge) and compressive (inner edge) regions along the length of the cable under bending. The TSTC was modeled with a 200 mm length consistent with current twist-pitch length being used for the cables. The HTS CICC was modeled with a 500 mm length which corresponds to the twist pitch used in the short twist pitch (STP) cable described in Section 5.1.

The generic TSTC was modeled with a 40-tape stack of SuperPower HTS tapes which were supported in a solid cylindrical copper core as seen in Figure 6.3. The core was modeled so that the geometry of the slot perfectly matched that of the tape stack. The TSTC model was analyzed for two configurations; a centrally located tape stack Figure 6.3(a) and a tape stack offset a radial off-center

distance (*h*) Figure 6.3(b). The two configurations were analyzed to show how all stacked-tape cables (including the HTS CICC) have similar electromechanical behavior under bending and can be modeled in the same manner.

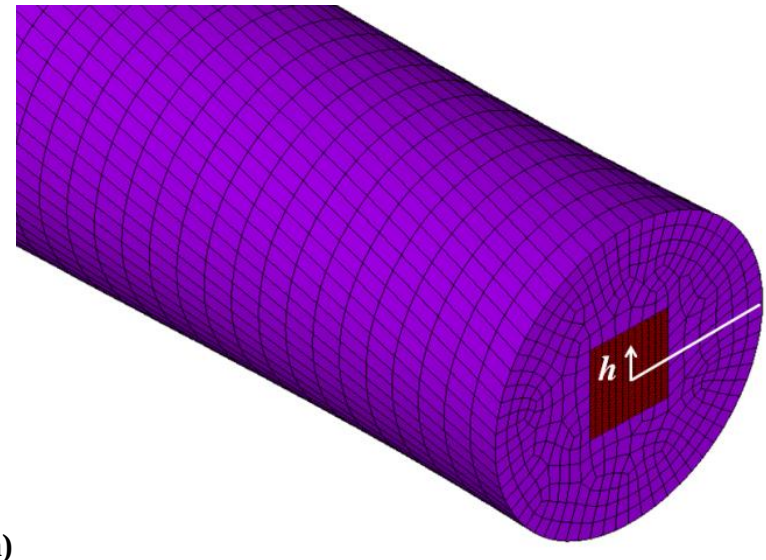

(a)

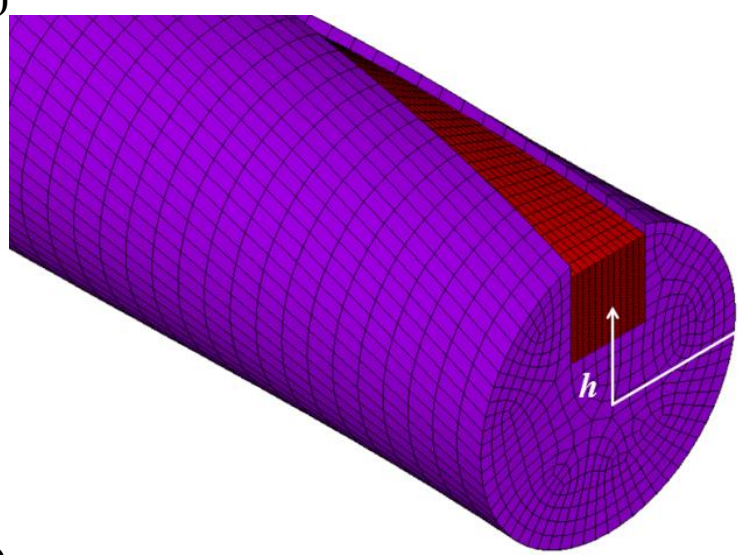

(b)

Figure 6.3 – Images the generic TSTC models analyzed under bending. (a) A centrally located tape stack and (b) a tape stack offset a radial distance of (*h)* [44].

For the TSTC model, contact sets were used to control the internal behavior of the HTS tapes within the cable under bending. Contact pairs were defined between all neighboring tapes and between the tape stack and the copper core. These contact sets were used to analyze two extreme cases: perfect-slip and no-

slip. The perfect-slip case was modeled with frictionless contacts while the no-slip case was modeled with bonded contacts.

The meshed model of the HTS CICC is shown in Figure 6.1(b) and contains a slightly simplified geometry from the actual cable design. The base of the channels were flat, the copper spacers are a single volume and the width of the channels were defined the same as the HTS tapes. The influence of the external jacket was also determined to be negligible with appropriate boundary conditions and therefore was excluded from the models. Also, as seen in Figure 6.1(b) only one of the five slots was filled with a tape stack, which was deemed adequate considering every slot experiences the same bending loads over one complete twist pitch of the cable, 500 mm. The tape stack was modeled with nineteen SuNAM tapes as was tested in the experiments.

Surface-to-surface contact pairs were used to define all interactions within the cable, as was done in the TSTC model. Specifically, contacts were set up between each neighboring tape, between the tape stack and the core, between the tape stack and copper spacer and also between the core and the copper spacer. These contacts were used to investigate the influence of friction on strain state of the HTS tapes and consequently on their critical current behavior under bending. A range of friction coefficients (1.0, 0.2 and 0.02) were analyzed. A coefficient of 1.0 is a typical value for dry copper-to-copper contact [74], a coefficient of 0.2 is a characteristic value for metal-to-metal contact with liquid nitrogen lubrication [75] and a coefficient of 0.02 represents a nearly frictionless condition.

A controlled bending load was applied to the numerical cable models by an equal and opposite, coupled displacement and rotation on the ends of the cable.

The bending load is schematically depicted in Figure 6.2(a). The rotational and translation degrees of freedom were applied to the ends of the cable using pilot node multipoint coupling constraints as done in the single tape simulations. The bending load was applied incrementally down to a final bending diameter of 0.25 m as was done in the experiments.

The numerical simulations were used to identify the axial strain of every HTS tape within the cables as a function of applied bending diameter. The strain through the width of each tape was recorded at numerous increments along each tapes length. These strain results were coupled with an analytical model to estimate the critical current performance of every tape within the HTS cables as a function of bending diameter. The numerical strain results and estimated critical current behavior were validated using an analytical bending model and the experimental data provided in Section 5.1.2.

6.2.2 Results

The strain in every tape of a generic twisted stacked-tape cable under bending was analyzed using finite element analysis. The numerical bending strains as a function of twist angle of four HTS tapes in the TSTC models are displayed in Figure 6.4. The bending strain refers to the longitudinal strain under bending and the twist angle is a measure of the position along the length of the cable over one full twist pitch. The strain results were analyzed for a bonded or no-slip case (a) and a frictionless or perfect-slip case (b). The presented bending strains are for a bending diameter of 0.3 m and were recorded from the edge of the tapes. The strain results are displayed for four tapes having radial off-center distances (h) of 0, 2, 4, and 6 mm.

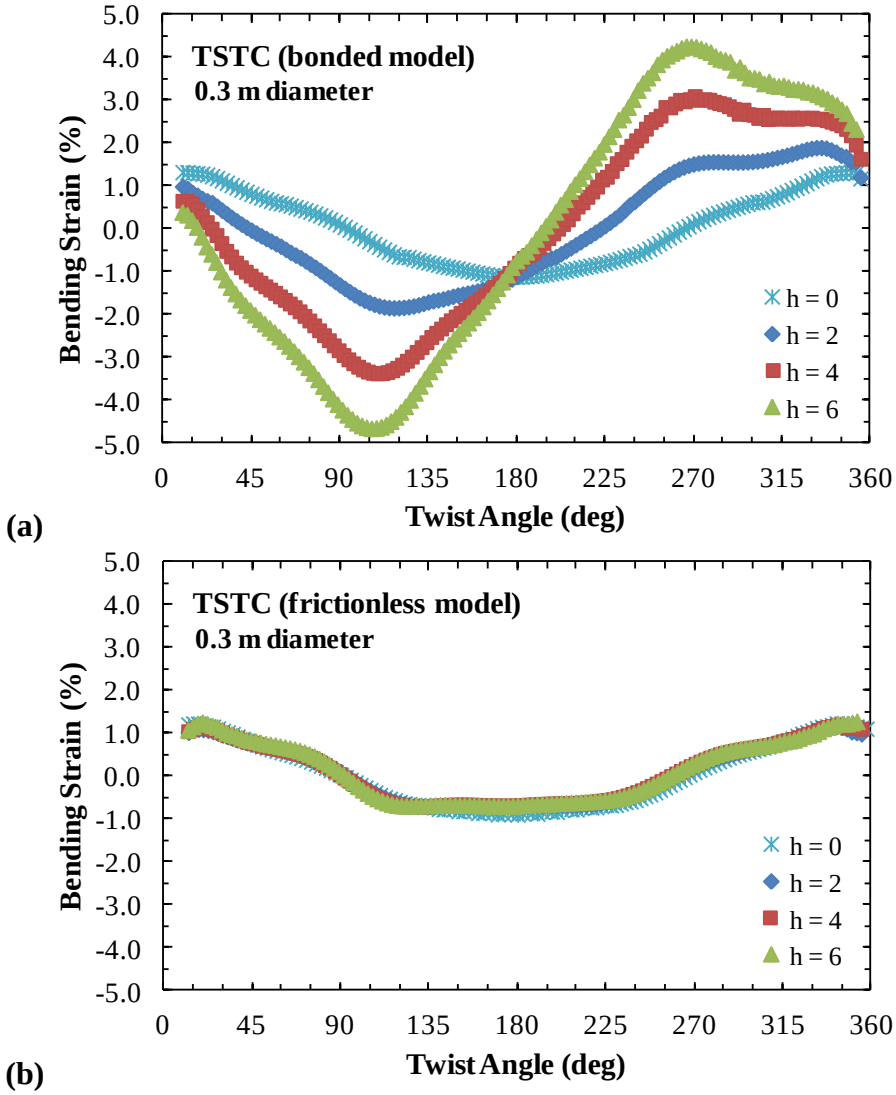

Figure 6.4 – Plots of numerical bending strain as a function of the twist angle for four HTS tapes in a TSTC under a 300 mm bending diameter. (a) Bonded model and (b) frictionless model [44].

The results from the bonded model shown in Figure 6.4(a) indicate that the bending strains of the tapes are highly dependent on the radial off-center distance. Tapes located further from the center of the cable (larger *h*) will experience much higher tensile and compressive bending strains large enough to degrade their critical current performance. This behavior is likely due to the fact that the tape stack acts as a single volume with no relative motion occurring between neighboring tapes.

In contrast, the results from the frictionless model shown in Figure 6.4(b) indicate that all four tapes undergo the same strain along the length of the cable regardless of their radial off center distance. The strain profile of all four tapes in the frictionless model matches the strain found in the center tape (h = 0) in the bonded model. The reduction of the strain for tapes with a larger radial off-center distance is due to the fact that the tapes can freely slide with respect to each other, likely allowing the compressive and tensile regions over one twist-pitch to cancel.

These numerical strain results were evaluated against an analytical bending model for validation. The analytical model calculates the bending strain of each tape based on its relative geometric location within a twisted bent cable as described in [73]. The analytical model can analyze a no-slip (bonded) and a perfect-slip (frictionless) case. Figure 6.5 plots the bending strain results as a function of twist angle from both the analytical and finite element models. The results are again shown for a bending diameter of 0.3 m and were recorded from the edge of a tape located at a radial off-center distances (h) of 6 mm.

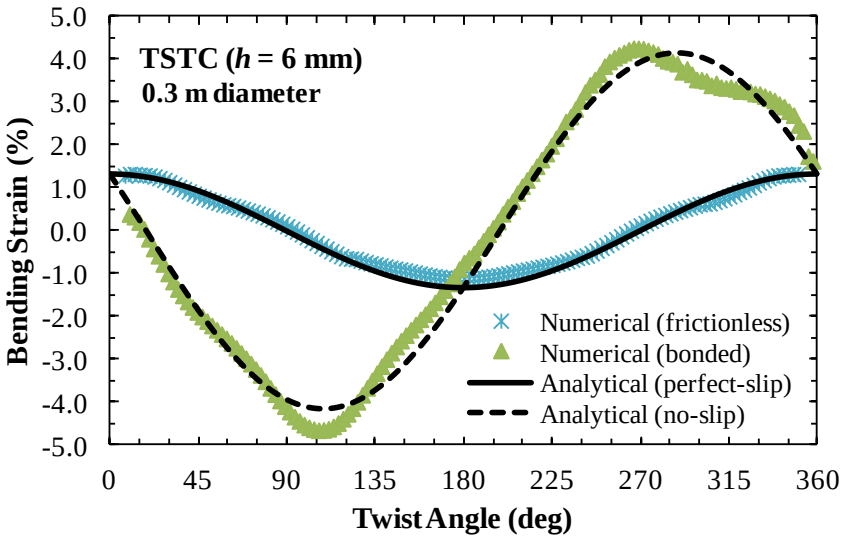

Figure 6.5 – Plot of the analytical and numerical bending strain as a function of the twist angle of the TSTC under a bending diameter of 0.3 m.

As it can be seen from the plot, the bonded numerical results are a close match to the analytical no-slip case confirming the dependence of strain on the radial off-center position of the tapes. Similarly, the frictionless numerical results agree well with the analytical perfect-slip case validating that the strain is independent of the tape position when the tapes are able to freely slide. Overall, the numerical results have more angular behavior and a slight asymmetry compared to the smooth analytical strain profiles. The cause of these numerical results may be an artifact of the mesh being too coarse, nonlinear contact interactions or most likely end effects caused by the load application.

Following the relative successful modeling of a generic TSTC conductor, the bending performance of the HTS slotted-core CICC was analyzed. Considering the actual friction within the cable under bending is not well understood, the effect of friction on the strain characteristics and critical current behavior of the HTS CICC was evaluated. The numerical bending strain in the HTS CICC as a function of twist angle for three different friction coefficients (1.0, 0.2 and 0.02) under a 0.5 m bending diameter are plotted in Figure 6.6. The numerical results are presented for the strain on the edge of tape thirteen in a stack of nineteen tapes which corresponds to a radial off-center distance of 6.7 mm in the HTS CICC. In Figure 6.6, the bending strain results are compared against the analytical model for a perfect-slip (frictionless) case and a no-slip (bonded) case.

The results for a friction coefficient of 0.02 were found to agree well with the perfect-slip analytical case (solid line) indicating that in the numerical model the tapes were able to slide freely with respect to each other and the core. The strain

profile for a friction coefficient of 0.2 was found to be slightly greater than the perfect-slip case which signifies that the tapes in the model can slide but with some resistance. The strain results for a friction coefficient of 1.0 were found to be significantly higher than the 0.2 and 0.02 models and had clear tensile and compressive peaks similar to the no-slip analytical case (dashed line).

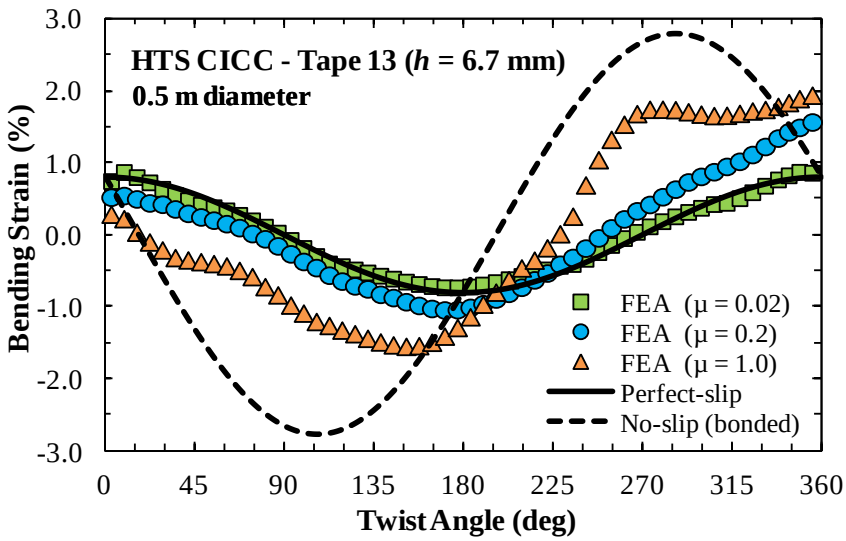

Figure 6.6 – Plot of the numerical bending strain as a function of the twist angle in the HTS slotted-core CICC under a 0.5 m bending diameter [44],[49].

Considering the strain in the numerical model was found to be clearly less than the no-slip case suggests that there is relative motion (sliding) occurring between neighboring tapes, however considering the strain was also much higher than the perfect-slip case suggests that the tapes have a high sliding resistance, enough so that the tensile and compressive strain regions cannot cancel each other. Overall, friction was found to have a considerable influence on the strain characteristics of the HTS CICC cable under bending.

The bending strain results along the length, as shown in Figure 6.6, and through the width of every tape in the numerical HTS CICC model were used to estimate each tapes critical current performance under bending with the method

outlined in Section 6.1.6. The estimated critical current performance of tape 13 as a function of bending diameter for the same three friction coefficients (1.0, 0.2 and 0.02) is shown in Figure 6.7. The numerical critical current results were compared with the experimental results presented in Section 5.1.2. The experimental results were average for all tested tapes in position 13, error bars were added to indicate the spread of results and a polynomial trend line was fit to the experimental data.

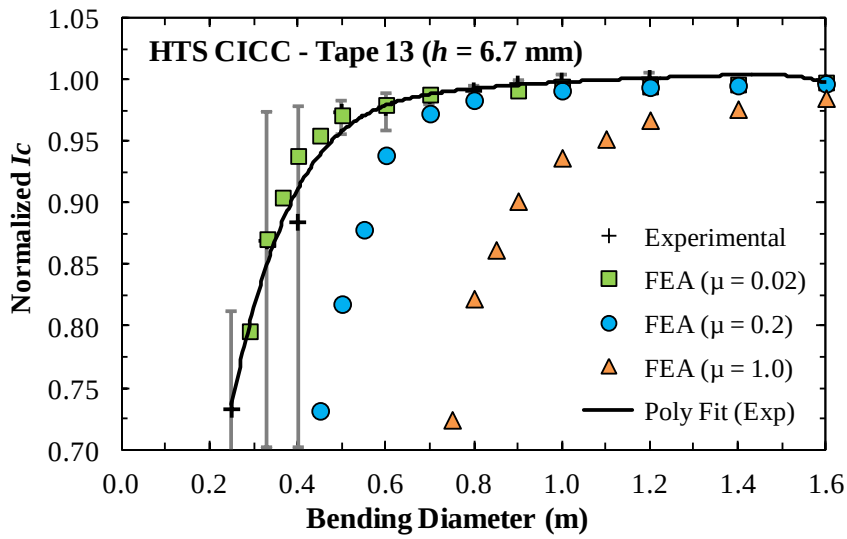

Figure 6.7 – Plot of the normalized critical current as a function of bending diameter for the HTS CICC as predicted from the finite element strain results with various friction coefficients [44],[49].

The polynomial fit to the averaged experimental critical current data for tapes in position 13 of the stack, shows a sharp degradation occurring after 0.5 m bending diameter, as previously reported in Section 5.1.2. Below this bending diameter, the error bars also indicate an increased variability between tested tapes. The estimated critical current behavior of the nearly frictionless model (coefficient of 0.02) predicted an almost identical critical current degradation as was experienced experimentally. The numerical data points all fell within the

experimental error bars and had a very close overall agreement with the polynomial fit. This agreement suggests that the real tapes in an HTS CICC are able slide freely with respect to each other in a nearly frictionless manner.

The estimated critical current results from the numerical strain data in the 1.0 and 0.2 coefficient models highlight an important and significant influence of friction on the critical current degradation under bending. The models with a coefficient of 0.2 and 1.0 experienced sharp degradations occurring at 0.7 m and 1.2 m bending diameters respectively. Therefore, higher friction in the HTS CICC results in larger bending strains, as seen in Figure 6.6, and consequently early critical current degradation, as seen in Figure 6.7.

6.3 Electromagnetic Transverse Compression

Cable support structures for the twisted stacked-tape cable were investigated under internal uniformly distributed transverse compression using full scale three-dimensional models [50]. As mentioned earlier, transverse compression is generated from natural electromagnetic Lorentz forces acting on the cable. High current density cables, like the TSTC, operating in high magnetic fields can experience very large electromagnetic transverse loads able to degrade the performance of the cable without appropriate support structures.

The stress and strain state of the HTS tapes in a TSTC under electromagnetic transverse loads was analyzed using finite element analysis. A typical 40-tape TSTC made from SuperPower tapes was modeled with two different support methods: a solid cylindrical copper core and a solder filled copper tube. The influences of the stack orientation angle and friction on the resulting deformation

and maximum stress in the cable cross section were evaluated for both support structures. The numerical stress results through the width and thickness of the tapes were compared to the experimental critical current results for single tapes under transverse stress on their thin edge and wide face presented in Section 3.4.2.

6.3.1 Model Details

Full scale three-dimensional cable models were developed for electromagnetic transverse compressive loads. Two 40-tape twisted stacked-tape cable models were created with two different cable support methods. The first method supported the tape stack inside a solid cylindrical copper core (a) while the second method supported the tape stack inside a copper tube filled with solder (b) as shown in Figure 6.8. Both cable supports have the same external diameter of 8.4 mm for consistency and the copper tube model has a wall thickness of 0.8 mm. Both models also use rigid plates beneath the cable to support against the applied compressive loads.

In both models the internal tape stack was straight (untwisted). This was done to analyze the angle dependence of the transverse load on the tape stack. Considering both the geometry (straight tape stack) and the applied load were uniform along the length of the cable, a length of only 20 mm was used in the numerical models with symmetry style end conditions to reduce their size and computation time. Considering the relative short length of the models, a finer mesh discretization was used through the cross section of the cable.

Surface-to-surface contact pairs were used for all interactions within the cable including the contact between adjacent tape and the contact between the tape

stack and cable support. These contact pairs were used to investigate the influence of friction (and bonded contact) on the maximum stress and strain through the cross section of the tape stack. A contact pair was also created for the exterior of the cable support and the rigid bottom plate.

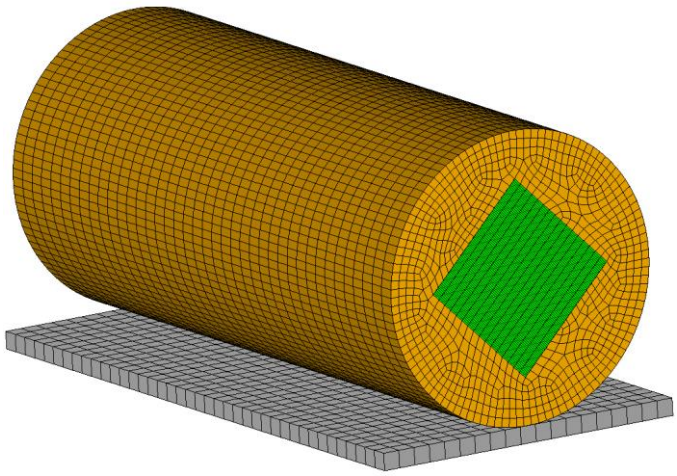

(a)

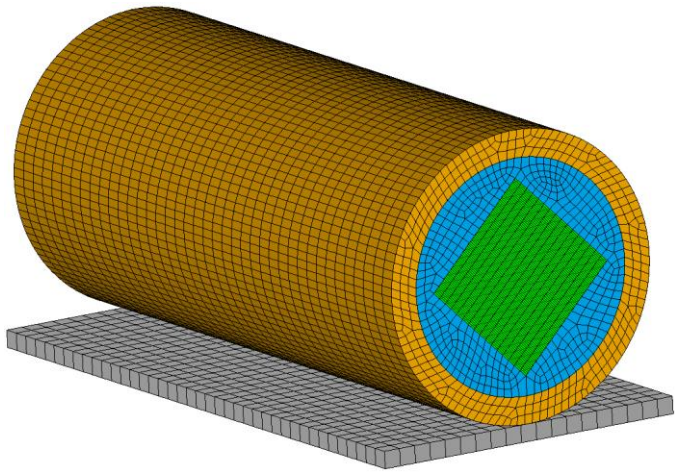

(b)

Figure 6.8 – Images of a typical 40-tape TSTC having a stack rotation of 45˚ with two different support methods; (a) a solid copper core and (b) a solder filled copper tube [50].

A maximum 300 kN/m transverse compressive load was applied to the tape stack in the numerical models. This corresponds the electromagnetic Lorentz force (B x I) generated on a TSTC carrying 20 kA in a background field of 15 T. The transverse load was applied incrementally in 25 kN/m steps. The entire load on the tape stack was divided evenly between all forty tapes. The load in each

tape was then distributed uniformly through its width and length. The load was applied to each tape as nodal forces as shown in Figure 6.2(a). This type of internal uniformly distributed load is an accurate representation of a real electromagnetic load and will allow the load to accumulate through the tape stack.

In the models, the transverse load was always applied downward perpendicular to the bottom plate and the orientation of the tape stack was rotated. Separate models were run for various tape stack orientations between 0° and 90°, a stack rotation of 45° is shown in Figure 6.8. At an angle of 0° the transverse load is acting perpendicular to the wide face of the tapes and for 90° is acting parallel. The results as a function of stack orientation angle for a straight tape stack can be used to predict the characteristics of an actual twisted stacked-tape cable.

The numerical simulations were used to identify the stress and strain of every tape as a function of applied transverse load. The maximum stress and strain in the tape stack, in the width, thickness and length directions, was recorded and used to evaluate the influence contact friction and stack orientation angle. The numerical stress results were compared to the experimental single tape transverse compression data shown in Section 3.4.2 for validation.

6.3.2 Results

The effectiveness of two support methods for a 40-tape TSTC under electromagnetic transverse compression was evaluated by investigating the maximum stress and strain within the tape stack under load. The stress and strain through the width and thickness of every tape in the stack was analyzed. An example of the stress through the cross section of the tape stack in the width (a)

and thickness (b) directions are displayed in Figure 6.9, for a solid copper core model with an angle of 45° and a load of 300 kN/m.

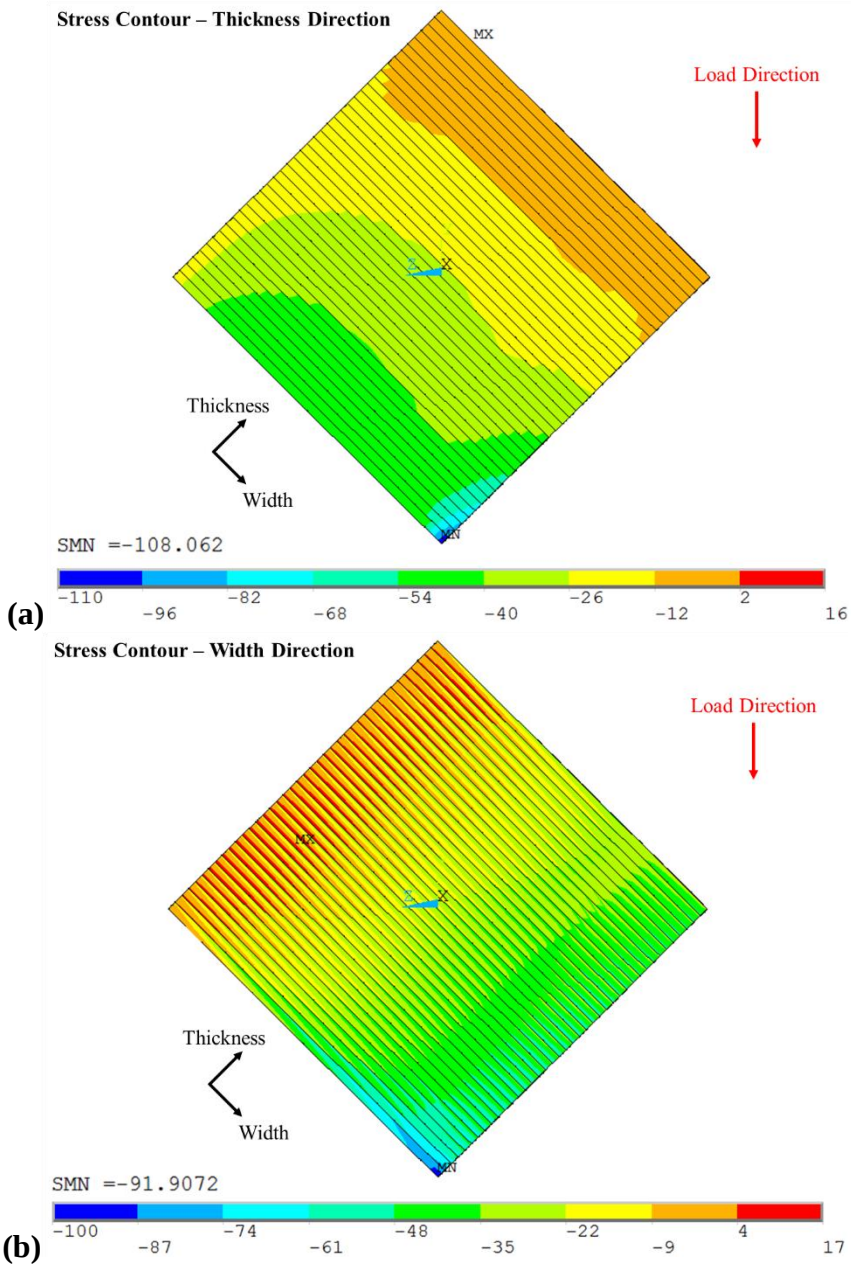

Figure 6.9 – Stress contours in a solid copper core TSTC with a 45° stack rotation angle and a 300 kN/m load [50]. (a) Stress in the thickness direction and (b) stress in the width.

The stress contour plots for the 45° rotated model, nicely illustrate how certain stack orientation angles result in an accumulation of electromagnetic load on the sides and edges of the tape stack creating stress concentrations (local regions of

high stress). The maximum compressive stress in the tape stack occurs in these stress concentration regions as indicated in blue in Figure 6.9.

The maximum compressive stresses in the cross section of the tape stack for the width and thickness directions were used as a means to compare the numerical models. It should be noted that, the maximum stress was used as a value for relative comparison between models but does not necessarily reflect the actual performance of the entire cable since the maximum value typically occurs at a small localized stress concentration meaning the majority of the tapes in the stack do not experience that high of a stress level.

The maximum compressive stress in the thickness (a) and width (b) directions as a function of applied load are plotted in Figure 6.10 for both cable support methods (solid copper core and solder filled copper tube). The results were evaluated in 25 kN/m steps up to a maximum transverse compressive load of 300 kN/m. Results for three different stack orientation angles are also plotted to highlight its impact on the maximum stress.

The results in Figure 6.10 were taken from models with the following contact settings. Both models for consistency prescribed sliding contact with a friction coefficient of 0.2 between every neighboring tape in the stack. For the solid copper core model, a sliding contact with a friction coefficient of 0.2 was also defined between the exterior of the tape stack and the copper core. For the solder filled copper tube model, the exterior surface of the tape stack was defined as bonded or glued to the surrounding solder geometry. Besides the contact settings, the only other differences between the two models are their support geometries,

solid copper core and solder filled copper tube. The stress contours for the solid copper core model shown in Figure 6.9 also use these same contact settings.

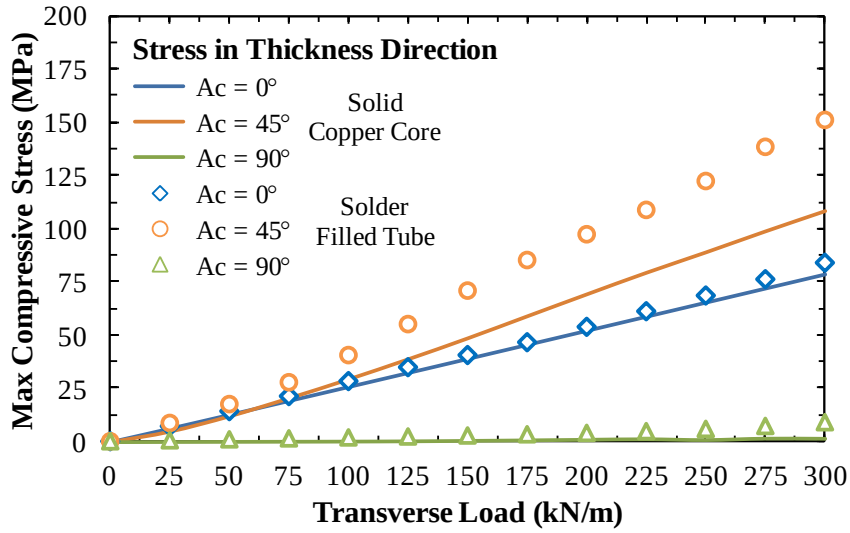

(a)

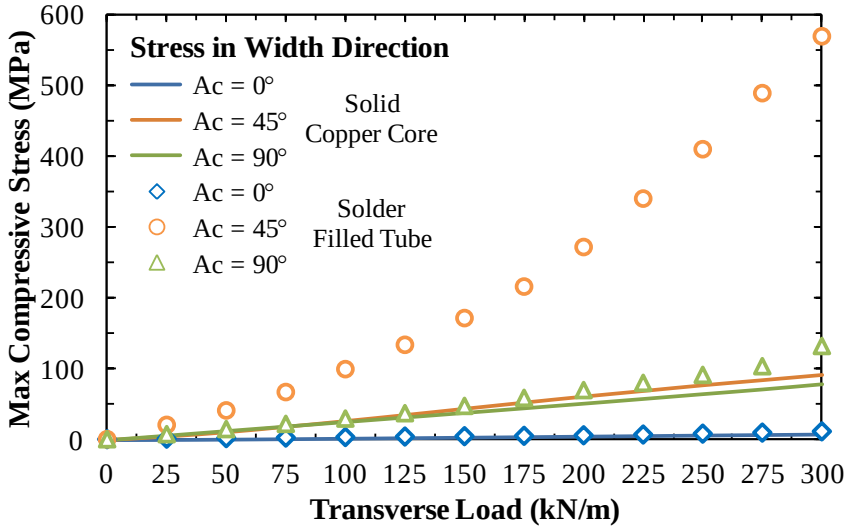

(b)

Figure 6.10 – Plots of maximum compressive stress in the TSTC as a function of applied transverse load for three different stack orientation angles (Ac) [50]. (a) Plot of stress through the thickness and (b) plot of stress through the width for both a solid copper core support and a solder filled copper tube support.

In Figure 6.10, for stack orientation angles of 0° and 90°, when the tapes are aligned perpendicular and parallel to the applied load, a maximum stress of 75 MPa is anticipated for a maximum load of 300 kN/m and a (4 mm x 4 mm) tape stack cross section. This stress agrees well with the numerical values

presented in the figure. The corresponding results for a stack orientation of 45° in both cable models reveals a consistently higher maximum compressive stress in both the width and thickness directions. This higher max stress behavior is also seen for other angles between 30° and 60° and is likely attributed to local stress concentrations that develop near the edge of the tape stack as shown in Figure 6.9.

The maximum compressive stress results as a function of applied transverse load shown in Figure 6.10 follow a nearly linear increase under increasing applied load. For any of the three plotted angles, a comparison of the results from the solid copper core model and the solder filled copper tube model indicates that later model experiences higher maximum compressive stresses. This difference is especially evident for a 45° angle at which the solder filled copper tube experienced roughly 1.5 times higher stress through the thickness and 6 times higher stress in the width. The likely cause of the significantly higher stress in the solder filled copper tube model is the considerably larger cross sectional deformation, roughly 5 times, that was experienced due to the relatively weak material properties of solder.

The influence of friction on the maximum stress in both cable models was also evaluated for the worst case condition of a 45° angle and a load of 300 kN/m. The resulting maximum compressive stresses for the width and thickness directions along with the cross sectional deformations are listed in Table 6 for five friction coefficients (0, 0.02, 0.05, 0.1, 0.2, 0.4 and 0.8). The results from a perfectly bonded condition (no sliding) were also presented for comparison.

For the solid copper core model, increasing the friction between tapes and between the tape stack and core was found to slightly increase the maximum stress in the tape stack in both the width and thickness directions. The deformation was also found to slightly decrease under higher friction.

Table 6 – Influence of friction on the maximum stress and deformation in a 45° rotated tape stack under 300 kN/m of transverse compression [50].

	Solid Copper Core			Solder Filled Tube		
Friction (μ)	**Stress** (GPa)		**Deformation**	**Stress** (GPa)		**Deformation**
	Thickness	Width	(mm)	Thickness	Width	(mm)
0.00	88	64	0.037	175	742	0.195
0.02	92	71	0.036	168	721	0.191
0.05	95	76	-	157	692	0.186
0.10	100	84	0.033	140	647	0.176
0.20	108	92	0.030	110	569	0.159
0.40	115	97	0.027	117	437	0.130
0.80	-	-	-	163	312	0.095
bonded	100	109	0.017	125	187	0.042

The solder filled copper tube model experienced a much larger impact from friction and saw the opposite stress behavior as seen in the solid copper core model. For the solder filled copper tube, larger friction coefficients were found to noticeably reduce the cross section deformation by restricting the relative motion of the adjacent tapes causing the tape stack to act more like a single volume. A friction coefficient of 0.8 restricted the deformation by over half compared to the frictionless case. This improvement in the cross section deformation under higher friction resulted in a significantly lower maximum stress experienced in the tape stack, particularly in the width direction which saw a stress reduction of nearly 60 percent compared to the frictionless case.

Overall, the stack of tapes was determined to be better supported against electromagnetic transverse compressive loads (lower maximum stresses) using a solid cylindrical copper core support. The stress through the width of the tapes was also determined to have the highest potential to degrade the cable (especially in the case of a soldered filled copper tube with a 45° angle). A higher level of friction was found to significantly improve the stress results for the solder filled copper tube model by reducing the cross section deformation while for the solid copper core model was found to have a slight negative impact.

6.4 Summary and Future Work

A methodology for modeling full scale three-dimensional stacked-tape cables under bending and electromagnetic transverse compression was developed which incorporated parameterized geometry and modifiable contact pair relationships to define the interactions between neighboring geometries. The HTS tapes in the cable were modeled with the same solid-shell technique used for single tapes.

Under bending, a generic TSTC model was first developed to validate the numerical models ability to accurately capture the bending behavior of a full scale cable. Detailed results for the bending strain along the length of every tape within the generic TSTC models were evaluated for two conditions: frictionless and bonded. The tapes in the frictionless model were able to freely slide with respect to each other which was found to reduce their bending strain by allowing the tensile and compressive regions to cancel over one twist-pitch. These numerical strain results were found to have good overall agreement with an analytical model for perfect-slip and no-slip conditions.

A model of the HTS slotted-core CICC was developed next and was used to investigate the influence of friction on the bending performance of the cable. The numerical bending strain results were coupled with an analytical relationship to predict the critical current performance in each tape. The results indicated that friction in the cable has a significant influence on bending strain and therefore the critical current of the cable. Higher friction leads to larger bending strains and earlier critical current degradation.

The experimental critical current bending behavior was found to be well characterized by a nearly frictionless numerical model, coefficient of 0.02. This confirmed that the tapes in the cable can slide freely during bending allowing their tensile and compressive strain regions to cancel. The relative motion between the tapes was found to lower the bending strain in the cable and as a result improve the critical current performance.

One future work topic for modeling full scale stacked-tape cables under bending should be investigating the wavy or angular bending strain results seen along the length of the individual tapes. Potential causes for this strain behavior that should be studied are the mesh density as well as end effects arising from the load application in the limited length one twist pitch models.

Under electromagnetic transverse compression, two 40-tape TSTC models were developed; one in a solid cylindrical copper core and one in a solder filled copper tube. The two models were used to investigate how effective different cable support structures were at protecting the HTS tapes from degradations caused by electromagnetic loads. The TSTC models where initially simulated in a

straight untwisted configuration and the angle dependence of the load and the influence of friction were investigated.

Detail stress and strain results through the width and thickness directions in every tape in the TSTC were evaluated. The maximum compressive stress in the cable cross section was evaluated for both cables and was found to linearly increase under increasing electromagnetic load. Stack orientation angles around 45° were found to experience the greatest maximum compressive stresses due to load accumulation and stress concentrations in the tape stack. Higher friction was also found to actually reduce the deformation and stress characteristics of the solder filled copper tube model.

Overall, the TSTC was determined to be better supported against electromagnetic transverse compressive loads using a solid cylindrical copper core support instead of a solder filled copper tube. The stress through the width of the tapes was also determined to have the highest potential to degrade the tapes and cable.

Future work for the transverse compression modeling of TSTC should include analyzing twisted cables and comparing their results to the straight cable results analyzed in this work under different stack orientation angles. In addition to this, considering the cable fabrication of a TSTC inside a solid copper core is more challenging and costly, the future work should also focus on optimizing the design of the solder filled tube support method by investigating the tube diameter, tube thickness and tube material.

7.0 Conclusion

Experimentation and numerical modeling have been used to investigate the electromechanical behaviors of single HTS tapes and HTS cables under various anticipated fabrication and operational loads. The aim of this work was to advance high temperature superconductors for their future implementation in high field magnet applications like fusion energy and high energy physics.

The novelty of this work was the coupling of laboratory tests with finite element modeling which provided unique insights into the true electromechanical characteristics of these HTS tapes and cables. Experiments were used to measure critical current performance as a function of applied load and to characterize mechanical characteristics while structural finite element analysis was conducted to investigate the mechanical characteristics and strain dependence of the critical current under each type of analyzed load.

Experiments were performed on commercially available HTS tapes from three manufacturers: SuperPower, SuNAM and American Superconductor. Single tapes from each manufacturer were tested under pure torsion, axial tension, combined tension-torsion and transverse compression on their wide face and thin edge. Custom experimental equipment for each load type was developed to measure the critical current and mechanical properties of individual tapes under 77 K, self-field conditions.

Under pure torsion the critical current of single HTS tapes remained unchanged down to a twist pitch of 120 mm after which a slight reversible decrease was experienced. Below a twist pitch of 80 mm all tapes experienced a

rapid irreversible degradation of critical current. The mechanical characteristics of each tape were different but all experienced an exponential increase in torque for decreasing twist pitch length.

Under axial tension the tested HTS tapes were found to have a gradual reduction of critical current under increasing tension, followed by a steep irreversible degradation occurring near the yield strength of the tape as determined by comparison with their experimental stress-strain curves. SuNAM tapes experienced fairly repeatable critical current degradation at their yield stress while SuperPower tapes had large variability and experienced critical current degradation significantly below their yield strength.

Under combined tension-torsion load the critical current results of HTS tapes were found to be nearly identical to the pure tension results for twist pitch lengths longer than 150 mm. This indicates that the tensile load is dominant and the effect of the initial torsion strain is small for the tested twist pitch lengths. A mechanical characteristic of linearly increasing torque under increasing applied tension was also observed with a greater slope seen in samples with shorter twist-pitches.

Under transverse loads single HTS tapes were found to be far more sensitive to compression applied on their thin edge compared to compression applied to their wide face. AMSC and SuperPower tapes both experienced severe critical current degradation around 150 MPa of stress on their thin edge, while had no irreversible degradation above 400 MPa of stress on their wide face.

The single HTS tapes from each manufacturer were also analyzed using structural finite element analysis. A novel technique was developed for modeling

the layered composite structure of the HTS tapes using structural solid-shell elements. Each tape was simulated under the same conditions and loads tested experimentally: pure torsion, axial tension and combined tension-torsion.

The numerical models were able to closely replicate the experimental stress-strain curves of each HTS tape under tension and their torque behavior under torsion and combined tension-torsion loads. For every applied load, the finite element models were also able to produce detailed axial strain results in the superconducting layer of each HTS tape. These strain results were successfully paired with an analytical model to estimate the critical current performance of the HTS tapes under load. The numerically predicted critical current behaviors of each tape were found to have close agreement to experimental results for all three load types analyzed: torsion, tension and combined tension-torsion.

In addition to the single tape studies, the electromechanical performance of two HTS tape cabling methods designed for high field magnet applications were also investigated experimentally. The HTS slotted-core CICC was tested under bending and the twisted stacked-tape cable (TSTC) was characterized under transverse compression. Two custom experimental systems were designed: one to apply uniform bending and the other to apply mechanical transverse compression. Loads were applied to the cables at room temperature and the critical current was evaluated at 77 K, self-field conditions.

Under bending, both tested HTS CICC cables (short and long twist pitch) saw minimal overall critical current degradation down to a bending diameter of 0.5 m. At this bending diameter, all tested tapes from both cables had similar performance and experienced an average critical current reduction of only 2%.

Under further bending down to a 0.25 m diameter, an irreversible critical current degradation of the tapes was experienced with a greater variability between tapes, some performing better than anticipated and others performing worse.

Under mechanically applied transverse compressive loads, a 40-tape TSTC conductor placed inside a solder filled copper tube experienced critical current degradation for an applied stress greater than 40 MPa (400 kN/m). A more pronounced degradation in critical current was also seen on a soldered TSTC conductor under a localized two-point load. Overall, the TSTC conductors under transverse load performed better than expected compared to real degradations caused by electromagnetic loads in high field tests.

To augment the cable experiments, a methodology for modeling full scale three-dimensional HTS cables (TSTC and HTS CICC) was developed which incorporated parameterized geometry and modifiable contact pair relationships. In the cable models, the HTS tapes were modeled with the same solid-shell technique used for single tape simulations. The cable models were analyzed under bending and electromagnetic transverse compression. The influence of friction on the performance of the cables was also investigated for both load types.

Under bending, both a generic TSTC and the HTS slotted-core CICC models were found to capture the relative motion of neighboring tapes under bending. Their bending strain results for every tape within the cables were found to agree well with an analytical model for a frictionless (perfect-slip) and bonded (no-slip) case. The numerical strain results from the HTS CICC model were successfully coupled with an analytical relationship to predict critical current performance. The experimental critical current bending behavior was found to be well

characterized by a nearly frictionless numerical model, coefficient of 0.02, which confirms that the tapes are able slide freely during bending. It was also found that higher friction leads to larger bending strains and an earlier critical current degradation in stacked-tape cables.

Under a uniformly distributed internal transverse compressive load (representative of an electromagnetic load), the stress and strain of the HTS tapes in two TSTC conductors with different support structures were investigated. The tape stack in a solid cylindrical copper core was found to have lower maximum compressive stresses compared to a solder filled copper tube support. A stack orientation of 45° was found to consistently have the highest stresses in both models. The effect of friction was also found to impact the maximum stress in both cables particularly for the solder filled copper tube which saw a significant reduction in stress for higher friction factors. Overall, the solid copper core provided better support against electromagnetic transverse loads.

Overall, the coupling of the numerical modeling together with laboratory tests has provided unique insight into the mechanical behavior and electrical characteristics of HTS tapes and cables under various structural, thermal and electromagnetic loads. The close agreement seen between the experiments and finite element analysis has validated the electromechanical characteristics presented in this work. The novel single tape and cable investigations done in this work have helped: to improve cable processing methods for HTS tapes; to limit magnet fabrication degradations in HTS cables; and to maximize the operational performance of HTS tapes and cables in high field magnet applications.

8.0 References

[1] Buckel W *et al.* 2004 Superconductivity: fundamentals and applications, 2nd ed. Weinheim, Germany: *Wiley-VCH*.

[2] Chiesa L 2009 Mechanical and electromagnetic transverse load effects on superconducting Niobium-Tin performance *Doctoral Dissertation* Department of Nuclear Science and Engineering, MIT, MA.

[3] Meissner W and Ochsenfeld R 1993 Ein neuer effekt bei eintritt der supraleitfähigkeit *Naturwissenschaften* vol 21 no 44 pp 787–88.

[4] Bean CP and Livingston JD 1964 Surface Barrier in Type-II Superconductors *Phys. Rev. Lett.* vol 14 pp 12.

[5] Lee P *et al.* 2014 Applied Superconductivity Center, NHMFL http://fs.magnet.fsu.edu/~lee/plot/plot.htm.

[6] Superconductivity: Applications (online) 2016 https://en.wikipedia.org/wiki/Superconductivity#High-temperature_superconductivity.

[7] Large Hadron Collider Design Report, Chapter 7: Main magnets in the arcs, LHC (online), http://lhc.web.cern.ch/lhc/LHC-DesignReport.html.

[8] ITER technical basis, The plant description document, Chapter 2.1 Magnets, ITER (online) http://www.naka.jaea.go.jp/ITER/official-J/pdfs/PDD2-12.pdf.

[9] GE Healthcare: Magnetic Resonance Imaging (online) 2016 http://www3.gehealthcare.com/en/Products/Categories/Magnetic_Resonance_Imaging

[10] American Superconductor website (online) 2016 HTS Wire page http://www.amsc.com/solutions-products/hts_wire.html

[11] SuperPower Inc website (online) 2016 2G HTS Wire page http://www.superpower-inc.com/content/2g-hts-wire

[12] SuNAM Co, Ltd website (online) 2016 2G HTS Wire Catalog http://www.i-sunam.com/home/en_company,4,1,4,4

[13] SuperOx website (online) 2016 2G HTS Tape page http://www.superox.ru/en/products/42-2G-HTS-tape/

[14] Fujikura Europe Ltd website (online) 2016 2G High Temperature Superconductor http://www.fujikura.co.uk/products/energy-and-environment/2g-ybco-high-tempurature-superconductors/

[15] Bruker Corporation website (online) 2016 YBCO 2G HTS Superconductors page https://www.bruker.com/products/superconductors-and-metal-composite-materials/superconductors/ybco-2g-hts-superconductors/overview.html

[16] Goldacker W *et al.* 2014 Roebel cables from REBCO coated conductors: a one-century-old concept for the superconductivity of the future *Supercond. Sci. Technol.* vol 27 no 093001.

[17] Van der Laan DC *et al.* 2013 Characterization of a high-temperature superconducting conductor on round core cables in magnetic fields up to 20 T *Supercond. Sci. Technol.* vol 26 no 045005.

[18] Takayasu M, Chiesa L, Bromberg L and Minervini J 2016 Present status and recent developments of the Twisted Stacked-Tape Cable (TSTC) conductor *IEEE Trans. Appl. Supercond.* vol 26 no 2.

[19] Bykovsky N *et al.* 2015 Design optimization of round strands made by twisted stacks of HTS tapes *IEEE Trans. Appl. Supercond.* vol 26 no 4201207.

[20] Celentano G *et al.* 2014 Design of an industrially feasible twisted-stacked HTS

cable-in-conduit conductor for fusion application *IEEE Trans. Appl. Supercond.* vol 24 no 4601805.
[21] Cheggour N *et al.* 2003 Reversible axial-strain effect and extended strain limits in Y-Ba-Cu-O coatings on deformation-textured substrates *Appl. Phys. Lett.* vol 83 no 20 pp 4223–5.
[22] Van der Laan DC *et al.* 2010 Effect of strain, magnetic field and field angle on the critical current density of YBa2Cu3O7δ coated conductors *Supercond. Sci. Technol.* vol 23 no 072001.
[23] Zhang Y *et al.* 2016 Stress-strain relationship, critical strain (stress) and irreversible strain (stress) of IBAD-MOCVD-based 2G HTS wires under uniaxial tension *IEEE Trans. Appl. Supercond.* vol 26 no 4.
[24] Barth C *et al.* 2015 Electro-mechanical properties of REBCO coated conductors from various industrial manufacturers at 77 K, self-field and 4.2 K, 19T *Supercond. Sci. Technol.* vol 28 no 045011.
[25] Dedicatoria M, Shin H, Ha H, Oh S and Moon S 2010 Electro-mechanical property evaluation of REBCO coated conductor tape with stainless steel substrate *Supercond. Cryo.* vol 12 no 4.
[26] Majkic G *et al.* 2009 Electromechanical behavior of IBAD/MOCVD YBCO coated conductors subjected to torsion and tension loading *IEEE Trans. Appl. Supercond.* vol 19 no 3.
[27] Ilin K *et al.* 2015 Experiments and FE modeling of stress-strain state in REBCO tape under tensile, torsional and transverse load *Supercond. Sci. Technol.* vol 28 no 055006.
[28] Shin HS *et al.* 2007 Critical current degradation behavior in YBCO coated conductors under torsional strain *IEEE Trans. Appl. Supercond.* vol 17 no 2.
[29] Weiss K *et al.* 2011 Finite element analysis of torsion experiments on HTSC tapes *IEEE Trans. Appl. Supercond.* vol 21 no 3.
[30] Takao T *et al.* 2007 Influence of bending and torsion strains on critical currents in YBCO coated conductors *IEEE Trans. Appl. Supercond.* vol 17 no 2.
[31] Jin JX, Dou S X, Liu H K and Hardono T 1999 Critical current degradation caused by winding process of Bi-2223/Ag HTS wire in the form of a coil *IEEE Trans. Appl. Supercond.* vol 9 no 2.
[32] Shin HS *et al.* 2003 Ic degradation behavior in Bi-2223 superconducting tape under torsional deformation *Physica C* vol 392-396 no 2 pp 1162-66.
[33] Uglietti D *et al.* 2013 Effect of transverse load on the critical current of a coated conductor Roebel cable *Supercond. Sci. Technol.* vol 26 no 074002.
[34] Ekin J *et al.* 2001 Transverse stress and fatigue effects in Y-Ba-Cu-O coated IBAD tapes *IEEE Trans. Appl. Supercond.* vol 11 pp 3389-92.
[35] Nijhuis A *et al.* 2014 AC loss and mechanical tests on REBCO tapes, joints and cables at University of Twente *HTS4Fusion Workshop* CRPP Villigen.
[36] Uglietti D *et al.* 2006 Critical currents versus applied strain for industrial Y-123 coated conductors at various temperatures and magnetic fields up to 19 T *Supercond. Sci. Technol.* vol 19 pp 869-72.
[37] Sunwong P *et al.* 2013 The critical current density of grain boundary channels in polycrystalline HTS and LTS superconductors in magnetic fields *Supercond. Sci. Technol.* vol 26 no 095006.
[38] Takayasu M *et al.* 2013 Conductor characterization of YBCO twisted stacked-tape cables *IEEE Trans. Appl. Supercond.* vol 23 no 3.
[39] Barth C *et al.* 2015 Temperature-and field dependent characterization of a twisted stacked-tape cable *Supercond. Sci. Technol.* vol 28 no 045015.
[40] Van der Laan DC *et al.* 2015 Development of HTS conductor on round core

(CORC) cables for fusion application *HTS4Fusion Workshop* Italy.
[41] Fleiter J *et al.* 2013 Electrical characterization of REBCO Roebel cables *Supercond. Sci. Technol*. vol 26 no 065014.
[42] Barth C *et al.* 2012 Electro-mechanical analysis of Roebel cables with different geometries *Supercond. Sci. Technol.* vol 25 no 025007.
[43] Nijhuis A *et al.* 2015 Transverse, axial and torsional strain in REBCO tapes: experiments and modeling *Chats-Applied Superconductivity Workshop*, Italy.
[44] Allen NC, Chiesa L and Takayasu M 2016 Structural modeling of HTS tapes and cables *Cryogenics* doi:10.1016.
[45] Chiesa L, Takayasu M, Allen NC and Bromberg L 2013 Electromechanical investigation of different type YBCO tapes for Twisted Stacked-Tape Cabling *IEEE Trans. Appl. Supercond.* vol 23 no 3.
[46] Allen NC *et al.* 2015 Numerical and experimental investigation of the electromechanical behavior of REBCO tapes," *IOP Conference Series: Materials Science and Engineering (MSE)* vol 102 no 012025.
[47] Allen NC, Chiesa L and Takayasu M 2015 Combined tension-torsion effects on 2G REBCO tapes for Twisted Stacked-Tape Cabling," *IEEE Trans. Appl. Supercond.* vol 25 no 3.
[48] Chiesa L, Allen NC and Takayasu M 2014 Electromechanical investigation of 2G HTS Twisted Stacked-Tape Cable conductors," *IEEE Trans. Appl. Supercond.* vol 24 no 3.
[49] De Marzi G, Allen NC, *et al.* 2106 Bending tests of HTS cable-in-conduit conductors for high-field magnets applications," *IEEE Trans. Appl. Supercond.* vol 26 no 4.
[50] Allen NC *et al.* 2016 Structural finite element evaluation of twisted stacked-tape cables for high-field magnets *IEEE Trans. Appl. Supercond.* (submitted for publication – ASC2016).
[51] Nyilas A 2005 Strain sensing systems tailored for tensile measurement of fragile wires *Supercond. Sci. Technol.* vol 18 pp S409-15.
[52] Shin HS *et al.* 2013 Intrinsic strain effect on critical current in Cu-stabilized GdBCO coated conductor tapes with different substrates *Supercond. Sci. Technol.* vol 26 no 055005.
[53] Matweb – Material Property Data Website: Stainless Steel Type 304, 20% CR http://matweb.com/search/DataSheet.aspx?MatGUID=1462ed9ca5334a75b52e748b3f3195e5
[54] Cheggour N *et al.* 2003 Transverse compressive stress effect in Y-Ba-Cu-O coatings on biaxially textured Ni and Ni-W substrates *IEEE Trans. Appl. Supercond.* vol 13 no 2 pp 3530–3.
[55] Clickner CC, Ekin J, Cheggour N, *et al.* 2006 Mechanical properties of pure Ni and Ni-alloy substrate materials for Y–Ba–Cu–O coated superconductors *Cryogenics* vol 46 no 6 pp 432–8.
[56] Brechna H *et al.* 1971 Cryogenic properties of metallic and non-metallic materials utilized in low temperature and superconducting magnets *8th Int. Conf. High-Energy Accelerators* Inst. fur Experim. Kernphysik C71-09-20.
[57] Reed *et al.* 1967 Low temperature mechanical properties of copper and selected copper alloys *National Bureau of Standards* Boulder, CO.
[58] Huang H and Spaepen F 2000 Tensile testing of free-standing Cu, Ag and Al thin films and Ag/Cu multilayers *Acta mater.* vol 48 pp 3261-9.
[59] Verdier M *et al.* 2006 Microstructure, indentation and work hardening of Cu/Ag multilayers *Phil. Mag.* vol 86 pp 5009–16.
[60] Goretta K *et al.* 1995 Mechanical properties of high-temperature superconducting

wires *Proc. of 4th World Congress on Supercond.* NASA Conference Publication vol 3290 pp 633–8.
[61] Raynes AS *et al.* 1991 Fracture toughness of YBa2Cu3O6+δ single crystals: Anisotropy and twinning effects *J. Appl. Phys.* vol 70 no 5254.
[62] Ledbetter H and Ming L 1991 Monocrystal elastic constants of orthotropic YBCO: An estimate *J. Mater. Res.* vol 6 pp 2253–5.
[63] Van der Laan DC and Ekin JW 2008 Dependence of the critical current of YBa2Cu3O7 coated conductors on in-plane bending *Supercond. Sci. Technol. vol* 21 no 115002.
[64] Takayasu M, Chiesa L, Bromberg L and Minervini J 2012 HTS twisted stacked-tape cable conductor *Supercond. Sci. Technol.* vol 25 no 014011.
[65] Osamura K *et al.* 2009 Internal residual strain and critical current maximum of a surrounded Cu stabilized YBCO coated conductor *Supercond. Sci. Technol.* vol 22 no 065001.
[66] Takayasu M *et al.* 2011 Investigation of twisted stacked-tape cable conductor *Adv. Cryo. Eng.* vol 58 pp 273-80.
[67] Barth C *et al. 2012* Measurements of HTS cables in a temperature range of 4.2 K to 80 K and background fields up to 12 T *Applied Superconductivity Conference* Portland, OR.
[68] Weiss KP, Bagerts N, Sas J and Kvackaj T 2016 Mechanical and thermal properties of central former material for high current superconducting cables *IEEE Trans. Appl. Supercond.* vol 26 no 4.
[69] Matweb – Material Property Data Website: Aluminum 6063-T6 http://matweb.com/search/DataSheet.aspx?MatGUID=333b3a557aeb49b2b17266558e5d0dc0
[70] Mruzek MT 1980 Properties and methods of lead/tin splices for superconductors TM-944 *Fermilab* Batavia, USA.
[71] Fast RW *et al.* 1988 Electrical and mechanical properties of lead/tin solders and splices for superconducting cables *Cryogenics* vol 28.
[72] Matweb – Material Property Data Website: 60-40 Soft Solder (60Sn-40Pb) http://matweb.com/search/DataSheet.aspx?MatGUID=06a31d97bb734b509043d81cf131b280
[73] Takayasu M *et al.* 2015 Analytical investigation in bending characteristic of twisted-stacked-tape cable conductor *IOP Conference Series: Materials Science and Engineering (MSE)* vol102 no 012023.
[74] Liu T 1964 Sliding friction of copper *Wear* vol 7 no 2.
[75] Hong SY *et al.* 2002 Experimental evaluation of friction coefficient and liquid nitrogen lubrication effect in cryogenic machining *Mach. Sci. and Tech.* vol 6 no 2 pp 235-50.